POLITECNICO DI TORINO

Master's Degree in Energy and Nuclear Engineering

Master's Degree Thesis

Models and simulations of electron-positron pair cascades in time-dependent, non-uniform electric fields

Supervisors

Prof. Gianni COPPA[a]

Prof. Luís Miguel DE OLIVEIRA E SILVA[b]

Dott. Fábio CRUZ[b]

Dott. Thomas GRISMAYER[b]

[a)] Politecnico di Torino

[b)] Instituto Superior Técnico, Lisbon

Candidate

Paolo TORTONE

October 2023

Abstract

The nature of pulsar radio emission is a longstanding open problem in high-energy astrophysics, mainly due to the intrinsic challenge of modeling the behavior of the electron-positron plasma filling its magnetosphere. That region gathers the most extreme physical conditions, as pulsars are the most compact and magnetized stellar objects we know of. Time-dependent cascades of electron-positron pairs are thought to be the main source of the aforementioned plasma, together with being the main ingredient to explain the nature of the characteristic pulsars radio emission. The cascade events consist in positive feedback loops of gamma-ray photon emission, produced via curvature radiation by TeV electrons and positrons, and pair production.

In this Thesis, I present the analytical models aimed at describing the pair cascades in the framework of pulsar kinetic electrodynamics: starting from the description of the underlying QED mechanisms of photon emission and pair production, the self-consistent development of pair cascades in the pulsar polar caps is investigated accounting for the time dependency of the electric field and its spatial non-homogeneity. The onset stage and the exponential growth of those events are studied in the case of a background linear electric field by using an heuristic model of the pair production process, while the saturation stage is instead analyzed purely through parametric analysis.

The analytical results are confirmed with the use of the fully-relativistic particle-in-cell (PIC) code OSIRIS, which relies on pushing macro-particles on a grid by forces deriving from solving the full set of Maxwell's equations, which in turn depend on the self-consisting charge densities, currents and fields. PIC method is shown to be fundamental to reduce the high computational effort associated to the kinetic characterization of the plasma dynamics and the presence of many QED processes, which are intrinsically highly nonlinear. Following the heuristic approach, different simulation setups are investigated in order to reconstruct and confirm the analytical models, together with performing parallel parametric analysis aimed at inferring possible considerations in the study of these high-energy plasmas.

La natura delle emissioni radio delle pulsar è, ad oggi, una questione aperta nell'astrofisica delle alte energie, principalmente a causa della difficoltà intrinseca nel modellare il comportamento del plasma di elettroni e positroni che popolano la magnetosfera di questi corpi celesti. La regione in esame è caratterizzata da condizioni fisiche estreme, essendo le pulsar i corpi celesti più compatti e più magnetizzati che conosciamo. Si pensa che la principale sorgente di questo plasma sia da ricercare in processi a cascata che portano alla creazione di coppie elettroni-positroni, oltre ad essere l'ingrediente principale per descrivere la natura delle caratteristiche emissioni radio delle pulsar. Questi processi consistono in cicli a feedback positivo di emissioni di raggi gamma, prodotti da radiazione di sincrotrone di elettroni e positroni da svariati TeV, e produzione di coppie.

In questa Tesi presento i modelli analitici atti a descrivere le cascate nel contesto dell'elettrodinamica delle pulsar. Partendo da una descrizione dei meccanismi QED alla base, emissione di fotoni e produzione di coppie, si indaga lo sviluppo autoconsistente di cascate di coppie tenendo in considerazione la dipendenza temporale del campo elettrico e la sua disomogeneità spaziale. Lo stadio iniziale e la crescita esponenziale di questi eventi sono studiati nel caso di un campo elettrico lineare di fondo utilizzando un modello euristico del processo di produzione di coppie, mentre lo stadio di saturazione è analizzato puramente tramite analisi parametriche.

I risultati analitici sono confermati utilizzando il codice PIC (particle-in-celle) OSIRIS, tramite il quale macro-particelle di plasma sono spinte su una griglia da forze derivanti dalla soluzione delle equazioni di Maxwell che, a loro volta, dipendono da campi elettrici, cariche e correnti autoconsistenti. Il metodo PIC si rivela fondamentale per ridurre l'elevato sforzo computazionale associato alla caratterizzazione cinetica della dinamica dei plasmi e alla presenza di diversi processi QED, in quanto intrinsecamente non-lineari. Seguendo l'approccio euristico, diverse configurazioni sono indagate con lo scopo di ricostruire e confermare i modelli analitici, insieme allo sviluppo di diverse analisi paramentriche atte a trarre possibili considerazioni nello studio di questi plasmi ad alta energia.

Acknowledgements

This thesis is the culmination of a journey that would not have been possible without the support of many to whom I would like to express my gratitude.

First, I would like to thank my supervisor Gianni Coppa for the extraordinary opportunity and unwavering support in sending me to Instituto Superior Técnico to conduct and write my thesis. Your belief in my abilities and dedication to my success have inspired me to strive for excellence in every aspect of this work.

I would like to acknowledge my supervisors at IST Fábio Cruz, Thomas Grismayer and Luís Silva, your guidance and mentorship have been instrumental throughout this international experience, and I am profoundly thankful for the trust and confidence you placed in me. I extend my heartfelt gratitude to Pablo, Chiara, Bernardo, Simon, Daniel and all the EPP GoLP team, with whom I shared this journey, which has been a pivotal chapter in my academic and personal development.

A special thanks goes to the dedicated team of nurses and medical staff, who stood by me during my chemotherapy treatments, and to Uga and Paolo, you are my "angels". Your kindness, patience, and reassuring presence were a source of comfort during some of the most trying moments of my life. This thesis is not only a testament to my academic journey but also a tribute to the remarkable individuals like them, who played an essential role in my recovery and well-being.

To Alex, Lorenzo and Davide I am thankful for the invaluable bonds formed during the university years, I look forward to seeing how we continue to inspire each other in our future endeavors. I am particularly thankful to all the members of the Planar, their sincere friendship, camaraderie, and shared experiences have enriched me in countless ways. I extend my genuine thanks to Matteo, Simone, Chiara, Michelle, Silvia and Elisa, your fellowship has reminded me of the importance of maintaining a balance between academic pursuits and personal connections.

Finally, I would like to thank my family, for their unconditional support, boundless love and being always there. To my parents Laura and Romano, your sacrifices, guidance, and constant encouragement have been the driving force behind my pursuit of knowledge. To my sisters Alessia and Michela, I look forward to the day when I can be the role model and mentor you deserve, just as you have been a source of motivation for me. To my extended relatives who have offered their blessings throughout this journey, your encouragement meant the world to me.

Table of Contents

Chapter 1

Introduction

1.1 Pulsars

Pulsars are astronomical objects that gather the most extreme physical conditions as they are the most compact and the most magnetized stellar objects we know of, with typical masses of tens solar masses and radii of tens of km. A strongly magnetized rotating neutron star is thought to be at their core, which is responsible for the radiations emitted by these objects that span from radio to gamma-rays. They are the end result of supernovae explosions after supergiant stars collapse, and remain stable due to the equilibrium between self-gravitation and neutron degeneracy pressure [1]. Along with that, their intrinsic magnetic fields can be as large as 10^{12} G, supporting highly relativistic plasmas and their complex self-consistent electromagnetic fields, that extend to light-years away from the neutron star surface.

Early observational evidences of pulsar came from A. Hewish, J.B. Bell *et al.* [2] as as source of pulsed radio emission at a frequency of 81.5 MHz with an incredibly constant period of 1.33 s. The most likely astronomical body which could emit that kind of pulsed radio wave are compact stars, either a white dwarf or a neutron star. A common analogy for the pulsed character of this emission is the one with the light emitted by lighthouses, that can be directly observed only periodically, which is based on the association between the rotation of the neutron star and the constancy of emission period [3]. Later on, various observations highlighted other significant radiation signatures of pulsars, in the high-energy X-ray and gamma-ray bands; the most significant discovery of high-energy radiating pulsars came recently from the Fermi space telescope [4].

Thomas Gold [5] proposed a model where the neutron star magnetosphere - the region close to the star characterized by the highest magnetization - would be filled with plasma in corotation with the stellar surface up to a radius $R_{\rm LC}$, or

light-cylinder radius, that can be expressed as

$$R_{\rm LC} = \frac{c}{\Omega} \ , \tag{1.1}$$

and defines a cylinder beyond which the linear velocity required for corotation would exceed the speed of light c in a neutron star with rotation frequency Ω.

Despite decades of observations and theoretical research, there is yet no consensus in the plasma astrophysics community regarding radio emissions from pulsars [6], hence no definite, robust model had yet fully connected radio emission to collective plasma processes. The driving scope of this work was to investigate the possibility that plasma collective effects may actually play a significant role in those emissions.

1.1.1 System characterization

The general configuration of pulsar magnetospheres has been well established for decades following the model proposed in the work by P. Goldreich and W. H. Julian [7]. In this model, the star is considered to be an ideal magnetized rotating spherical conductor with radius $r_* = 10$ km, rotating with frequency $\Omega \sim 1$ - 10 Hz, highly magnetized with surface magnetic field $B \sim 10^{12}$ G . Such a conductor rotating in vacuum induces an electric field above the stellar surface strong enough to extract charged particles from it. For this very reason, a plasma-filled magnetosphere must exist surrounding the neutron star, which screens the strong rotation-induced electric field parallel to the magnetic field. More precisely, we consider the part of its magnetosphere that can corotate with the star i.e. the magnetosphere located between the surface of the star and $R_{\rm LC} = c/\Omega$. The charge density required to effectively screen the parallel electric field is called the Goldreich-Julian (hereafter GJ) density, and is given by

$$\rho_{\rm GJ} = \frac{\nabla \cdot \mathbf{E}}{4\pi} = -\frac{\mathbf{\Omega} \cdot \mathbf{B}}{2\pi c} \frac{1}{1 - (\Omega r/c)^2 \sin^2 \chi} \ , \tag{1.2}$$

where $\mathbf{E}$ and $\mathbf{B}$ are the vacuum electric and magnetic fields, $\mathbf{r} = r\hat{\mathbf{r}}$ is the coordinate vector and χ is the angle between the magnetic axis and the rotation axis, defined by the vector $\mathbf{\Omega}$ as shown in Figure 1.1. This charge-separated GJ plasma on the surface of the star is filled with relativistic leptons. Because of the strong magnetic field, it is assumed that particle motion is restricted to occur mostly along the magnetic field lines and that they rotate with the stellar surface, ensuring that the electric field component parallel to B is fully screened. Thus, in almost all the magnetosphere $\mathbf{E} \cdot \mathbf{B} \sim 0$. However, since the plasma can only corotate with the star up to a cylindrical radius $R_{\rm RL}$, the magnetosphere itself is divided in two regions: the region of magnetic field lines that close on the neutron star and from

which the plasma cannot escape, and the region of open field lines, from which plasma can outflow as shown in Figure 1.1.

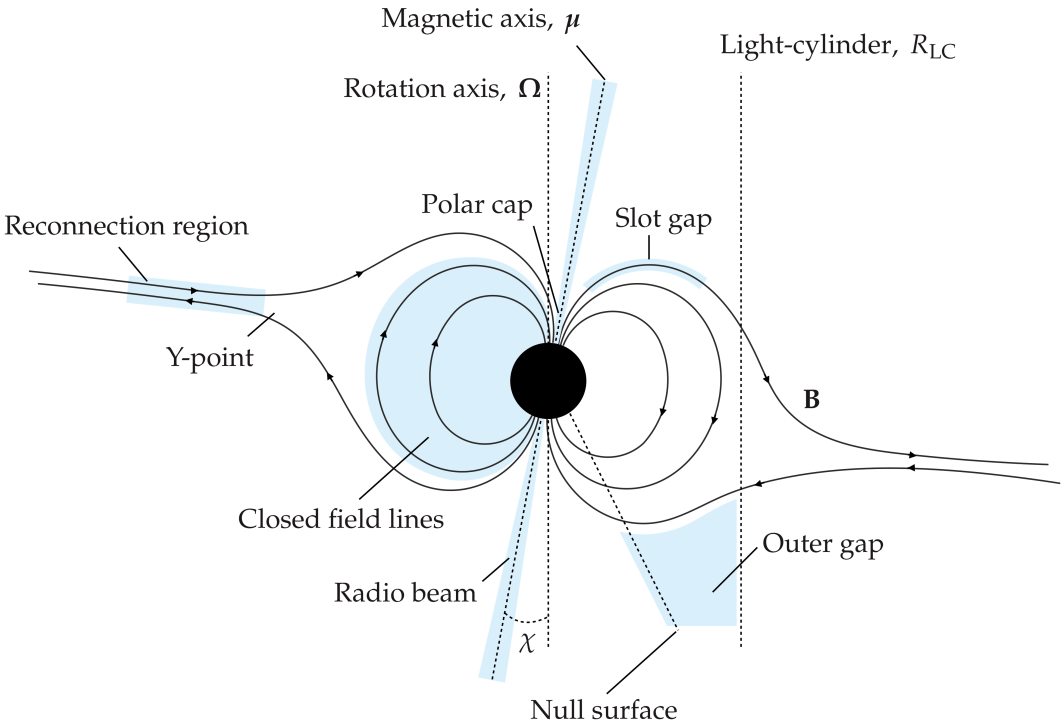

Figure 1.1: Schematic representation of a pulsar magnetosphere. The central neutron star is drawn with a black circle and the relevant regions are highlighted and/or identified with labels. Figure taken from [8]

The magnetic field of neutron stars is assumed to be well approximated by a dipolar profile. With this configuration, the open field lines form a bundle that starts in the magnetic polar regions and extend to infinity. At the transition between open and closed field lines, the magnetic field assumes a Y shape, which helps converting efficiently magnetic energy into particle kinetic energy thanks to the favourable onset of a process called "magnetic reconnection" [7].

1.1.2 Physical processes involved

The plasma outflow through open field lines required by this model poses an important problem: a source is required to replenish the leaking magnetosphere. In order to provide a charge density $\rho_{\rm GJ}$ and an associated current density $|\mathbf{j}_m| \simeq \rho_{\rm GJ} c$ to the outer magnetosphere that supports the equilibrium solution of Goldreich and Julian [7], Peter Sturrok [9] proposed as sites of intense pair plasma production

the vacuum gaps, regions of strong unscreened electric field where the equilibrium charge and current density conditions are not met locally. Therefore, in those vacuum gaps an electric field $\mathbf{E}$ can actually accelerate particles along the magnetic field lines such that $\mathbf{E} \cdot \mathbf{B} \neq 0$.

The vacuum gap dynamics can be described in a frame co-rotating with the neutron star [10], where Gauss's and Ampere's laws become:

$$\nabla \cdot \mathbf{E} = 4\pi \left(\rho - \rho_{\mathrm{GJ}}\right) \tag{1.3}$$

$$\frac{\partial \mathbf{E}}{\partial t} = -4\pi \left(\mathbf{j} - \mathbf{j}_m\right) \tag{1.4}$$

where $\mathbf{j}_{\mathrm{m}}$ is a free parameter that can be interpreted as the current density which flows in the star crust towards the vacuum gap.

Two main classes of quantum electrodynamic (QED) models for vacuum gaps, needed to replenish the magnetosphere, occur in neutron star polar caps, the regions of the stellar surface that embed the footprints of open field lines. For a dipolar magnetic field profile, these footprints are located around the magnetic axes of the star [11].

The first model assumes that a significantly dense population of charged particles are extracted from the stellar surface and accelerated to high energies. These relativistic leptons, co-rotating with the pulsar magnetosphere, stream along curved magnetic field lines and emit gamma-ray photons through curvature radiation that, very like the synchrotron radiation, appears when an accelerated charge follows a locally curved trajectory.

It is worth noticing that, due to the intensity of the magnetic field $\mathbf{B}$, the gyro-frequency $\omega = eB/m\gamma c$ of an electron of charge $-e$, mass m and Lorentz factor γ, is so large that the momentum (of a lepton) perpendicular to the local magnetic field is almost instantaneously dissipated to very low values due to the radiation reaction force associated to synchrotron emission. Electrons and positrons can be then assumed to follow the local magnetic field lines, radiating mostly because of their motion along the curved field line rather than perpendicular to it. Furthermore, this emission does not significantly perturb the trajectory of the lepton, only its energy.

The so-produced photons then propagate away from the star and undergo multi-photon Breit-Wheeler (also known as nonlinear B-W or strong field B-W) pair production, another relevant QED process in pulsar polar caps: photons are absorbed in the strong magnetic field and converted into electron-positron pairs.

For the second model let's assume, without loss of generality, that the electric field in the gap is negative: the positrons are then accelerated towards the neutron star surface, while the electrons are accelerate outwards. If a positron is provided

from regions of higher altitude, where $\mathbf{E} \cdot \mathbf{B} = 0$, it enters the vacuum gap and it is accelerated almost instantaneously to relativistic speed along the strong curved magnetic field. This positron can emit gamma-ray photons through curvature radiation, therefore gradually reducing its energy; the so-produced photons then propagate away from the star and, following the same mechanisms as in the first model, can later decay in the strong magnetic field, converting into electron-positron pairs. Those leptons, that are produced with some delay, are in turn accelerated and will eventually undergo the same processes: the process of pair production, followed by re-acceleration of the leptons and consequently by repeated pair production events takes the name of "pair cascade". A schematic representation of this process in a polar cap vacuum gap is shown in Figure 1.2.

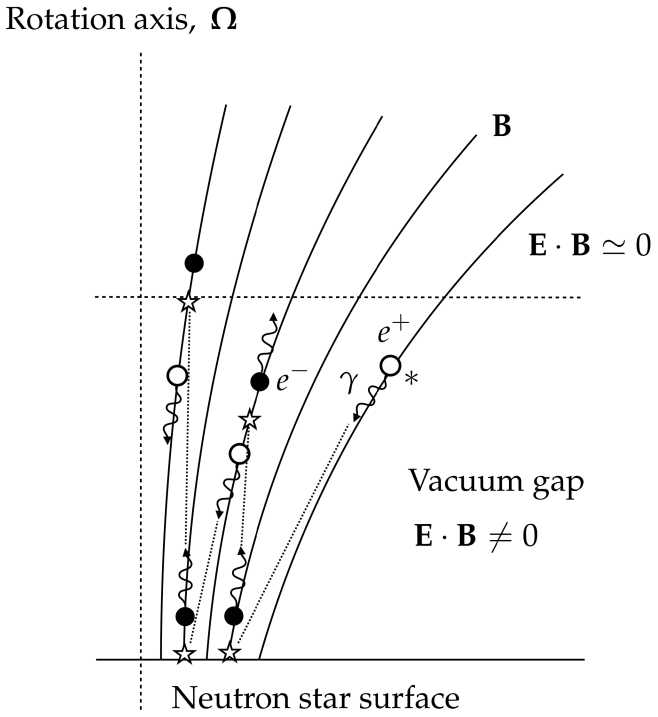

Figure 1.2: Schematic representation of a pair cascade in a polar cap vacuum gap. An initial positron e^+ (marked with *) enters the gap, producing a curvature photon γ. After propagating a finite distance (trajectory indicated with a dashed line), the photon decays into an electron-positron pair e^-e^+ (event marked with a star icon). The positron is absorbed at the neutron star surface, and the electron is accelerated outwards, emitting a new photon. This process is repeated until the fresh plasma drives enough current to screen the vacuum electric field. For simplicity, the rotation axis is assumed to be aligned with the magnetic axis. Figure taken from [8]

Once created, this electron-positron plasma can advect to outer regions in the magnetosphere and provide the charge density $\rho_{\rm GJ}$ and the associated current which can satisfy the equilibrium of the magnetosphere itself. The overall effectiveness of pair cascades in replenishing the magnetospheric plasma can be quantified via the plasma multiplicity at the end of the discharge process, which is defined as

$$\mathcal{M} = \frac{\rho_+ + |\rho_-|}{|\rho_{GJ}|} = \frac{n_+ + n_-}{n_{GJ}} \tag{1.5}$$

where $\rho_\pm = \pm e n_\pm$ are the charge densities of positrons and electrons, while $n_{GJ} = |\rho_{GJ}|/e$ is the Goldreich-Julian particle number density. For standard pulsar parameters, the $\mathcal{M}$ parameter can be as large as 10^5 [12], which justifies the GJ equilibrium conditions to be achieved through polar cap discharges.

The pair cascade self-regulates, stopping when the fresh plasma conducts the required current and has the required charge density to screen the vacuum electric field. Once the electric field is totally screened, the plasma is driven away from the magnetosphere following the open field lines. As the plasma advects into the outer magnetosphere, the density of the plasma does not match the equilibrium density anymore, therefore the vacuum gap opens again and the process is repeated.

1.2 This dissertation

1.2.1 Objectives and outline

The overarching goal of this Thesis is to present the analytic models and the associated large-scale *ab initio* particle-in-cell (PIC) simulations aimed at describing the pair cascades in the framework of pulsar kinetic electrodynamics.

Starting from the description of the underlying QED mechanisms of photon emission and pair production, the self-consistent development of pair cascades in pulsar polar caps is investigated with the analytical models presented in Chapter 2. The recent 1-D model described by F. Cruz [13], which is based on a constant electric field in an infinite gap, did not account for the time-dependency of the electric field, nor for its spacial non-homogeneity, despite it still lead to relevant results regarding the macroscopic plasma dynamics of pulsars. This work aims at making this model more realistic by following the ideas of Timokhin [10] by investigating time-dependent electric fields and studying the self-consistency of the phenomena. This new assumption required the implementation of further parameters in the first-principle description of the QED processes treated, which in turn evolved in parametric analysis aimed at validating the accuracy of the whole model itself for what concerns the time and energy scales of the problem.

High-performance computing technologies, together with the advancements in numerical techniques, have enabled a remarkable progress in the understanding of pulsar electrodynamics in the last two decades. Fluid models developed for the description of pulsar magnetosphere are based on magnetohydrodynamics (MHD), which considers the plasma as a single fluid; however, this MHD approach cannot include the intrinsically kinetic character of phenomena such as particle acceleration.
The research presented in this Thesis strongly relies on massively-parallel particle-in-cell (PIC) simulations performed with the OSIRIS code. In Chapter 3, the analytical expression are compared with the numerical result of the simulations performed with OSIRIS, which has been suitable for the description done hereafter thanks to the various QED processes it has implemented. These PIC simulations, performed using realistic pulsar parameters, have been used to obtain fully kinetic models of pulsar magnetospheres. Vacuum gaps are demonstrated to open periodically, producing burst of pair plasma, and the different species (electrons and positrons) have been studied individually and in conjunction in order to fully describe their role in the cascade process, both in the local-short and global-long scales.

Finally, in Chapter 4 the conclusion of this Thesis are presented and open challenges in the multiscale modelling of pulsars magnetospheres are discussed.

1.2.2 Particle-in-cell (PIC) methodology

The phenomena investigated in this Thesis require a kinetic characterization of the plasma dynamics and present many QED processes, which are intrinsically highly nonlinear. While attempting to simulate plasma behavior we may first be tempted directly simulate the interaction of all the particles, using what is known as Particle-Particle method. At each time step would be necessary to calculate the forces acting on the particles and then to push the particles themselves, leading to a total number of operations $10N_p^2 - N_p$, therefore scaling with N_p^2 [14]. Another method is the so-called Particle-Mesh method, in which the forces are exchanged through fields that are approximated by a regular array of mesh points, where field values at the particles position are obtained by interpolation. Despite being already faster that the previous one, this method is still not feasible for the number of particles we need to simulate. Since we are generally interested in the collective behavior of the plasma and not in the time evolution of each individual particle, the optimal choice will be using "superparticles" (ensembles of real particles) which makes also good physical sense. These superparticles could be seen as finite-sized clouds of plasma particles, with position and velocity being those of their center of mass.

The first-principle kinetic simulations are performed with the Particle-In-Cell method, or PIC, which is a subset of the Particle-Mesh method. PIC codes rely

on solving the full set of Maxwell's equations on a grid using currents and charge densities calculated by weighting discrete particles onto the grid. Each particle is pushed to a new position and momentum via self-consistently calculated fields therefore, to the extent that quantum mechanical effects can be neglected, these codes make no physics approximations.
The key equation that describes the motion of the particles is the Lorentz equation

$$\dot{\mathbf{p}}_p = q_p \left(\mathbf{E} + \frac{\mathbf{v}_p}{c} \times \mathbf{B} \right) \tag{1.6}$$

where $\mathbf{p}_p$ is the particle momentum, q_p is the particle charge, $\mathbf{v}_p$ is the particle velocity, and $\mathbf{E}$ and $\mathbf{B}$ are, respectively, the electric and the magnetic field.

The simulation domain is represented by a discrete spatial grid, in which the superparticles continuously move. As they move across the grid, charged superparticles carry electrical currents that are deposited on the grid vertices. These currents, defined with the vector $\mathbf{j}$, are then used to advance the electric and magnetic fields $\mathbf{E}$ and $\mathbf{B}$ in time via Faraday's and Ampère's laws, respectively

$$\frac{\partial \mathbf{B}}{\partial t} = -c\nabla \times \mathbf{E} \tag{1.7}$$

$$\frac{\partial \mathbf{E}}{\partial t} = c\nabla \times \mathbf{B} - 4\pi\mathbf{j} \tag{1.8}$$

By using the generalized velocity $\mathbf{u}_p \equiv \gamma_p \mathbf{v}_p$, where $\gamma_p = (1 - \|\mathbf{v}_p\|^2/c^2)^{-1/2}$ is the Lorentz factor, we could obtain the relativistic generalization of equation 1.6

$$\dot{\mathbf{u}}_p = \frac{q_p}{m_p} \left(\mathbf{E} + \frac{1}{c}\frac{\mathbf{u}_p}{\gamma_p} \times \mathbf{B} \right) \tag{1.9}$$

where m_p is the particle mass. The corresponding Lorentz force is combined with other external forces (e.g. external electromagnetic or gravitational fields, radiation recoil) and used to advance the particles' momentum via the relativistic equations of motion

$$m_p \frac{d(\gamma_p \mathbf{v}_p)}{dt} = \mathbf{F}_p^L + \mathbf{F}_p^{ext} = q_p(\mathbf{E} + \frac{v_p}{c} \times \mathbf{B}) + \mathbf{F}_p^{ext} \tag{1.10}$$

where $\mathbf{F}_p^{ext}$ is the external force applied to it. Particle's position $\mathbf{x}_p$ is finally updated by solving

$$\frac{d\mathbf{x}_p}{dt} = \mathbf{v}_p \tag{1.11}$$

The most common numerical scheme to solve equation 1.7 and 1.8 in PIC is the Yee solver [15], a second-order finite-difference time-domain method that considers $\mathbf{E}$ and $\mathbf{B}$ to be defined in staggered positions on the grid. Equations 1.10 and 1.11

are solved with the so-called Boris pusher [16] using the updated electromagnetic field values, defined on the grid vertices, interpolated to the particles' positions. This numerical scheme is a leapfrog method that defines $\mathbf{x}_p$ and $\mathbf{u}_p$ at interleaved times. Current deposition algorithms compute the current density $\mathbf{j}$ on the grid vertices while ensuring the continuity equation

$$\frac{\partial \rho}{\partial t} + \nabla \cdot \mathbf{j} = 0 \tag{1.12}$$

Ensuring equation 1.12 guarantees that the electric field satisfies Gauss' law,

$$\nabla \cdot \mathbf{E} = 4\pi\rho \tag{1.13}$$

an equation not solved explicitly in PIC.

Figure 1.3 shows the PIC loop cycle. Beginning with a self-consistent initial condition for particle position/velocity and electric/magnetic fields, the cycle first interpolates the field values a the particle position. Then, using the interpolated fields, it integrates the equations of motion of the particles. It then proceeds to deposit the current density values on the grid and finally uses these values to integrate the field equations. The topmost block represents the additional modifications performed by the code OSIRIS, which also accounts for the QED processes occurring.

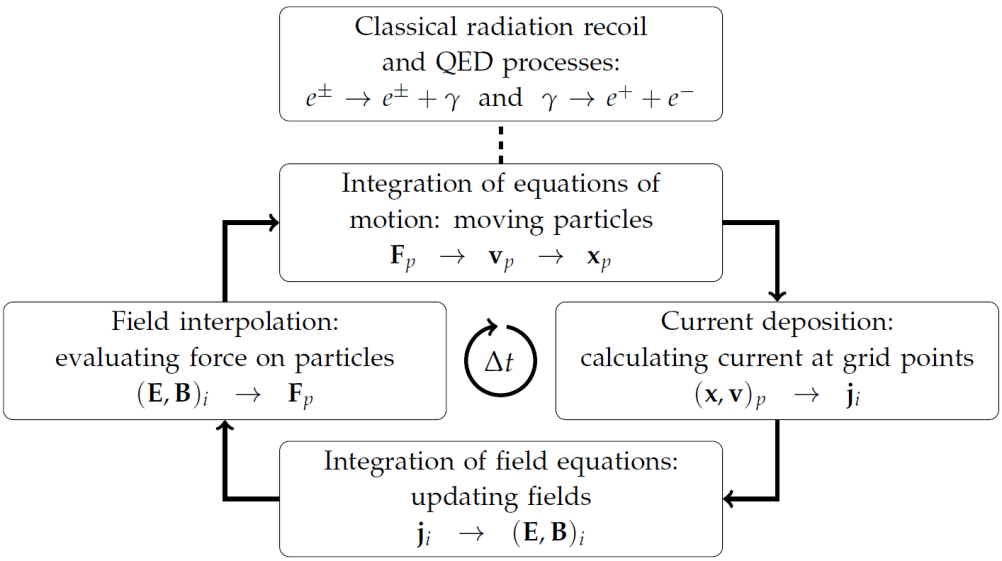

Figure 1.3: Simulation loop cycle performed by OSIRIS. Grid quantities are shown with indices i and particles are labeled with subscript p. Figure taken from F. Cruz [8]

All sub-steps of PIC can be performed with only local operations (in space). For this reason, PIC can be solved independently by a collection of computing nodes that only require information exchange with their neighbours. Furthermore, because the individual macro-particles interact through the collectively produced electromagnetic fields defined on a grid, the number of computations in PIC scales proportionally to N_p (and not to N_p^2 as particle-particle codes), where N_p is the number of simulated macro-particles. These highly scalable properties set PIC as a unique and efficient tool to model plasma dynamics ranging from the kinetic to meso and large scales.

Another thing worth mentioning is that PIC simulations are usually done in normalized units, therefore the multiplication by several constants is avoided, hence increasing the overall performances. Furthermore, by expressing the quantities used in the simulation in terms of the fundamental plasma quantities ω_p, m_e, e and c, respectively the electron plasma frequency, its rest mass, its charge and the speed of light, the obtained results are general and not bound to some specific units we might have chosen. Position, linear momentum, electric and magnetic field become

$$\mathbf{x}' = \frac{\omega_p}{c}\mathbf{x} \tag{1.14}$$

$$\mathbf{p}' = \frac{\mathbf{p}}{m_{sp}c} = \frac{\gamma\mathbf{v}}{c} = \frac{\mathbf{u}}{c} \tag{1.15}$$

$$\mathbf{E}' = e\frac{c/\omega_p}{m_e c^2}\mathbf{E} \tag{1.16}$$

$$\mathbf{B}' = e\frac{c/\omega_p}{m_e c^2}\mathbf{B} \tag{1.17}$$

where m_{sp} is the mass of the considered species. In this case γ can be calculated as $\gamma = (1 + p'^2)^{1/2}$.

Chapter 2

Analytical models

As previously stated, the development of pair cascades and the following plasma collective dynamics are highly non-linear phenomena. In this chapter, the heuristic pair production analytical models used to investigate the onset, saturation and late stage of pair cascade are described. In a preliminary section, a constant external field is considered in order to characterize the pair cascade process, hence the self-consistent excitation and damping of current-driven plasma waves; subsequently, the model is generalized in order to consider the growth of a non-linear self-consistent electric field.

2.1 Quantum parameters

As leptons are accelerated along magnetic field lines up to TeV they emit γ rays curvature photons. This is the classical limit of nonlinear Compton scattering, which consists in the interaction between a lepton with energy $\epsilon_\pm = \gamma_\pm m_e c^2$ and an arbitrary number of photons (which describe the background electric field). In this QED process, a photon with a fraction f_γ of the lepton's energy is emitted, hence $\epsilon_\gamma \equiv f_\gamma \epsilon_\pm$ with an associated lepton recoil. The differential probability rates for these QED processes are well known [17] [18] functions of the energy, local electromagnetic field components and momentum components of the parents particles. These complex functions, hence the QED processes regulating pair discharges, revolve around the Lorentz invariant $\chi_{\pm,\gamma}$ of the electron, positrons and photons (subscript $\pm$ and γ, respectively) defined as

$$\chi_\pm = \frac{1}{B_Q}\sqrt{\left(\gamma_\pm \mathbf{E} + \frac{\mathbf{p}_\pm}{m_e c} \times \mathbf{B}\right)^2 - \left(\frac{\mathbf{p}_\pm}{m_e c} \cdot \mathbf{E}\right)^2} \tag{2.1}$$

$$\chi_\gamma = \frac{1}{B_Q}\sqrt{\left(\frac{\epsilon_\gamma}{m_e c^2}\mathbf{E} + \frac{\hbar \mathbf{k}_\gamma}{m_e c} \times \mathbf{B}\right)^2 - \left(\frac{\hbar \mathbf{k}_\gamma}{m_e c} \cdot \mathbf{E}\right)^2} \tag{2.2}$$

where $\mathbf{p}_\pm$ is the momentum of the lepton, ϵ_γ is the photon energy and $\mathbf{k}_\gamma$ is the wavevector. The quantum parameter $\chi_\pm$ (χ_γ) corresponds to the ratio between the electromagnetic field that the lepton (photon) experiences at rest and the Schwinger critical field $B_Q \simeq 4.4 \times 10^{13} G$, which in turn defines the field able to perform a work equal to an electron rest mass within a Compton wavelength. The emission can be considered classical, hence the QED effects can be disregarded, when the ratio between the energies of the radiated photon and the producing lepton is negligible, hence when

$$f_\gamma = \frac{\epsilon_\gamma}{\gamma_\pm m_e c^2} = \frac{\chi_\gamma}{\chi_\pm} \ll 1 \tag{2.3}$$

which subsists if we assume that the leptons are moving almost exactly along the MF lines and for typical pulsar surface field $B \simeq 10^{12} G$.

2.2 Constant electric field

On the analytical side, a recent 1-D model described by Cruz et al. [13] assumes the presence of a constant electric field in an infinite gap; this model represents the background over which we will build our study.

To begin with, photons are assumed to have zero mean free path, which means that the very moment the photon is produced, it immediately decays into an electron-positron pair (the pair production is done in place). Accordingly, from now on photons won't be considered and leptons will be considered as able to directly pair produce. This hypothesis is justified in [13] and still allows us to model the cascade in a large variety of pulsars.

The second assumption is that a lepton emits a new electron-positron pair whenever it reaches a Lorentz factor γ_{thr}, as a very simple energy-based prescription. The ratio between the primary and combined secondary particle energies can be expressed as:

$$f = \gamma_{\text{pair}}/\gamma_{\text{thr}} \simeq \chi_\pm \tag{2.4}$$

where γ_{pair} is the Lorentz factor of the two secondary leptons right after their creation. The approximation is justified by the fact that, in the classical emission regime, the photon quantum parameter distribution has a sharp peak at $\chi_\gamma \simeq \chi_\pm^2$. For realistic pulsar parameters, $f \ll 1$ and $\gamma_{\text{pair}} > 1$. Finally, the energy $\gamma_{\text{pair}} m_e c^2$, is supposed to be equally split between the two leptons energy. Right after the

emission, the Lorentz factor of the emitting particle will then be $\gamma_{\rm thr}(1-f)$ and the two secondary leptons emitted will have $\gamma_{\rm pair}/2$.

Let us now suppose that the cascade occurs in an infinite vacuum gap with uniform background field E_0.

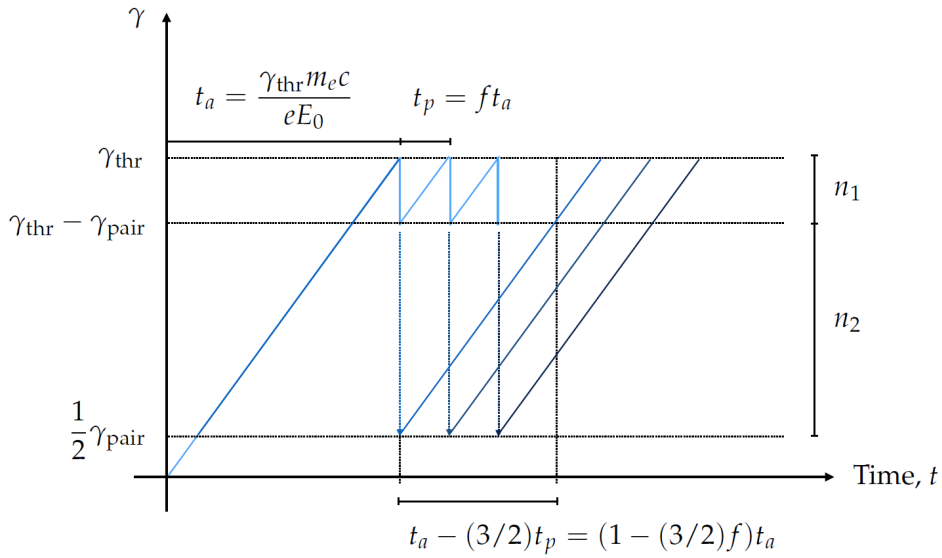

Figure 2.1: Schematic representation of heuristic pair production model and associated populations and time scales. Solid blue lines represent the time evolution of the Lorentz factor of leptons. When they reach a Lorentz factor γ_{thr}, leptons emit a pair with energy $\gamma_{pair} m_e c^2$. Emission times are indicated with blue dashed arrows, and new particles created at those times are shown with darker colors. The energy bands corresponding to populations 1 and 2 described in the text are indicated on the right hand side. Characteristic times t_a and t_p are also schematically indicated. Figure taken from [8]

As appreciable in Figure 2.1, plasma can be divided in two populations:
1) particles with a Lorentz factor $\gamma \in [\gamma_{\rm thr} - \gamma_{\rm pair}, \gamma_{\rm thr}]$,
2) secondary particles, with $\gamma \in [\gamma_{\rm pair}/2, \gamma_{\rm thr} - \gamma_{\rm pair}[$.
We hereby define two time scales relevant for the description of the system. The first one is the time required for particles to be accelerated from rest to $\gamma_{\rm thr}$, defined as $t_a \equiv \gamma_{\rm thr} m_e c/eE_0$, where e is the electron charge. The second one, $t_p \equiv f t_a$ is the time needed to accelerate particles from $\gamma_{\rm thr} - \gamma_{\rm pair}$ to $\gamma_{\rm thr}$, i.e. it is the period at which each particle in population 1 undergoes the QED processes responsible for the pair production. Since there is yet no forces to decelerate particles, the ones in population 1 are never converted into population 2, however particles in population 2, created due to pair production, are accelerated and get in the energy range of population 1 over a time $t_a - (3/2)t_p = (1-(3/2)f)t_a$ as appreciable in

Figure 2.1. The particle population equilibrium can be written as

$$n_1\left(t + (1-(3/2)f)t_a\right) = n_1(t) + (1-f)n_2(t) \tag{2.5}$$

where $n_{1,2}$ are the number of particles in each population. The factor $(1-f)$ is only a small correction, and removes from equation 2.5 the fraction of particles in population 2 at the time t that decelerates and counter-propagates with the bulk distribution. This small fraction can be written as $(1-3f/2)/(1-f/2) \simeq 1-f$ for $f \ll 1$ and corresponds to electrons emitted by positrons (or vice-versa) [8].

At each time interval $t_p \equiv ft_a$ the number of particles in population 2 increases thanks to pair production of both electrons and positrons in population 1, while the conversion to population 1 occurs via acceleration of particle in population 2. We can thus write:

$$\frac{\mathrm{d}n_2(t)}{\mathrm{d}t} \simeq \frac{2n_1(t)}{ft_a} - \frac{n_2(t)}{(1-3f/2)t_a} \tag{2.6}$$

It is possible to solve the system of coupled equations 2.5 and 2.6 assuming solutions of the type $exp(\Gamma t)$ such like $n_{1,2} = \overline{n}_{1,2}\exp(\Gamma t)$:

$$\begin{aligned} n_1 e^{\Gamma t_a(1-3/2f)} &= n_1 + n_2 & (2.7)\\ \Gamma n_2 &= \frac{2n_1}{t_p} - \frac{n_2}{t_a - 3/2t_p}\ , & (2.8) \end{aligned}$$

which leads to

$$e^{\Gamma t_a(1-3/2f)} = 1 + \frac{2/f}{\Gamma t_a + 1/(1-3/2f)}\ . \tag{2.9}$$

This is a difficult equation to solve analytically, but one that can be solved numerically for Γ given t_a and f.

Let us work out the case for which $\Gamma t_a \gg 1$ and $\Gamma f t_a = \Gamma t_p \ll 1$. This is equivalent to considering $t_p \ll t_a$, or equivalently $f \ll 1$. In these conditions, equation (2.9) simplifies to

$$e^{\Gamma t_a} \simeq \frac{2}{f\Gamma t_a}\ . \tag{2.10}$$

The problem is that we cannot expand the factor in the exponential. One can recast this equation in the form

$$xe^x = \frac{2}{f}, \tag{2.11}$$

which amounts now to find the argument of the Lambert W function, $W(x) = xe^x$ [19] for $W = 2/f$, where $x = \Gamma t_a$. There is an approximate solution $W(x) \simeq \ln x$, valid for $x > e$ (or for $f \ll 1$), which allows us to write

$$\Gamma \sim \frac{1}{t_a} \ln\left(\frac{2}{f}\right) \ . \tag{2.12}$$

From equation 2.8 and using the approximation given by equation 2.12 considering $f \ll 1$, it is possible to write the equilibrium condition

$$\frac{n_1}{n_2} \simeq \frac{f}{2} \ln(2/f) + \frac{f/2}{1 - 3f/2} \simeq \frac{f}{2} \ln(2/f) \tag{2.13}$$

i.e. that the ratio of particles in populations 1 and 2 is constant over time and only depends on f. Since $f \ll 1$, the number density at the screening time t_s is $n_s = n_1(t_s) + n_2(t_s) \simeq n_2(t_s)$. It is noteworthy that the factors "2" in equation 2.13 are the result of the presence of both the electrons and the protons in the gap that can pair emit when reaching $\gamma_{\rm thr}$.

2.3 Linear electric field

Despite it led to relevant results regarding the growth of a cascade process in the gaps, the model from Cruz et al. [13] did not account for the charge screening one could expect but only for a screening current. In this Thesis that model is generalized by using a time-space dependent electric field instead of a constant field in the gap as numerically described in [10]. Various aspects of the problem have been explored, step by step and under different angles through a quantitative analysis performed with variable scanning.

2.3.1 Initial setup for the linear field

The system considered is that of a plasma-filled magnetosphere with initial uniform density profiles of electrons $\rho_- = -2\,|\rho_{\rm GJ}|$ and positrons $\rho_+ = |\rho_{\rm GJ}|$, which assure the equilibrium of the system $\rho = \rho_- + \rho_+ = \rho_{\rm GJ}$ at time $t = 0$ when the gap opens. As in [13], without loss of generality, $\rho_{\rm GJ} = -\Omega B_*/2\pi c < 0$ has been chosen in order to reproduce the conditions of an aligned rotator ($\mathbf{\Omega} \parallel \mathbf{B}$). The plain sight of the cascade is the driving force for the cone of light to spread in the plasma at the pulsar polar caps.

From the initial density $\rho = \rho_{\rm GJ}$ setup, a vacuum gap develops as the electrons flow outward due to the externally-applied electric field, therefore generating a gap with a linear electric field inside of it, with $\mathbf{E} \cdot \mathbf{B} \neq 0$. As in [10] and in Figure 2.2, the gap contains just a fraction of the total positrons ρ_{GJ} defined as $\rho_{\rm gap} \equiv f_+\,|\rho_{\rm GJ}|$.

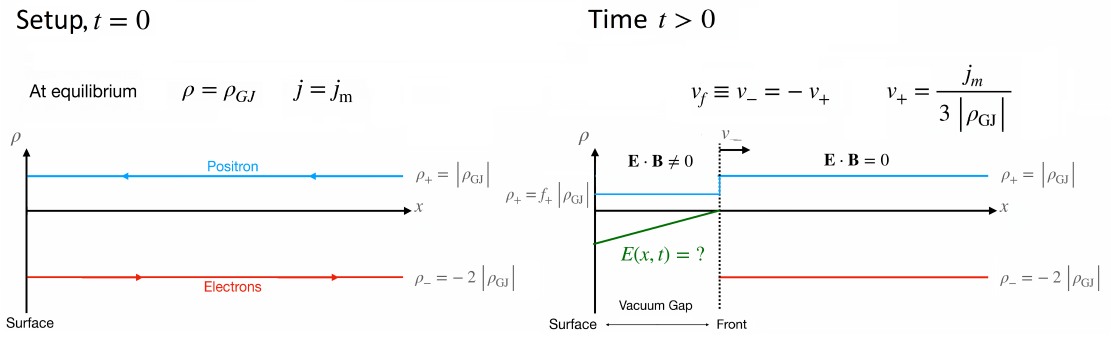

Figure 2.2: Initial setup at time $t = 0$ and system evolution at a generic time $t > 0$. The rightwards motion of electrons due to the external electric field results in a gap opening, hence to the creation of a linear electric field inside of it such that $\mathbf{E} \cdot \mathbf{B} \neq 0$.

The front, which represents the upper limit of the gap, moves at speed $v_f = v_-$. Knowing that the current density $j_\mathrm{m} \equiv \rho_- v_- + \rho_+ v_+$ by definition and that $v_- = -v_+$, it is possible to find

$$v_f = \frac{-j_m}{3\,|\rho_\mathrm{GJ}|} \tag{2.14}$$

Despite this very correlation stands only for the values of initial density that had been chosen, it's noteworthy underlining how the front velocity is fixed depending on the j_m, which can be treated - at least for now - as a free parameter. Since the front is composed by relativistic electrons we have $v_f < c$, therefore $j_\mathrm{m} < 3\rho_\mathrm{GJ}c$. Furthermore, as shown in [10], $j_m > 1.5\,|\rho_\mathrm{GJ}|\,c$, which corresponds to a front velocity $v_f > 0.5c$.

2.3.2 Linear Field regime

As electrons flow outwards (to the right, in our setup), the so-formed gap is characterized by a growing electric field. This field develops with a linear profile because of the capacitor-like setup, and scales linearly with both time and distance from the electrons population front up to the surface (at $x = 0$). The generic equation for the field will then be:

$$E(x,t) = a(t)x + b(t) \tag{2.15}$$

This is true only in the early stages of the gap opening, when the number of pairs created is still sufficiently low such that the zeroth order electric field is not affected by them filling the gap itself.

Initially, the vacuum gap only contains positrons with density $\rho = -f_+\rho_{\mathrm{GJ}}$ flowing towards the surface with speed which is assumed to be c in the gap, hence the presence of a current $j = -f_+ \left|\rho_{\mathrm{GJ}}\right| c$. Equations 1.3 and 1.4 can be extended with the introduction of ρ_{gap} and $\mathbf{j}_{\mathrm{gap}}$:

$$\nabla \cdot \mathbf{E} = 4\pi \left(\rho - \rho_{\mathrm{GJ}}\right) \equiv 4\pi\rho_{\mathrm{gap}} \tag{2.16}$$

$$\frac{\partial \mathbf{E}}{\partial t} = -4\pi \left(\mathbf{j} - \mathbf{j}_m\right) \equiv -4\pi\mathbf{j}_{\mathrm{gap}} \tag{2.17}$$

From equation 2.16 applied to 2.15 is possible to deduce $a(t) = 4\pi(1 + f_+)\left|\rho_{\mathrm{GJ}}\right|$. Using $j_m \equiv -\alpha \left|\rho_{\mathrm{GJ}}\right| c$, equation 2.17 can be rewritten as

$$\frac{\partial \mathbf{E}}{\partial t} = 4\pi \left(f_+ - \alpha\right) \left|\rho_{\mathrm{GJ}}\right| c \tag{2.18}$$

Since $E(x = 0, t) = b(t)$, it's possible to find $b(t) = 4\pi \left(f_+ - \alpha\right) \left|\rho_{\mathrm{GJ}}\right| c \cdot t + C$ by integrating 2.18. The boundary condition $E(x = v_f t, t) = 0$ is imposed considering that the electric field is completely screened out of the vacuum gap. Equation 2.15 than becomes:

$$E(x, t) = 4\pi(1 + f_+) \left|\rho_{\mathrm{GJ}}\right| \left(x - v_f t\right) \tag{2.19}$$

which is valid for a lepton in the gap, i.e. for $x < v_f t$. The use of parameters like α and f_+ is supported by the quest for self-consistency between the parameters used in the numerical simulation, as later shown in Chapter 3.

Knowing the electric field profile, it is now possible to write the momentum equation for the leptons (with subscript + or - for positrons or electrons, respectively) by assuming that their speed is equal to c in the gap and using $p_\pm \simeq \gamma_\pm mc$, where $p_\pm$ is the momentum, $\gamma_\pm$ is the Lorentz factor:

$$\frac{d\gamma_\pm}{dt} = \frac{-e}{m_e c} E(x, t) = \frac{-4\pi e}{m_e c}(1 + f_+) \left|\rho_{\mathrm{GJ}}\right| \left(x - v_f t\right) \tag{2.20}$$

Since this very analytical model has been later compared with numerical simulations, it has been necessary to normalize the problem to OSIRIS units: $\left|\rho_{\mathrm{GJ}}\right| = e \times n_{\mathrm{GJ}}$ and, as in OSIRIS, the equivalent of a plasma frequency ω_0 and n_0 are defined as:

$$\frac{4\pi e^2 n_0}{m_e} = \omega_0^2 \equiv \left(\frac{c}{r_*}\right)^2 \tag{2.21}$$

Finally, let $\overline{n_{\mathrm{GJ}}} = (1 + f_+) n_{\mathrm{GJ}}/n_0$. By setting $c = 1, n_0 = 1, \omega_0 = 1$ and $\overline{v_f} = v_f/c$, the equation of motion becomes:

$$\frac{d\gamma_\pm}{dt} = \overline{n_{\rm GJ}}\left(\overline{v_f}t - x\right) \tag{2.22}$$

Depending on the nature of the lepton, $x = x_i \mp (t - t_i)$, where x_i is the position of the lepton at time t_i. By integrating equation 2.22 between time t_i and time t, we get:

$$\gamma_\pm(t) - \gamma_\pm\left(t_i\right) = \overline{n_{\rm GJ}}\left(\frac{t^2 - t_i^2}{2}\left(\overline{v_f} \pm 1\right) \mp \left(t_i \pm x_i\right)\left(t - t_i\right)\right) \tag{2.23}$$

This can be written as a second order equation for t:

$$\frac{\gamma_\pm(t) - \gamma_\pm\left(t_i\right)}{\overline{n_{\rm GJ}}} = t^2\left(\frac{\overline{v_f} \pm 1}{2}\right) \mp t\left(t_i \pm x_i\right) + t_i\left(\frac{t_i}{2}\left(\overline{v_f} \pm 1\right) - \left(t_i \pm x_i\right)\right) \tag{2.24}$$

The determinant of this problem reads

$$\begin{aligned}\Delta &= \left(t_i \pm x_i\right)^2 - \frac{4}{2}(\overline{v_f} \pm 1)\left[-(t_i \pm x_i)t_i - \frac{\gamma - \gamma_i}{\overline{n_{\rm GJ}}} + \frac{\overline{v_f} \pm 1}{2}t_i^2\right], \\ &= \left(x_i - \overline{v_f}t_i\right)^2 \pm \frac{2(\gamma - \gamma_i)(1 \pm \overline{v_f})}{\overline{n_{\rm GJ}}}.\end{aligned}$$

Then

$$t_- = \frac{t_i - x_i}{1 - \overline{v_f}} - \sqrt{\left(\frac{\overline{v_f}t_i - x_i}{1 - \overline{v_f}}\right)^2 - \frac{2\left(\gamma(t) - \gamma\left(t_i\right)\right)}{\left(1 - \overline{v_f}\right)}\frac{1}{\overline{n_{\rm GJ}}}} \tag{2.25}$$

$$t_+ = \frac{t_i + x_i}{1 + \overline{v_f}} + \sqrt{\left(\frac{\overline{v_f}t_i - x_i}{1 + \overline{v_f}}\right)^2 + \frac{2\left(\gamma(t) - \gamma\left(t_i\right)\right)}{\left(1 + \overline{v_f}\right)}\frac{1}{\overline{n_{\rm GJ}}}} \tag{2.26}$$

The signs in front of the square roots are chosen so that $t_\pm$ increases with $\gamma(t)$.

It is now possible to compute the times $t_p(t)$ and $t_a(t)$ according to their definition: for instance, t_a is the time required to accelerate a particle from $\gamma_{\rm pair}/2$ at time t_i to $\gamma_{\rm thr}$ at time t, hence $t_{a\pm} \equiv t_\pm - t_i$:

$$t_{a-}(t_i) = \frac{\overline{v_f}t_i - x_i}{1 - \overline{v_f}} - \sqrt{\left(\frac{\overline{v_f}t_i - x_i}{1 - \overline{v_f}}\right)^2 - \frac{2\gamma_{\rm thr}\left(1 - f/2\right)}{\left(1 - \overline{v_f}\right)}\frac{1}{\overline{n_{\rm GJ}}}} \tag{2.27}$$

$$t_{a+}(t_i) = \frac{-\overline{v_f}t_i + x_i}{1 + \overline{v_f}} + \sqrt{\left(\frac{\overline{v_f}t_i - x_i}{1 + \overline{v_f}}\right)^2 + \frac{2\gamma_{\rm thr}\left(1 - f/2\right)}{\left(1 + \overline{v_f}\right)}\frac{1}{\overline{n_{\rm GJ}}}} \tag{2.28}$$

while t_p, by definition, is the time required to accelerate a lepton from $\gamma_{\text{thr}} - \gamma_{\text{pair}}$ to γ_{thr}, hence:

$$t_{p-}(t_i) = \frac{\overline{v_f} t_i - x_i}{1 - \overline{v_f}} - \sqrt{\left(\frac{\overline{v_f} t_i - x_i}{1 - \overline{v_f}}\right)^2 - \frac{2\gamma_{\text{thr}} f}{(1 - \overline{v_f})} \frac{1}{\overline{n_{\text{GJ}}}}} \tag{2.29}$$

It is noteworthy that, since all the leptons are relativistic (supposed to be moving at c), the problem is only time dependent because x_i is in the form $x_i = x_0 \pm c(t_i - t_0)$. Furthermore, it is remarkable how the difference between electrons and protons is embodied by the reverse sign in the speed and in the square root argument.

2.3.3 Layers and characteristic times

Analytically describing the whole cascade is quite nontrivial because of the high non-linearity of the processes involved, the self-consistency of the phenomena to be addressed and the successive optimization of the numerical analysis to be performed. Together with the few approximations regarding the physics of the phenomena (such like the zero-MFP for the photons) it becomes necessary to divide the whole process into sub-processes, which are easier to approach analytically and lighter to be computed.

By considering time scales for which the number of leptons is small enough in order not to perturb the externally-imposed electric field, it is possible to assume that all the leptons are substantially independent from each other. Thanks to this assumption, in a preliminary approach it is possible to consider only the electrons in the gap while neglecting the presence of the positrons, both the ones originally present in the magnetosphere (primary e^+) and the ones that have been pair-produced (secondary e^+). Specifically, for the moment the only leptons able to pair produce will be the electrons, and the will only emit electrons in the cascade. Furthermore, the variables $t_a(t)$ and $t_p(t)$ will be referred to the electrons, hence equations 2.27 and 2.29) will be the ones considered.

Because all the electrons in the gap move at c, the cascade is described as occurring in a succession of layers of infinitesimal width moving at c towards the positive values of x. The whole cascade process can be then subdivided into different phases, according to the following scheme.

- Phase 1) : As the gap gradually opens, positrons start being accelerated towards the surface as soon as the front reaches their position in the initial distribution. The very first ones subjected to the linear electric field, due to their proximity to the surface, collide with it before being able to reach γ_{thr}, hence they are absorbed without undergoing any pair production. Let $t_{\text{Phase 1}}$ be the time at which the front reaches the very first positron that could be accelerated to γ_{thr} right before hitting the surface in $x = 0$. The position of this positron can be considered to be the layer of infinitesimal width located in $x = v_f t_{\text{Phase 1}}$.

- Phase 2) : The positrons produces at $t = t_{\text{Phase 1}}$ in $x = 0$ an electron-positron pair. While the so-produced positron is instantly absorbed by the surface, the electron created with $\gamma = \gamma_{\text{pair}}/2$ starts being accelerated by the gap field while moving at c towards the front moving at v_f. The layer it belongs to, which is moving rightwards at c as well, will be the focus of the model, since the layers to the right do not present any electrons accelerating towards the front as stated in Phase 1, while the ones to the left could be momentarily considered as "copies" of it (more on this in Chapter 3). In the available time before it reaches the front of the gap, this electron hits γ_{thr}, pair produces other electrons on site and starts being re-accelerated from $\gamma_{\text{thr}} - \gamma_{\text{pair}}$ several times. It is worth noticing how the so-produced secondary (and even further generation) electrons move at c with their progenitor since they are assumed to move basically at c.
- Phase 3) : The cascade process ends when the electrons layer under the focus reaches the gap front; here the electric field vanishes, hence the leptons couldn't be accelerated anymore to γ_{thr} and pair produce.

This whole scheme and, particularly, the evolution of the number of particles in each layer are fully determined by the time $t_{\text{Phase 1}}$ when the positron from the front enters the gap, which in turn has to be already wide enough so that the electric field inside is sufficiently strong to accelerate the positron to γ_{thr}. Phase 1 can thus only occur after a time $t_{\text{Phase 1}}$ that satisfies $v_f t_{\text{Phase 1}} > c t_{A+}(x = v_f t_{\text{Phase 1}})$, since the positron has to be sufficiently far apart from the surface to be accelerated to γ_{thr} in a time t_{A+} evaluated in the gap front position $x = v_f t_{\text{Phase 1}}$. This condition, applied to equation 2.28, leads to

$$t_{\text{Phase 1}} > \tau_* = \frac{1}{\overline{v_f}} \sqrt{\frac{2\left(\gamma_{\text{thr}} - 1\right)}{\left(1 + \overline{v_f}\right)} \frac{1}{\overline{n_{\text{GJ}}}}} \sim \sqrt{\frac{\gamma_{\text{thr}}}{\overline{n_{\text{GJ}}}}} \tag{2.30}$$

for which an initial $\gamma = 1$ has been considered, since the positron was still before being reached by the gap front.

From now on, only the layer that left the front at time $t_{\text{Phase 1}} = \tau_*$ will be considered, meaning that the first electron is produced right on the stellar surface. Let us now introduce some notations. The positron emitted at time τ_* takes a time $t_{a+}(\tau_*)$ to reach the surface of the star where it can produce the first pair. $\tau_0 = \tau_* + t_{a+}(\tau_*)$ is hence defined as the time when the first generation electron is emitted at $x_0 = 0$, i.e. on the surface of the star. By imposing $x_i = c(t - \tau_0)$, which corresponds to $t - \tau_0$ in normalized quantities, equation 2.29 for the seed layer of that progenitor can be rewritten as:

$$t_p(t) = \frac{\tau_0}{1 - \overline{v_f}} - t - \sqrt{\left(\frac{\tau_0}{1 - \overline{v_f}} - t\right)^2 - \frac{2\gamma_{\text{thr}} f}{\left(1 - \overline{v_f}\right)} \frac{1}{\overline{n_{\text{GJ}}}}} \tag{2.31}$$

It is worth underlining how $t_{p,a}(t)$ are then sums of a linear term and a square root term: this becomes relevant in the analysis of the numerical simulations performed in Chapter 3.

Since the choice of $\overline{n_{\mathrm{GJ}}}$ used in OSIRIS simulations directly reflected the average Goldreich-Julian density normalized by $1+f$ as shown in equations 2.20 and 2.22, the problem now considered only depends on three parameters: f, γ_{thr} and $\overline{v_f}$.

It takes a time $t_a(\tau_0)$ for the progenitor electron to reach γ_{thr}, hence $\tau_1 = \tau_0 + t_a(\tau_0)$ can be defined as the time at which the first generation electron emits its first electron. Then at time $\tau_1 + t_p(\tau_1)$ it emits a second electron and so on.

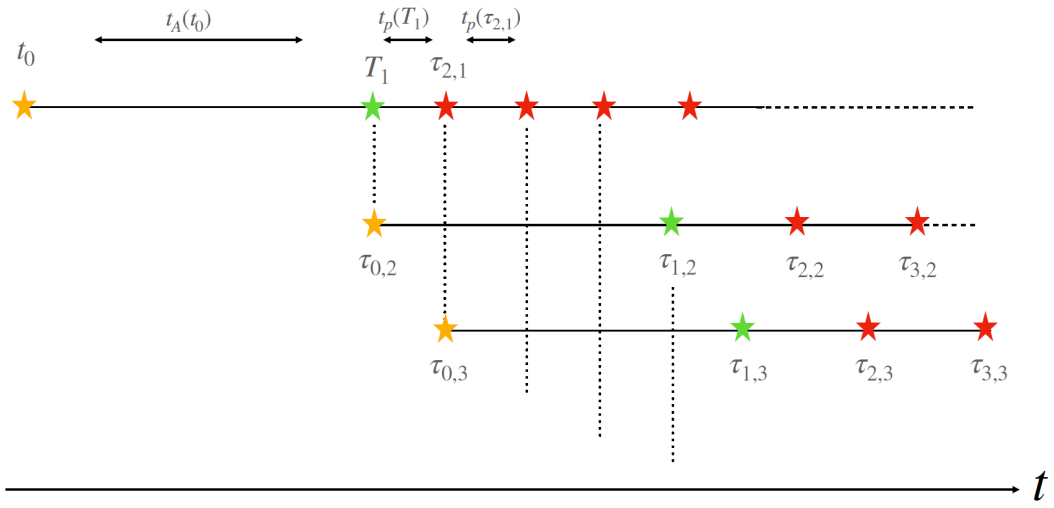

Figure 2.3: Illustration of the cascade in a layer. One horizontal line represents one electron. The yellow stars represent the moment an electron is born with $\gamma = \gamma_{\mathrm{pair}}/2$. The green stars represent the moment an electron reaches γ_{thr} for the first time. The red stars represent the production of electron every $t_p(t)$. Some useful time labels are used according to the notation expressed in 2.32; t_0 is what was previously defined as τ_0 (more precisely, $\tau_{0,1}$), while T_1 stands for τ_1 ($\tau_{1,1}$).

In order to assess the time dependency of the cascade process, a useful sequence of timestamps (conceptually shown in Figure 2.3) has been introduced:

$$\begin{cases} \tau_{1,i} \\ \tau_{n+1,i} = \tau_{n+1,i} + t_{p-}(\tau_{n+1,i}) \end{cases} \tag{2.32}$$

$\tau_{1,i}$ is the time when the i^{th} electron reaches γ_{thr} for the first time, while $\tau_{n,i}$ is the time when the i^{th} electron reaches γ_{thr} for the n^{th} time.

By paying closer attention to equations 2.29 and 2.27 it is noticeable that the two functions share the same time dependence. The main difference between them stands in the multiplying factor in front of $\gamma_{\rm thr}$, which is a direct consequence of the fact that $t_p(t)$ is defined on a smaller interval than $t_a(t)$.

It is therefore possible to evaluate the time at which the cascade process ends by considering two possible events. The first possible condition for which the whole process concludes is when the electron layer moving at c catches up with the gap front moving at $v_f < c$. The other situation that leads the almost-exponential cascade to an end is when $t_a(t)$ is no longer defined, i.e. the electrons produced in the layer are subjected to an electric field which is too low for them to be accelerated to $\gamma_{\rm thr}$, hence to be able to pair produce anymore. According to this, the time t that marks the conclusion of the cascade is

$$t_{\rm end} = \frac{\tau_0}{1-\overline{v_f}} - \sqrt{\frac{2\gamma_{\rm thr}(1-f/2)}{(1-\overline{v_f})}\frac{1}{\overline{n_{\rm GJ}}}} \tag{2.33}$$

This $t_{\rm end}$ should depend only slightly on the f parameter since $f \ll 1$, while it should significantly increase with v_f.

2.4 Differences between the two models

For what concerns the particle growth rate, hence the capability of the cascade process to replenish the gap, the constant field and spatio-temporal linear field models differ mainly differ according to the characteristic times t_p and t_a. More precisely, while in the constant field regime the two values are fixed depending on the initial distribution in the particle densities and the plasma current, if we consider the linearly-growing field $t_p(t)$ and $t_a(t)$ depend on time as well.

In order to better structure the analytical model for the processes involved and being able to use it as a framework for the numerical analysis foreseen, it becomes crucial to address the dependency of the functions previously described on the parameters that can be varied.

From the definition of $t_p(t)$ and $t_a(t)$ in equations 2.27 and 2.29, it can be shown that $\partial t_{\rm p,a}/\partial t > 0$. Physically, the electrons are flowing from the surface ($x = 0$), a region of high electric field, to the gap front, a region in which the electric field vanishes. Subsequently, it takes longer and longer time for the leptons to be accelerated to $\gamma_{\rm thr}$. This time-dependency can be appreciated in Figure 2.4, in which the investigated functions have been plotted with different parameters and compared.

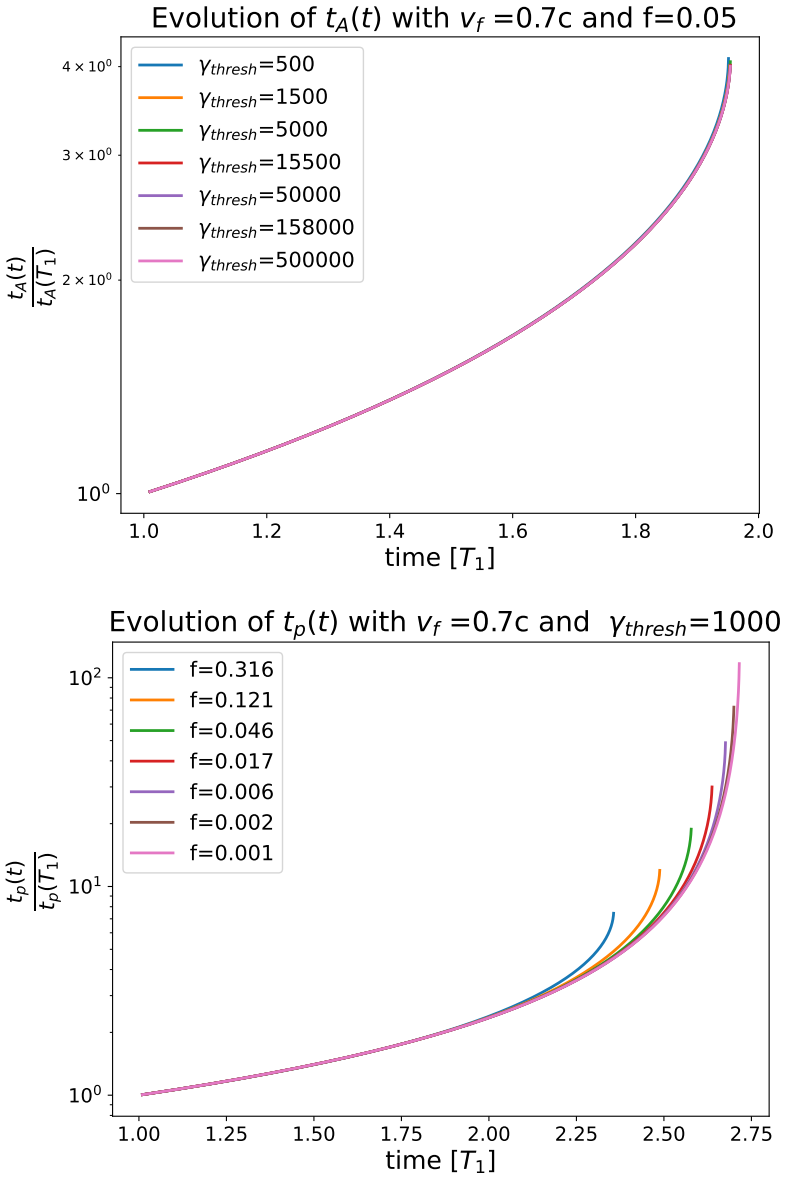

Figure 2.4: Top: time evolution of function $t_a(t)$ for different values of $\gamma_{\text{thr}} \in [500; 5 \cdot 10^6]$ with $v_f = 0.7c$ and $f = 0.05$. The function is normalized to its first value of interest $t_a(T_1)$ and time itself is normalized to T_1 (previously referred to as τ_1).
Bottom: Evolution of function $t_p(t)$ with time for different values of $f \in [0.316,0.001]$ with $v_f = 0.7c$ and $\gamma_{\text{thr}} = 1000$. All the curves share a common part for $t \in [T_1,2T_1]$. After that, depending on the value of f, the $t_p(t)$ start diverging at different timestamps.

It is immediately noticeable that, for a fixed values of f and $\overline{v_f}$ and with time normalized to T_1, $t_a(t)$ and $t_p(t)$, hence the whole problem, do not depend on the value of γ_{thr}.

It is also noteworthy how, when fixing the value for γ_{thr}, $t_a(t)$ and $t_p(t)$ are roughly linear up to $t \sim 1.8\ T_1$ and how, by this time, they are only multiplied by a factor 2. It can be deduced that, during this time lapse, the number of pairs is increasing almost exponentially if one admits that t_a is kind of constant.

Let us now introduce a local exponential growth rate, namely $\Gamma(t) = d\ln(N)/dt$ where N is the total number of electrons in the gap. $\Gamma(t)$ is the key element to fully describe the evolution of the number of particles in one layer, later generalized to the behaviour of the whole gap.

If $t_p(t)$ increases, the growth rate will decrease accordingly since it would take more time for an electron to reach γ_{thr} and populate the layer through pair creation. More precisely, $t_p(t)$ is evolving linearly and slowly varying when the square root part is almost constant since

$$\left(\frac{t_0}{1-\overline{v_f}} - t\right)^2 \ll \frac{2\gamma_{\text{thr}}}{(1-\overline{v_f})}\frac{f}{\overline{n_{\text{GJ}}}} \tag{2.34}$$

For $f \ll 1$, this approximation is valid for a larger time interval if v_f is close to c.

2.5 Growth in time

When considering a constant electric field setup, it is straightforward to determine that the two relevant timescales $t_{a,p}$ are also constant, therefore the growth of the cascade is exactly exponential for $t \gg t_a$, as shown in section 2.2. Rigorously determining the evolution in time of the number of particles in the cascade with the time and space dependent t_a and t_p is a challenging task. Moreover, with such time and space dependence, it is not straightforward that a pure exponential behavior similar to that observed for a constant electric field occurs.

Since functions $t_{p,a}(t)$ are increasing with time for electrons, equations 2.5 and 2.6 are still valid for a linear electric field. However, their analytical solution is really hard to find as, even in the easiest case, the equations are dilation equations (e.g. $f(2t) = f(t)$) that cannot be easily solved by classical techniques such as Laplace transform.

The purpose of the theoretical models described hereafter is to determine the evolution of the growth rate of the cascade $\Gamma(t)$ as a function of time and of the parameters f, γ_{thr} and $\overline{v_f}$.

2.5.1 Continuous approach

When $t_{p,a}$ vary with time, one has to consider another type of solution. The one sought is for a scenario where t_a and t_p are slowly varying, such that one may have a local growth rate. The form of the solution is then changed from $n_{1,2}(t) = \overline{n_{1,2}} \exp(\Gamma t)$ to an evolving $n_{1,2}(t) = \overline{n_{1,2}} \exp\left(\int_{t_a(T_1)}^{t} \Gamma(t')\, \mathrm{d}t'\right)$, where $t_a(T_1)$ is approximately the time when the cascade starts to be exponential. With this definition, the particle population can be described with $n_{1,2}(t) = \overline{n_{1,2}} \exp(u(t))$. This approximation is valid when $t_p(t)$ and $t_a(t)$ are almost linear and slowly evolving, which corresponds to the case where v_f is close to c according to equation 2.34 (e.g. $v_f \gtrsim 0.7c$ and $f \lesssim 0.05$).

First, it is assumed that, on the portion of time considered, $t_p(t) \simeq f t_a(t)$, therefore $t_a(t) - 3/2 t_p(t) \simeq t_a(t)$ since $f \ll 1$. This assumption is valid as long as the layer is far from the front of the gap. In these conditions, it is possible to re-write equations 2.5 and 2.6 as:

$$n_1\left(t + t_a(t)\right) \simeq n_1(t) + n_2(t) \tag{2.35}$$

$$\frac{\mathrm{d}n_2(t)}{\mathrm{d}t} \simeq \frac{n_1(t)}{f t_a(t)} - \frac{n_2(t)}{t_a(t)} \tag{2.36}$$

It is worth noticing that the first term on the right-hand side of equations 2.6 and 2.36 differs by a factor of 2 because, in the case of a linear electric field, the growth in the number of electrons is caused only by pair production events triggered by primary electrons (and not positrons).

Given the results given in section 2.2 and the rationale above, it is reasonable to assume that the solution of this system can be written with the WKB approximation

$$n_{1,2}(t) \propto \exp\left(\int_{t_a^*}^{t} \Gamma(t')\ \mathrm{d}t'\right) \tag{2.37}$$

where $\Gamma(t')$ is the local (in time) growth rate of the cascade at time t' and $t_a^* = t_a(T_1)$ is the time in which $n_{1,2}$ start to grow exponentially, which can be estimated as the time of creation of the second generation of electrons. Plugging $n_2(t)$ into equation 2.36, it is possible to write

$$\frac{n_2(t)}{n_1(t)} = \frac{1}{f(\Gamma(t) t_a(t) + 1)} \tag{2.38}$$

Equation 2.35 then becomes:

$$n_1\left(t + t_a(t)\right) = n_1(t)\left(1 + \frac{1}{f}\frac{1}{\left(\Gamma(t) \times t_a(t) + 1\right)}\right) \tag{2.39}$$

Given that, as it was for the constant field model, $(\Gamma(t)t_a(t)+1) > 1$ for $f \ll 1$:

$$\int_t^{t+t_a(t)} \Gamma(t')\,\mathrm{d}t' \simeq \frac{1}{f\Gamma(t)t_a(t)} \tag{2.40}$$

Assuming that $\Gamma(t)$ varies slowly during a time $t_a(t)$, it is possible to use its Taylor expansion $\Gamma(t') \simeq \Gamma(t) + (t-t')\dot{\Gamma}(t)$ to obtain:

$$\int_t^{t+t_a(t)} \Gamma(t')\,\mathrm{d}t' \simeq \Gamma(t)t_a(t)\left(1+\frac{\dot{\Gamma}(t)t_a(t)^2}{2\Gamma(t)}\right) = \Gamma(t)t_a(t)\left(1+\psi(t)\right) \tag{2.41}$$

Plugging this result in equation 2.35 and using equation 2.38 leads to

$$\exp\left[\tilde{\Gamma}(t)t_a(t)\right] \simeq \frac{1+\psi(t)}{f\tilde{\Gamma}(t)t_a(t)}\ , \tag{2.42}$$

where $\tilde{\Gamma}(t) = \Gamma(t)(1+\psi(t))$. The solution of equation 2.42 yields a correction to equation 2.12,

$$\Gamma(t)t_a(t) = \frac{1}{1+\psi(t)} W\left(\frac{1+\psi(t)}{f}\right)\ . \tag{2.43}$$

This is not a fully closed form of $\Gamma(t)$, since ψ is a function of Γ and $\dot{\Gamma}$. Assuming that $t_a(t) \simeq t_a(T_1)(1+Ct)$, where $C \ll 1$ is a constant, we can get ψ to the lowest order when $\Gamma(t)t_a(t) \simeq W(1/f)$,

$$\psi \simeq \frac{Ct_a(T_1)}{W(1/f)} \ll 1\ . \tag{2.44}$$

2.5.2 Discrete approach

In the early stages of this Thesis' workflow, the PIC simulation tool was non-trivial to be approached, both due to the training needed to be used and to the computational efforts that lead to extensive time required to run the simulations themselves. Therefore, in order to grasp initial understanding and confirmations of the problem, some heuristic simulations have been performed through Python coding.

A preliminary program aimed at numerically solving the coupled equations 2.27 and 2.29 by using a centered Euler scheme, hence leading to the evolution of $n_1(t)$ and $n_2(t)$, considering those functions as continuous. Since it was not possible to precisely establish the time at which electrons are created in the gap, the distribution functions derived this way were unreliable.

Here the necessity to adopt a new algorithm, in which each electron is represented by a list. Starting with the first electron created at time τ_0, whose list is $[\tau_0]$, the program keeps track of every event of pair production by updating the current lists and creating new ones (corresponding to freshly created electrons). For example, at time τ_1 the lists are $[[\tau_0, \tau_1], [\tau_1]]$, meaning that two electrons are in the layer; the next step, corresponding to a time increase of $t_p(\tau_1)$, updates the lists in the following way: $[[\tau_0, \tau_1, \tau_1 + t_p(\tau_1)], [\tau_1], [\tau_1 + t_p(\tau_1)]]$. The program updates at each time-step both the t_p between the pair production events and the t_a necessary to accelerate the newly-born electrons.

This numerical approach can be described theoretically as a sequence ruled by intervals of duration $t_a(t)$ and $t_p(t)$ over considering the number of particles as a continuous function of time. According to equation 2.31, it is possible to write $t_p(t) = A - t - \sqrt{(A-t)^2 - B}$, where $A = \tau_0/(1-\overline{v_f})$ and $B = 2f\gamma_{\text{thr}}/\left(1-\overline{v_f}\right)\overline{n_{\text{GJ}}}$. From the system 2.32, it is possible to deduce by recursion the sequence of all the timestamps $\tau_{n,i}$ when the i^{th} electron pair-produces, given the time $\tau_{1,i}$ when it reaches the threshold for the first time:

$$\begin{cases} \tau_{1,i} \\ \tau_{n,i} = A - \sqrt{\left(A - \tau_{1,i}\right)^2 - (n-1)B} \end{cases} \tag{2.45}$$

For a given time t, $\tau_{1,i} < t \ \forall i < i_{\max}$, which allows to determine the maximum number of generations $i_{\max}$ able to produce pairs every $t_p(t)$ at a given time t.

The main issue is then determining how $\tau_{1,i}$ evolves as a function of i. The intrinsic limit of this kinetic model emerges because $t_{p,a}(t)$ actually varies in time: $t_a(t) + t_p(t + t_a(t)) \neq t_p(t) + t_a(t + t_p(t))$. This implies that, after a sufficiently long time, there might be an almost continuous γ-distribution.

2.5.3 Asymptotic Regime: Linear $t_p(t)$

In this section the behaviour of t_p is further investigated by considering it to be a linear function of time and slowly evolving, which corresponds to the case where v_f is close to c according to equation 2.34 (e.g. $v_f \gtrsim 0.7c$ and $f \lesssim 0.05$). This assumption is clearly valid for time intervals in the order of magnitude of T_1 ($\tau_{1,1}$) as shown on the left panel of figure 2.5. In these conditions, after a time sufficiently long for the exponential cascade to develop, it is clearly visible on the right panel of Figure 2.5 that:

$$\tau_{1,i} = a\ln(i) + b \tag{2.46}$$

It is possible to compute $i_{\max}$ using $(\tau_{1,i} < t \ \ \forall\ i < i_{\max}) \Rightarrow i_{\max} = \lfloor \exp\left((t-b)/a\right) \rfloor$.

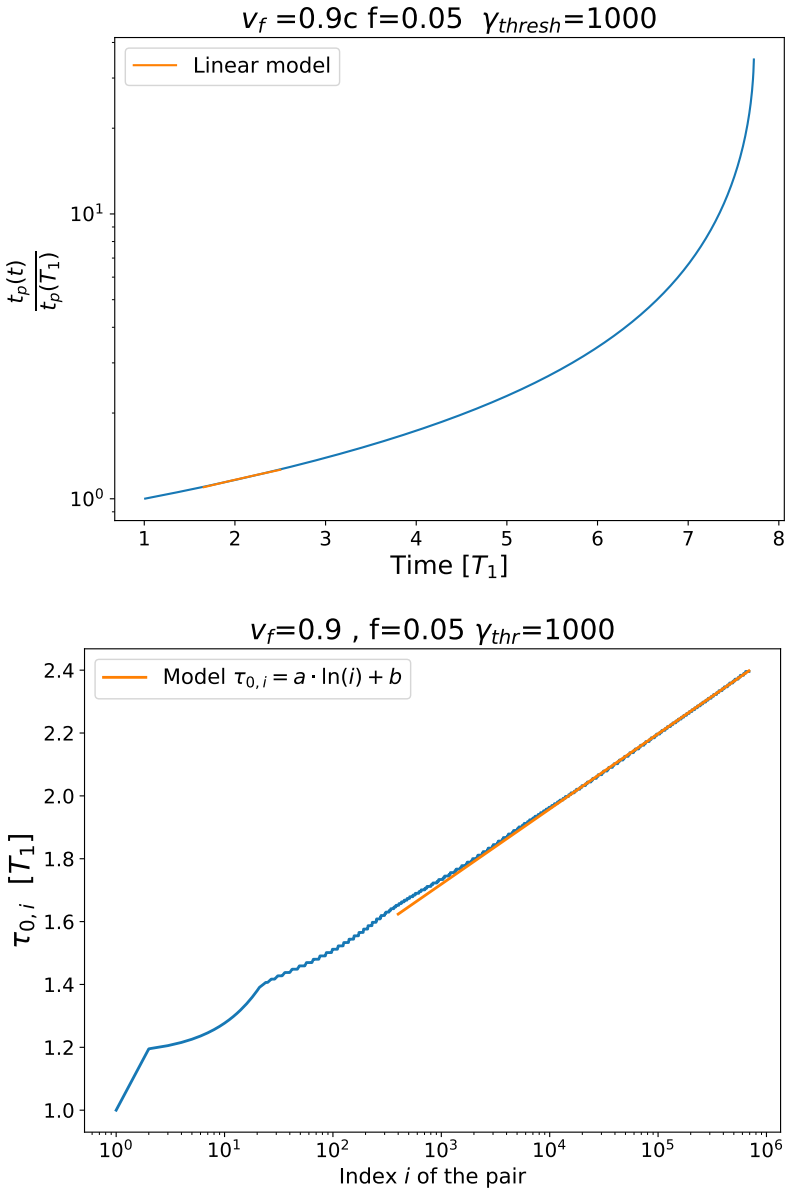

Figure 2.5: Top: Evolution of $\tau_{1,i}$ as a function of i for $v_f = 0.5$, $f = 0.05$, $\gamma_{\text{thr}} = 1000$. When $t_p(t)$ slowly varies in time, the $\tau_{1,i}$ function can be accurately fitted by a model $a \ln(i) + b$. Here $a \times T_1 = 0.104$ and $b/T_1 = 1$.
Bottom: Evolution of normalized $t_p(t)$ with respect to T_1. For those values v_f and f considered, the function can be well approximated by a linear model $f(t) = 0.20t + 0.77$ in normalized units.

The number of particles $n_i(t)$ produced at time t by the i^{th} electron is given by the condition $\tau_{n,i} < t$:

$$n_i(t) = \frac{(A - a\ln(i) - b)^2 - (A - t)^2}{B} \tag{2.47}$$

Then the total number of electrons, given by $N(t)$, can be obtained by summing all the $n_i(t)$ on i in the range $[1; i_{\max}]$:

$$N(t) = \sum_{i=1}^{i_{\max}} \frac{(A - a\ln(i) - b)^2 - (A - t)^2}{B} \tag{2.48}$$

$$\begin{aligned} N = {} & \frac{\exp\left(\frac{t-b}{a}\right)}{B}\left[-t^2 + 2At + b(b - 2A)\right] + \\ & + \frac{1}{B}\left[2a(b - A)\ln\left(i_{\max}!\right) + \sum_{i=1}^{i_{\max}} a^2\ln^2(i)\right] \end{aligned} \tag{2.49}$$

The total number of particles in the layer can be approximated by an exponential with a growth rate $1/a$ modulated by a polynomial.

The term $\ln(i_{\max}!)$, which is an exponential too, can be computed by using the Stirling's approximation: $\ln(i_{\max}!) \sim i_{\max}\left(\ln(i_{\max}) - 1\right) = (t - b - a)/a \times \exp\left((t - b)/a\right)$. For the term

$$\sum_{i=1}^{i_{\max}} a^2\ln^2(i) \tag{2.50}$$

since $\ln(x)^2$ is a monotonically increasing function, then:

$$\int_2^{i_{\max}+1} \ln(x - 1)^2\,\mathrm{d}x \leq \sum_{i=1}^{i_{\max}} \ln(i)^2 \leq \int_1^{i_{\max}+1} \ln(x)^2\,\mathrm{d}x \tag{2.51}$$

It can therefore be approximated by

$$\sum_{i=1}^{i_{\max}} \ln(i)^2 \sim i_{\max}\left(\ln(i_{\max})^2 + 2 - 2\ln(i_{\max})\right) = \left(\left(\frac{t - b}{a} - 1\right)^2 + 1\right) i_{\max} \tag{2.52}$$

The total number of electrons $N(t)$ can be then expressed as:

$$N(t) = \frac{\exp\left(\frac{t-b}{a}\right)}{B}\left(-2at + 2a(A + a)\right) \tag{2.53}$$

2.6 Growth in space

In order to extend the analysis presented above from one to multiple electron layers, other sets of simulations, later shown in Chapter 3, have been performed starting with a uniform positron distribution and externally imposing the electric field, which is chosen to be negative when the gap is opened. Positrons are accelerated as the gap opens, pair producing close to the surface and triggering the cascade process. Fresh electrons are then accelerated towards the magnetosphere, with each of them developing its own single-layered cascade. Since the initial uniform positron distribution, a multi-layered cascade is generated in this case. However, all layers move at approximately the speed of light, so each layer behaves according to the model outlined in the previous sections. For the sake of calculation, we set the growth of particles the layer k to be

$$N_k(t) = N_0 \exp\left(\int_{t_k}^{t} \Gamma(t')dt'\right) \quad \text{with} \quad \Gamma(t)t_a(t) \simeq W(2/f) \tag{2.54}$$

according to the results obtained in section 2.2, where t_k denotes the time at which the layer has been created.

For the first layer, let $t_1 = 0$ and thus $t_k = kt_p$ since the subsequent layers of seed electrons will be created every t_p. Layers are assumed to be of width ct_p, with the further assumption that the electron density inside them is uniform, hence equal to $n_k = N_k/(ct_p)$. It follows that

$$n_{k-1}(t) = n_k(t) \exp\left(-\int_{t-t_p}^{t} \Gamma(t')dt'\right) \tag{2.55}$$

If the electric field varies slowly in space, $n_{k-1} \simeq n_k e^{-\Gamma t_p}$. The argument of the exponential is $\Gamma t_p = fW(1/f)$, which is much smaller than unity for $f \ll 1$. Therefore, the density between layers does not vary abruptly. This is a key ingredient to determine the continuous profile (or the envelope) of the density histogram. Equation(2.55) can be rewritten in the following manner:

$$n_k(t) = n(x_k, t) \tag{2.56}$$
$$n_{k-1}(t) = n(x_k - ct_p, t) \tag{2.57}$$

with x_k being the position of the k layer moving at the speed of light. We can proceed to the calculation of the profile by expanding $n(x - ct_p, t) \simeq n(x) - ct_p\partial_x n = n(x)e^{-\Gamma t_p}$, which leads to

$$n(x, t) = n_0 \exp\left(\Gamma(t + x/c)\right) \tag{2.58}$$

This estimate holds for as long as the growth rate of individual layers is approximately the same, *i.e.*, while the number of electrons in each layer is dominantly determined by the life time of that layer. This condition can be written as $t\dot{\Gamma}(t)/\Gamma(t) \ll 1$, which is valid in early times of the cascade.

Chapter 3

Simulation results

3.1 Coding and post-processing

The analytical models presented in Chapter 2 have been thoroughly tested with and validated against 1D PIC simulations performed via the OSIRIS code. To those followed, firstly, a preliminary visualization of the simulation outputs through the VisXD tool, a set of data analysis and visualization routines based on IDL developed at GoLP; subsequently, if the outputs met the expectations, more detailed post-processing analysis have been carried out via Python.

3.1.1 OSIRIS

The *de facto* state-of-the-art PIC code is OSIRIS, a fully parallelized, fully implicit, fully relativistic and fully object-oriented code that has been used to perform large-scale simulations in fields as diverse as plasma wakefield acceleration, laser-plasma interaction, space physics and relativistic plasma astrophysics. Together with the typical PIC algorithm, OSIRIS is equipped with additional QED modules that account for effects such as photon emission via nonlinear Compton scattering and multiphoton Breit-Wheeler pair production.
In a nonlinear Compton scattering event a lepton emits a photon with a significant fraction of its energy when accelerating in a strong electromagnetic field. The superparticle radiation recoil is added to equation (1.10), and a new macro-photon is created.
In multiphoton Breit-Wheeler pair production a electron-positron pair is produced after a high-energy photon is absorbed by a high-energy density electromagnetic field while propagating in it. In this case the macro-photons are instead deleted from the simulation and a pair of two new superparticles is created in its stead.
Both implemented QED processes satisfy momentum, energy and charge conservation. The differential probability rates for these processes are evaluated by OSIRIS

via Monte Carlo methods in each simulation time step and for each superparticle.

Finally, in order to deal with the rapid growth of the number of superparticles due to the pair cascade processes, OSIRIS is implemented with a merging algorithm which combines multiple superparticles of the same species, conserving energy, momentum and charge locally, ensured by merging particles that are close in both configuration and momentum spaces. This very algorithm is applicable not only to massive (e.g. electrons, positrons, protons) but also to massless (e.g. photons) particles. This merge greatly optimizes and accelerates the simulations in which an accumulation of a large number of superparticles in a small region of space could otherwise lead to a load imbalance, hence making the simulation inaccessible.

3.1.2 NATA

Nata is a python package for post-processing and visualizing simulation output for particle-in-cell codes. It utilizes the numpy interface to provide a simple way to read, manipulate, and represent simulation output. I used it inside JupyterLab, an environment for interactive and reproducible computing based on the web-based Jupyter Notebook, which supports Python at its core.

The tool has proven essential not only to being able to visualize the simulation results, which format does not allow a simple Python script to be opened with, but also for the possible ways to compare different data files in parallel, which were not available by using the VisXD tool.

The results of the series of post-processing analysis can be appreciated in the following chapters: I will describe the thought process behind the simulation setup for each aspect of the cascade event to be investigated, together with some of the most significant plots produced to verify the analytical models.

3.2 Cascade onset

Considering that most of the analytical considerations are based on equations (2.27) and (2.29) governing the acceleration times for the leptons to reach the pair production threshold γ_{thr}, those are the very first equation to be verified. Following the layers characterization described in Section 2.3.3, I tried and evaluating the distinct phases of the cascade process onset.

3.2.1 Evaluation of τ_0

By looking at Figure 2.2, at time $t = 0$ the gap gradually opens due the electron drifting rightwards, generating a capacitor-like system that leads to the development of a linear electric field inside of the gap. The chosen setup consists in a uniform distribution of positrons, which are initially static due to the zero electric field, and

no electrons whatsoever. This decision aimed at simplifying the simulation while still satisfying the Goldreich-Julian density 1.2, which the positron density is set to be equal to, for the reason depicted in Section 2.3.1. Since the absence of electrons in this first stage simulation, the effect of the departing leptons is mimicked by superimposing an external electric field that grows according to equation (2.19) in the simulation setup itself.

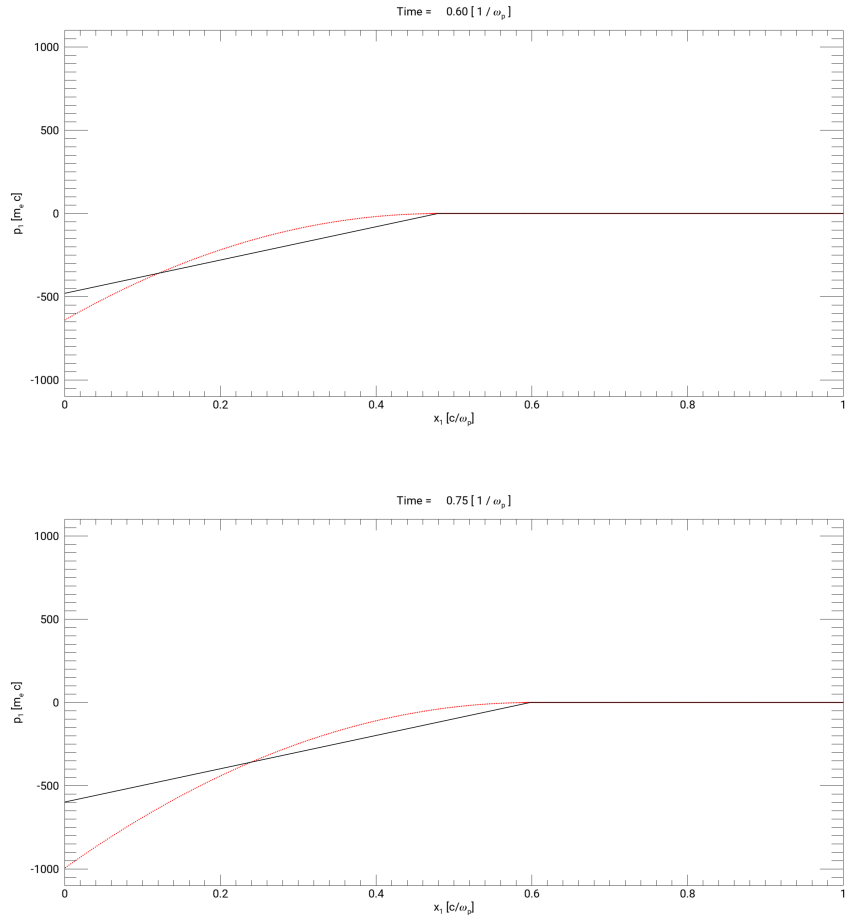

Figure 3.1: Top: positrons (red) phase space distribution at $t = 0.6[1/\omega_p]$
Bottom: positrons (red) phase space distribution at $t = 0.75[1/\omega_p]$
In both plots, obtained with $v_f = 0.79c$ and $f = 0.05$, the electric field (black) has been resized in order to visualize the gap opening while leptons are accelerating towards $\gamma_{\text{thr}} = 1000$. Diagrams obtained via VisXD.

By comparing the positrons phase space diagrams at different times in Figure 3.1, it can be observed how the leptons in the gap start being accelerated towards

the surface as soon as the gap front reaches their position. This preliminary set of simulations, which includes others performed with different v_f and $\gamma_{\rm thr}$, confirms the expected time τ_0 at which the first positron pair produces at the gap, in accordance with the analytical model described in Section 2.3.3.

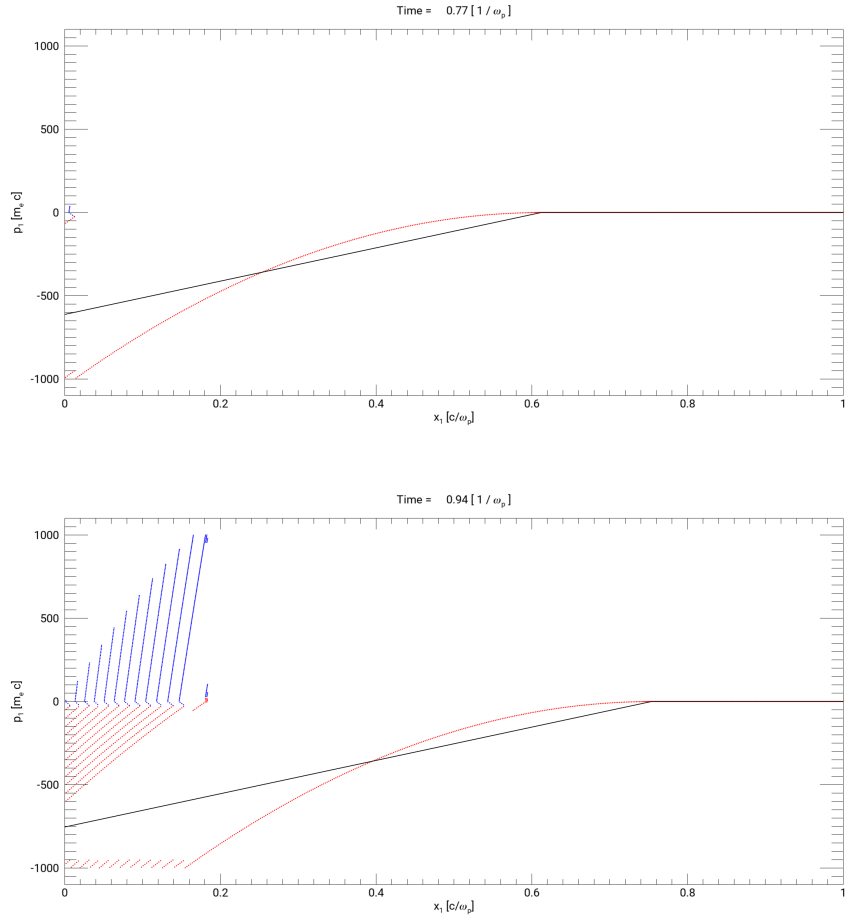

Figure 3.2: Top: positrons (red) and electrons (blue) phase space distribution at $t = 0.77\,[1/\omega_p]$ with $v_f = 0.79c$ and $f = 0.05$.
Bottom: positrons (red) and electrons (blue) phase space distribution at $t = 0.94\,[1/\omega_p]$ with $v_f = 0.79c$ and $f = 0.05$.
After the first progenitor reaches $\gamma_{\rm thr}$ for the first time at $t = \tau_0$, it undergoes pair production process (the same occurs for all the positrons behind it at later stages): in that events it loses a fraction f of its energy and produces an electron-positron pair with energy equal to $f/2 * \gamma_{\rm thr}$. The electrons produced this way will eventually reach the threshold themselves while drifting rightwards, pair producing and feeding the cascade process in their turn.

In this thesis, the QED pair production is assumed to be a threshold process, hence it takes place as soon as a lepton reaches the chosen threshold energy. At τ_0 the first proton reaches γ_{thr} on the stellar surface: there it loses a fraction f of its energy, which is equally distributed between the just pair-produced particles (each with energy $f/2 * \gamma_{\text{thr}}$). After this characteristic time, all the positrons behind the first progenitor, which are accelerated towards the surface by the electric field, undergo pair production in their turn at further and further distance from the surface itself. This can be appreciated in Figure 3.2 by observing the lower edge of the plot: in that region it's possible to find the so-defined "population 1" particles, which we defined in Section 2.2 as the ones having energies in the range between $\gamma_{\text{thr}} - \gamma_{\text{pair}} = (1 - f) * \gamma_{\text{thr}}$ and γ_{thr}. These particles continue being accelerated towards the threshold energy and pair produce every t_p until collapsing on the surface.

At the same time the electrons so-produced are accelerated in the opposite direction: after a time interval t_a they will eventually pair produce (as noticeable in the bottom plot of Figure 3.2), leading to other generations of progeny particles filling the gap.

3.2.2 Superimposing a linear electric field

The simplification induced by the absence of the initial electron population, hence the need of superimposing a linear electric field that grows according to the GJ parameters, is perfectly reasonable until QED processes occur: after pair production events initiate, positrons in population 1 start accumulating in the energy band close to γ_{thr} while new leptons are created and accelerate in opposite directions. Those particles start perturbing the electric field in a more significant manner the further we proceed in the cascade process, hence making the simulation non comparable with the analytical models. Since it is not possible to manually remove the self-consistent electric field from the OSIRIS code (contrary to what you can do with the QED processes, that can be switched on and off according to need), the solution adopted in these analysis is to reduce by different orders of magnitude the initial particle density, such that the E field they create is negligible if compared to the superimposed one.

This conjecture has been proven against different simulations, by changing both the setup density and the parameters governing the cascade process (f, γ_{thr} and, accordingly, v_f): in each run with $\rho_+ = \rho_{\text{GJ}}$ the self-consistent E field perfectly matched the theoretical one up until $t = \tau_0$, while in the low-density setups it has been proven that the particle-induced field is negligible with respect to the imposed one even after some generations of pair cascade progeny, whose multiplicity could've eventually led to some perturbation.

3.3 Single electron setup

With the fundamental equation of the analytical models being proved against PIC simulations, I then aimed at investigating the behavior of such electron-positron plasma in forced linearly-growing electric fields.

One of the crucial aspect for this kind of cascading phenomena in pulsars is the capability of filling with fresh plasma the gap generating in the polar caps: this is possible only under the condition of a sufficiently high multiplicity $\mathcal{M}$ (1.5), which can be achieved if the growth rate of the leptons population is sufficiently high. It is worth underlining that the low-density reduced model is still necessary to ensure that the electric field keeps developing linearly, not perturbed by the particle-generated one, as justified before.

Hereafter, the thought processes and the simulation choices aimed at investigating $\Gamma(t)$ will be presented. The focus of this analysis will be specifically the growth of the electrons population: this choice is purely out of convenience since, as electrons move together with their progenitors of the same specie unlike positrons, it is easier to count the firsts in the post-processing phase.

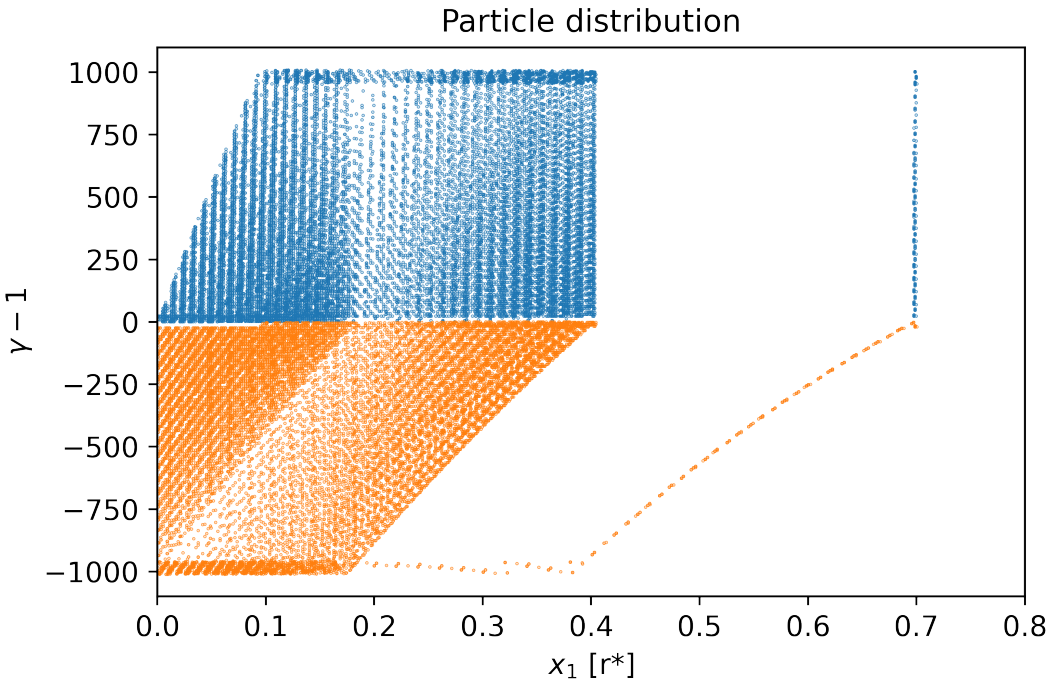

Figure 3.3: Electrons (blue) and positrons (orange) phase space distribution at $t = 0.7\,[r^*/c]$, starting from a single still electron in $x = 0$; $\gamma_{\text{thr}} = 1000$, f=0.05.

3.3.1 Total electrons evolution

Following the considerations made in Section 2.3.3 we can assume that, right after $t = \tau_0$, an electron generated at the surface (which we assume having initial $\gamma = 1$) starts being accelerated by the gap field while moving rightwards at c, leading to pair cascade once reaching γ_{thr}. This cascade process ends when the observed layer reaches the gap front since the E field vanishes there, hence the particles are not accelerated anymore. Another condition under which the whole process concludes is when $t_a(t)$ is no longer defined, which occurs when the E field is too low for the particles to be accelerated to γ_{thr}, marking a t_{end} (2.33) for the analysis.

By taking a close look at Figure 3.3, one could easily notice the difference between population "1" (gathering close to $\pm\gamma_{\text{thr}}$) and population "2" leptons we mentioned before. However, the most noticeable behavior in the distribution is the the separation between different groups of leptons depending on their spacial position; these correspond to many generations of particles and their progeny of the same kind.

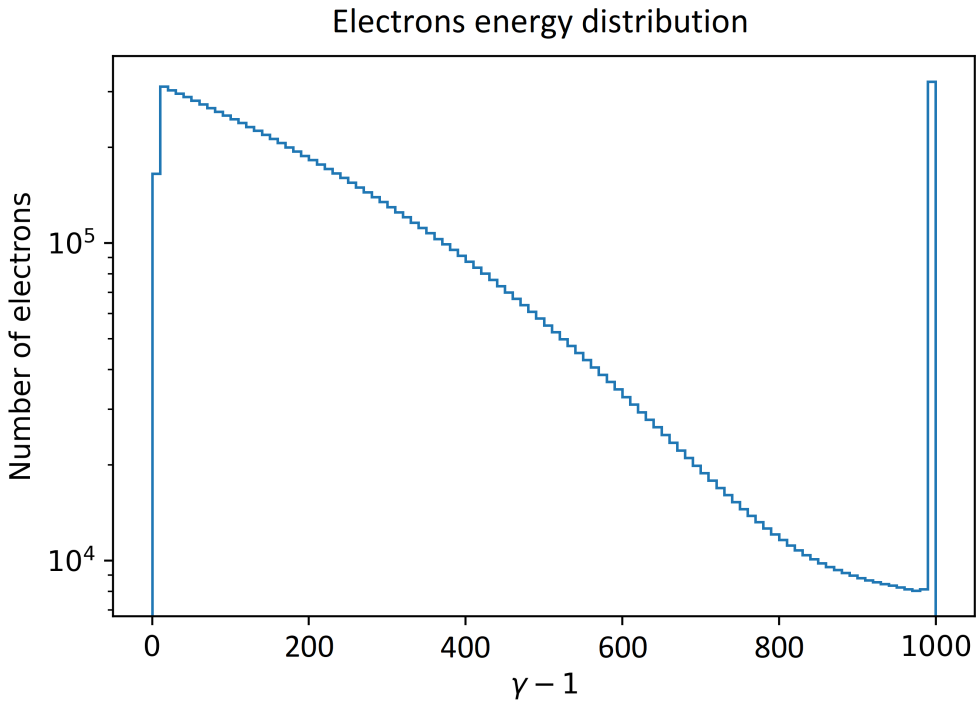

Figure 3.4: Unnormalized electrons distribution based on their energy throughout the whole system at $t = 0.7\,[r^*/c]$. The peak between $\gamma = 980$ and $\gamma = 1000 = \gamma_{\text{thr}}$ corresponds to "population 1" electrons, while all the others are "population 2" ones.

1) at $x = 0.7[r^*/c]$ the thin layer gathers the initial electron of the setup and all its electron progeny, which move together at c rightwards while pair producing.
2) between $x = 0.4[r^*/c]$ and $x = 0.7[r^*/c]$ there are the positrons recently produced by the previous group; their distribution seems "tilted" since they drift towards the surface, away from their source, while accelerating to high energies.
3) between $x = 0.18[r^*/c]$ and $x = 0.4[r^*/c]$ a new generation of electrons shows up, deriving from the previous positron reaching γ_{thr} and pair producing; their positron counterpart extends up to the surface for the reason given above, but the "slope" is noticeably steeper due to the stronger electric field the particles face here.
4) finally, the denser group before $x = 0.18[r^*/c]$ includes the particles generated by the positrons ahead; electrons here do not extend up to the surface since they need at least a time $t = t_a$ to reach the threshold despite it being even lower here due to the higher E field.

Figure 3.4 shows the number of electrons in the discretized energy space (intervals of $\gamma = 10$): "population 2" has a decreasing number of particles with the energy, followed by a sharp peak between $\gamma = 980 = \gamma_{\text{thr}} - \gamma_{\text{pair}} = (1 - f)\gamma_{\text{thr}}$ and $\gamma = 1000 = \gamma_{\text{thr}}$ corresponding to "population 1" electrons. This distinction strongly depends on the f parameter: since particles lose a fraction f of their energy in the pair production process, the lower the value of f, the faster they are re-accelerated to γ_{thr} according to the concept of the characteristic time t_p (2.29).

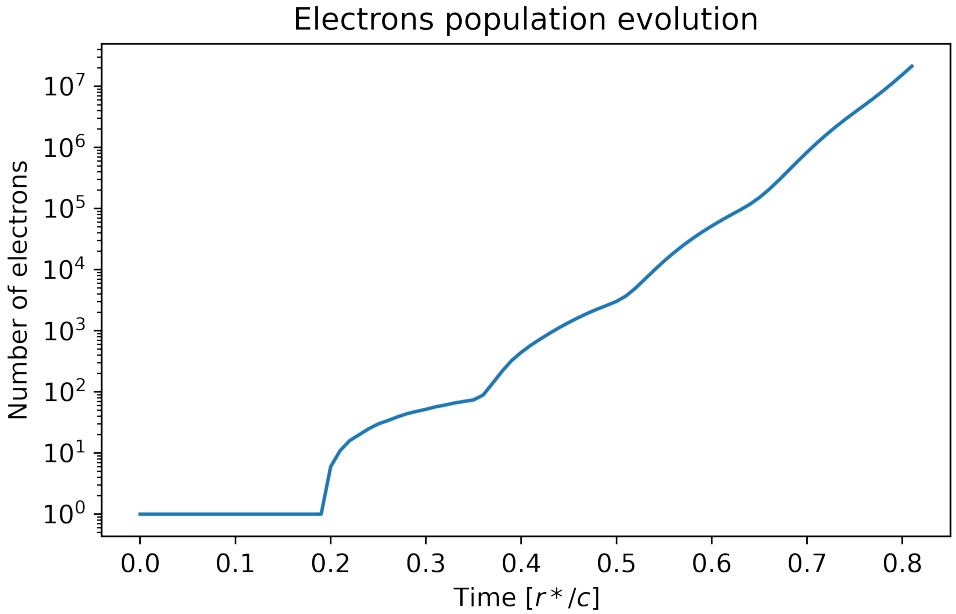

Figure 3.5: Evolution of the number of electrons in the system. Results are shown on a logarithmic scale since we are investigating an exponential growth

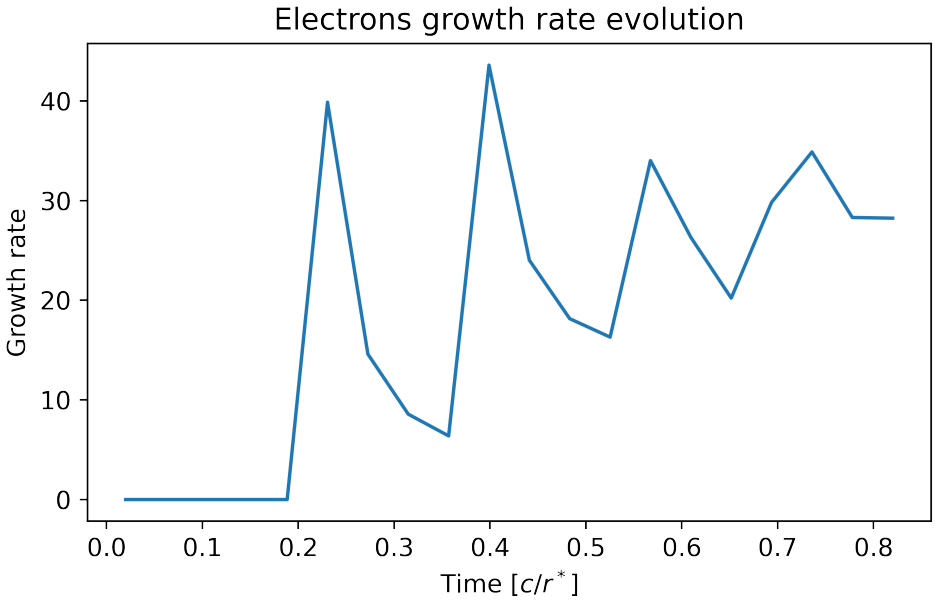

Figure 3.6: Growth rate evolution corresponding to the particles evolution shown in Figure 3.5. The exponent $\Gamma(t)$ is clearly time-dependent, especially in the early stages of the growth, because of the linearly-increasing electric field and the new generations of pair producing leptons every t_a

The global growth of the electrons in the system can be appreciated in Figure 3.5, in which their number is plotted on a log scale as a function of time. The first part of the graph is flat and corresponds to the initial time $t_a \simeq 0.19\,[r^*/c]$ (2.27) needed for the single electron of the setup to be accelerated to γ_{thr} and pair-produce. The increase in the number of electrons represented by the first "bulge" after t_a is related to the progeny of the original lepton and is basically linear: that's because the single electron that is pair producing does so every t_p, which is weakly depending on time due to the slow increase of the electric field (it can be considered constant locally). The plot then presents other bumps roughly every t_a due to new generations of leptons reaching the threshold, making the growth roughly exponential.

This exponential growth $\Gamma(t)$, whose evolution is displayed in Figure 3.6, presents a time-dependent exponent due to the field growing linearly in time, as analyzed in Section 2.5. Despite the bulges are less evident with the passing of different generations, leading to less varying growth rates, the average Γ value is slightly increasing over time. The time necessary for a particle to undergo a pair-production event $t_p(t)$ becomes smaller and smaller the longer the simulation, since it decreases with the electric field becoming stronger with time, hence leading to more and more frequent pair-production events.

3.3.2 Inhibited pair production by positrons

While observing the evolution of all the electrons produced by the system it is not possible to confirm the theoretical conditions under which the cascade process should conclude. In fact, even if the setup-electron reaches the gap front, hence stop being accelerated due to the E field vanishing there, electrons that were generated by positron continue pair producing closer to the surface. In order to verify the analytical model, I chose to inhibit pair production by positrons by directly modifying the OSIRIS code. This has later been proven to give the same results as by only taking into account the electrons in the very first layer.

Out of coherence with the previous model, the gap has been set to be already open at the beginning of this setup, since no acceleration would be induced on the first electron if it immediately overtook the gap front at the simulation onset. The starting magnitude and dimensions of the electric field have been calculated according to the analytical models (2.19) with the chosen values of v_f and f and with initial time τ_0.

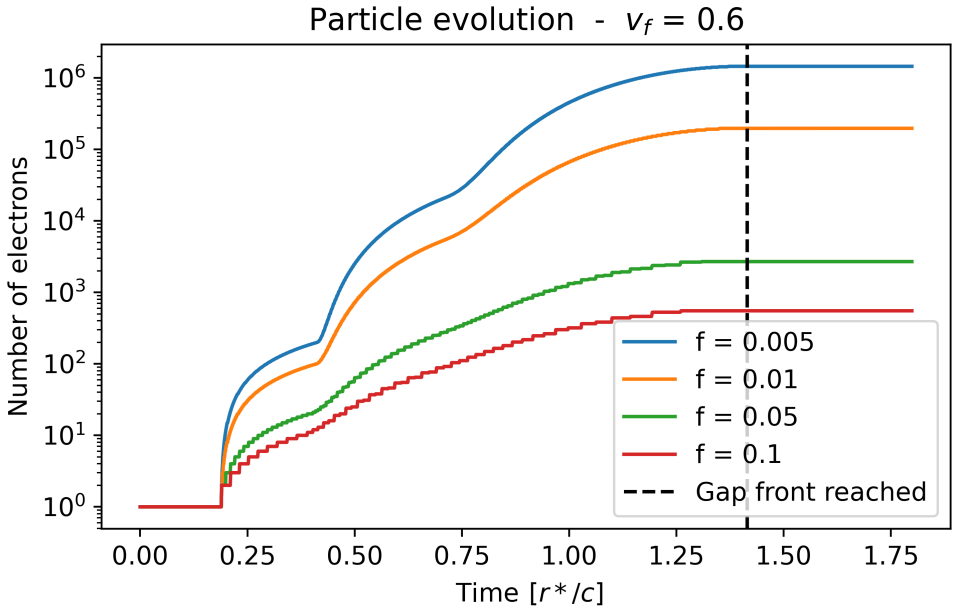

Figure 3.7: Comparison of the number of electrons for different f and $v_f = 0.6$

Figure 3.7 shows the evolution in time of the number of electrons in the system for different values of the parameter f. Let us compare this results with the previous evaluation in which all the electrons were taken into account, including the ones produced by positrons, displayed in Figure 3.5.

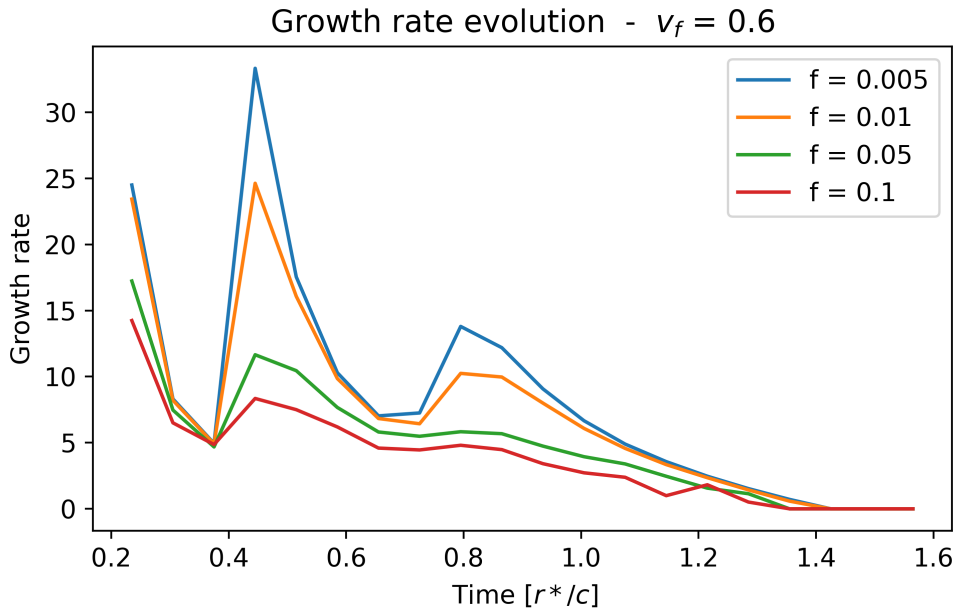

Figure 3.8: Comparison in the evolution of the growth rates corresponding to the different values of f and $v_f = 0.6$

Aside from the particle count at a given time, which is predictably lower in the current case since I deliberately inhibited protons from pair producing, what is also varying is the behavior of the growth rate (Figure 3.8): while in the previous scenario it was observed to oscillate around a value slightly increasing over time, here it progressively reduces until vanishing completely at a specific moment, independently on the value of f chosen.

The time at which the growth rate goes to zero is the one at which the first layer of electrons (and the only one since no positrons drifting behind can pair produce) reaches the gap front, which is moving only at a fraction of c. In that specific moment, the E field vanishes and electrons stop being accelerated by it. In a first approximation, this front-reaching time can be evaluated as:

$$t_{\text{end}} = \frac{\tau_0 v_f}{c - v_f} = \frac{\tau_0 \overline{v_f}}{1 - \overline{v_f}} \tag{3.1}$$

since the gap front is initially at a distance $\tau_0 v_f$ from the surface and the relative velocity between electrons and the front is $c - v_f$ ($1 - \overline{v_f}$ in normalized units). This approximation has been proven to match the simulation results for all the combinations of f and v_f that have been tested. Theoretically more accurate values for t_{end} are given by equation (2.33), which has been proven to lead to the same results since it mildly depends on f while mainly depending on v_f.

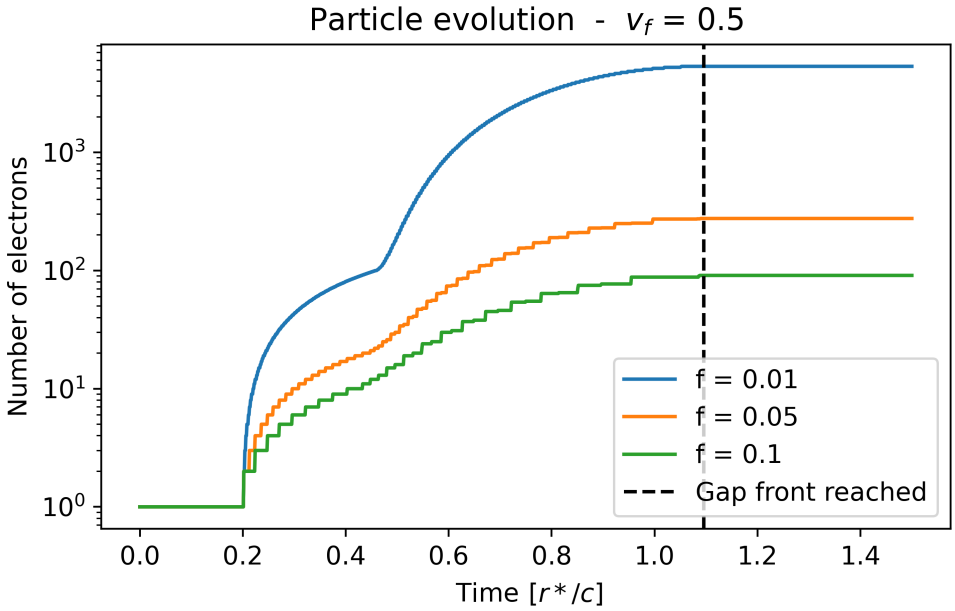

Figure 3.9: Comparison of the number of electrons for different f and $v_f = 0.5$

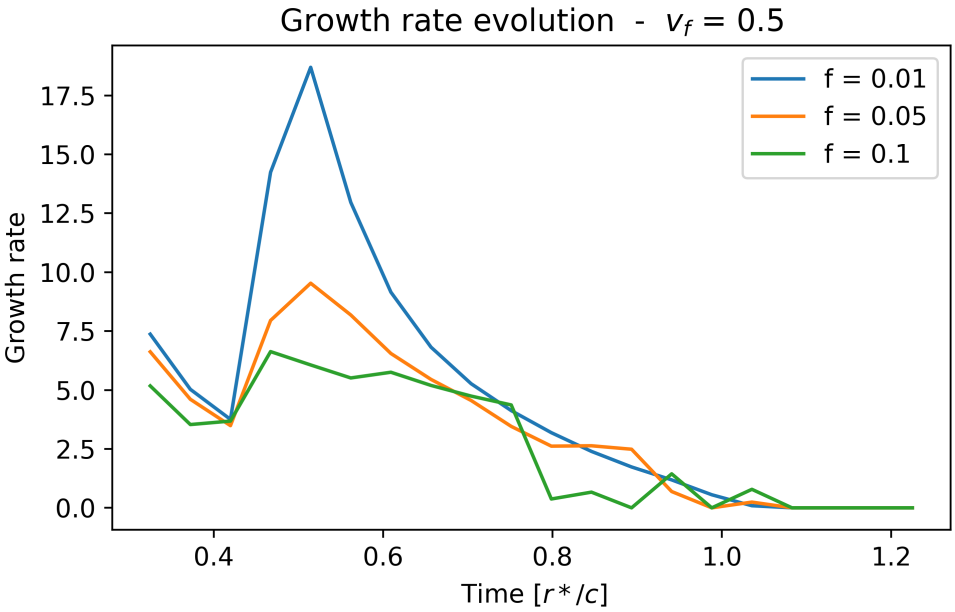

Figure 3.10: Growth rates comparison for different values of f and $v_f = 0.5$

This kind of simulations are usually suit for parametric analysis, for which the electrons population evolution for different values of a particular parameter is investigated and the results compared. Aside from the magnitude of the externally imposed E field, which evolves as the one developed by a uniform positron distribution of density ρ_{GJ}, the only other parameters on which the phenomena depends are f and v_f.

Figure 3.7 directly shows the comparison in the population growth on a logarithmic scale for different possible values of f while fixing $v_f = 0.6$. First of all, the different simulations share the same t_{end} since they have the v_f in common. They also share similar t_a, the characteristic acceleration times needed for freshly pair-produced leptons to reach γ_{thr}, since those mainly depend on the threshold energy itself and the E field imposed, while mildly depending on f - see equation (2.27) - which only affects the particles low initial energy. This acceleration time $t_a(t)$ is the one regulating the alternation of the different "bumps" in the plots: the first one is basically a line (which become logarithmic in this scale), whose slope is $1/t_p$ since the only electron which is pair producing does so every t_p (which is locally time-independent since it perceives a E field almost constant). Then, when the first-generation electrons reach the threshold hence start undergoing pair production, the population has another burst in its rate of growth. The t_a for the second generation particles, roughly corresponding to the second bump width, is slightly higher than the first one: that can be explained by the fact that electrons, while drifting towards the gap front, experience an electric field which is increasingly lower, hence the time needed for them to be accelerated to γ_{thr} is increasingly higher.

The distinction between the bumps in the plots is more evident the lower the f, since for those values t_p is very low, particles are pair-produced more often, hence multiplicity is higher and more easily observable in the population evolution. This behavior is confirmed by the growth rate evolution (Figure 3.8), which present sharp peaks for in correspondence of the different $t_a(t)$ for $f = 0.005$ while being quite smooth for $f = 0.1$.

A similar behavior can be observed in the comparisons of the simulations performed with $v_f = 0.5$, which can be observed in Figure 3.9 and Figure 3.10. In this setup, as well as in the previous one, the growth rate tends to be smoother for higher values of f. What can also be noticed is that the plots for the electrons number are step-wise, since particles are produced once at a time; this behavior is much more evident for for higher values of f since, for those, $t_p(t)$ is higher, hence the steps larger. Those steps being increasingly larger also confirms the time dependency for this characteristic time, since it takes longer and longer to be re-accelerated to γ_{thr} the closer a particles is to the gap front, according to equation (2.29). While τ_0 is slightly higher for $v_f = 0.5$ with respect to $v_f = 0.6$ due to the lower E field, the t_{end} is lower as expected, all according to the analytical models.

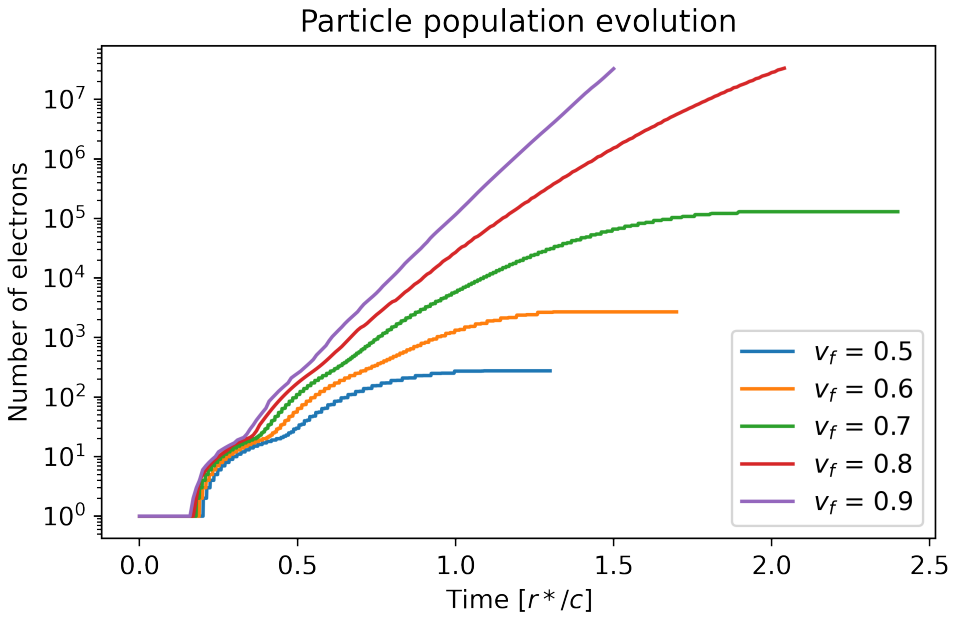

Figure 3.11: Comparison of the number of electrons for $f = 0.05$ and different v_f

A broader comparison between different gap front velocities can be appreciated in the result of parametric analysis in Figure 3.11 for the leptons population and in Figure 3.12 for its corresponding growth rate. Here the difference in the front catching for different values of v_f becomes explicit, together with the behavior for the slope of the curve described previously. After an initial phase in which the setup electron is the only pair-producing particle, the curves spread significantly due to the strong difference in the electric fields experienced by the leptons.

The most extreme case investigated in this evaluation is the setup with $v_f = 0.9$: for that value of the gap front velocity the population evolution plot presents only one evident "bump", followed by a curve which is almost straight in the log plot, hence basically a pure exponential. The idea that $\Gamma(t)$ is almost independent from time after the initial phase is confirmed by its plot in Figure 3.12, which converges to some fixed value around 12 (in normalized 1/time units) in a very short time - basically right after the second-generation particles start pair producing. That setup leads to results very similar to the ones one would obtain by simulating particles in a constant electric field: since the electrons drift rightwards slightly faster than the gap front, the variation in the E field magnitude they are immersed in is very slow, hence leading to characteristic times t_a and t_p which are almost constant in time. This limit behavior - which becomes fully-fledged for $v_f = 1$ - is only valid for electrons, since those are the leptons drifting towards the gap front.

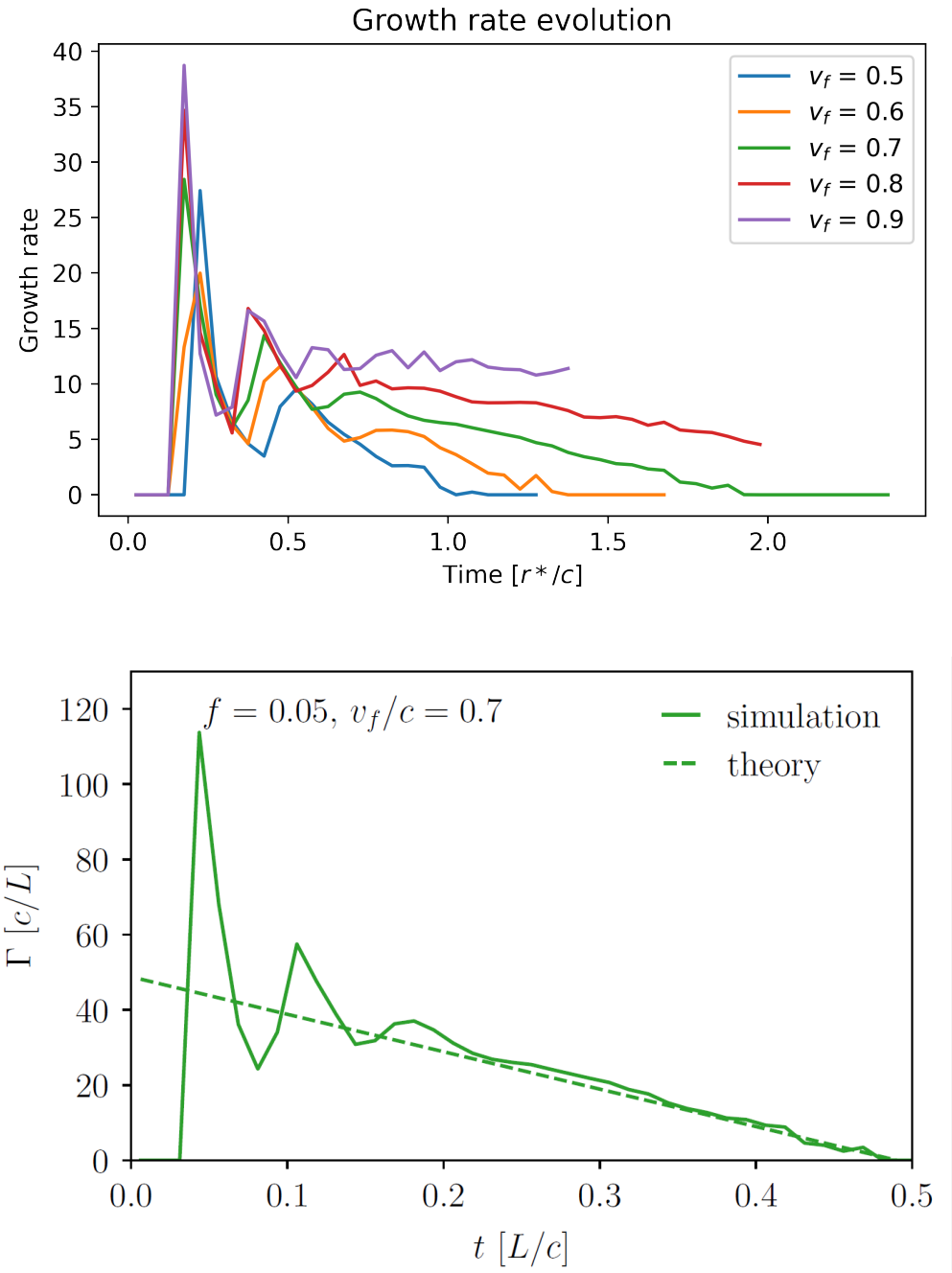

Figure 3.12: Top: Comparison of the growth rates corresponding to the curves of Figure 3.11 for $f = 0.05$ and different values of v_f.
Bottom: Comparison between the growth rate corresponding to the curve obtained with $f = 0.05$ and $v_f = 0.7$ and the theoretical growth rate according to the analytical models. Axes in this plot are referred to the length of the PIC simulation domain L instead of the usual r^*.

The situation would be reversed if we accounted the positrons as well, which would instead experience a stronger increase in the field magnitude the higher the v_f. Furthermore, this behavior is locally valid when following a certain layer of electrons, but is surely not a good approximation when studying the distribution of particles in their phase space, for which the field they experience may change dramatically depending on their distance from the surface and the gap front. The slower change in the growth rate for higher values of v_f is also reflected by the inherently longer time needed to reach the gap front - where $\Gamma(t) = 0$ - hence by the smaller slope in the growth rate versus time. In this set of simulations the gap front couldn't even be reached before getting to $\simeq 4 \cdot 10^7$ particles in the system, which marks the threshold after which the simulation becomes too slow to be sustained.

While considering the growth rate constant is an acceptable approximation for $v_f \gtrsim 0.9$, time dependency of $\Gamma(t)$ is definitely non-negligible for lower values of the gap front velocity. The bottom plot in Figure 3.12 shows the same green curve present in the top plot, resulting from a simulation with $f = 0.05$ and $v_f = 0.7$, overlaid by the theoretical growth rate evaluated analytically. In that diagram the axes show different values with respect to the ones above since the spacial units are expressed by means of the length of the PIC simulation domain L instead of the usual pulsar radius r^*: the choice reflected the need of comparing the numerical results with the analytical ones, which were expressed in c/L units for convenience. The theoretical line has been plotted using the corrected equation for $\Gamma(t)$:

$$\Gamma(t)t_a(t) = \frac{1}{1+\psi(t)} W\left(\frac{1+\psi(t)}{f}\right) \tag{3.2}$$

and using the first order approximation for ψ find in equation (2.44). Before $t \simeq 1 - 2t_a \simeq 0.2\,[L/c]$, the growth rate presents some really pronounced peaks, sign that the particle growth is not yet purely exponential and, thus, falls out of the regime of validity of the models. The time from which the model can be considered valid and not only a rough approximation roughly corresponds to the end of the second bump in particles count of Figure 3.11. After that the model has proven to fit the simulation results with exceptional accuracy, as depicted in Figure 3.12.

When choosing higher values of the t_p/t_a ratio, like in Figure 3.13 where $f = 0.1$ has been chosen, it is possible to appreciate the t_{end} for higher values of v_f since the whole population grows more slowly: this is well explained by the theory since $\Gamma(t)$ evolves approximately as $W(1/f)/t_a(t)$ (2.43). This not only helps in distinguishing the differences in magnitude and time scales at which these phenomena occur according to the setup conditions chosen, but also in starting having an idea of what values of the parameters lead to the actual condition in the real environment of the pulsar.

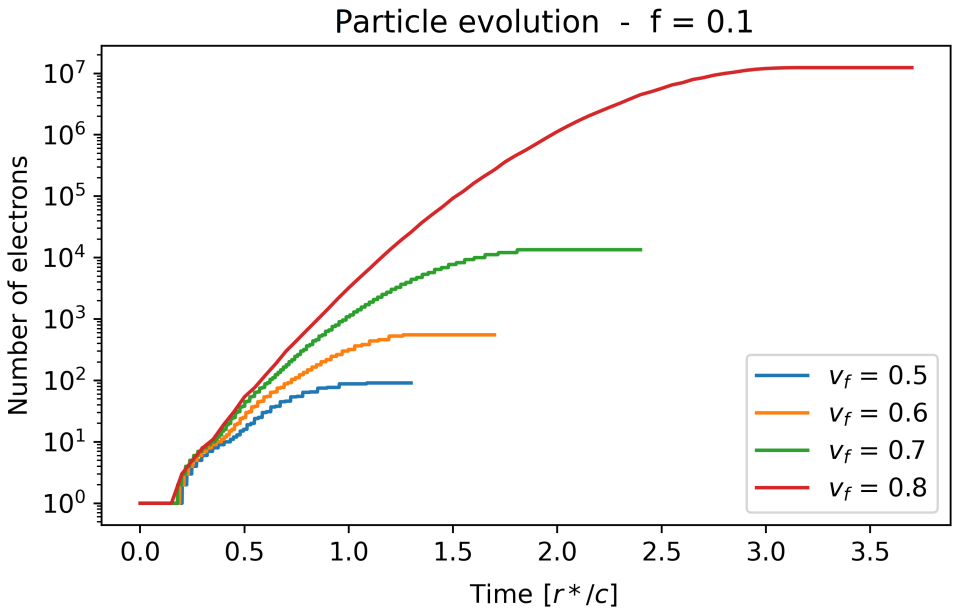

Figure 3.13: Comparison of the number of electrons for $f = 0.1$ and different v_f

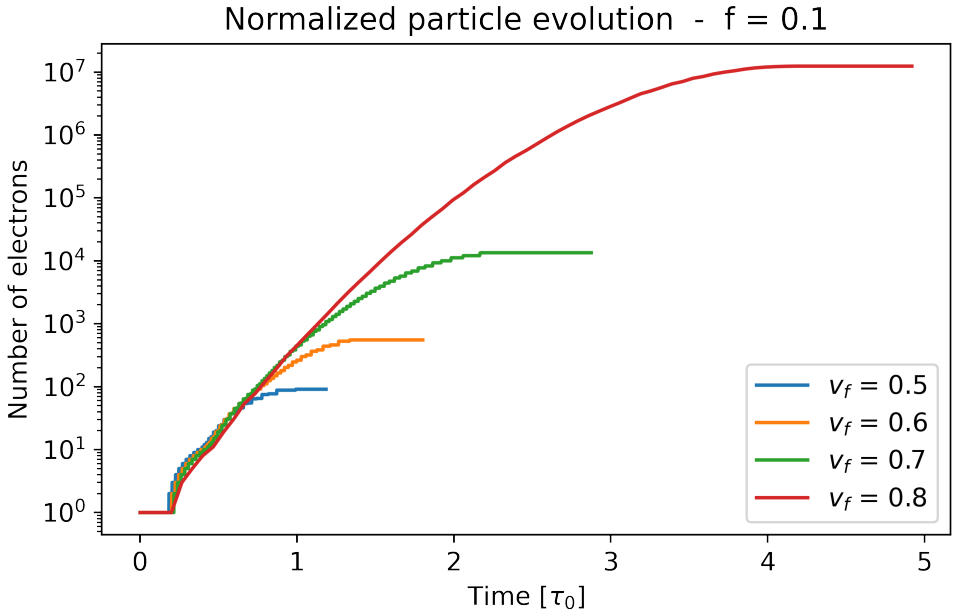

Figure 3.14: Comparison of the number of electrons for $f = 0.1$ and different v_f, time units normalized to the characteristic time $\tau_0(v_f)$

The very same results shown in Figure 3.13 are also proposed in Figure 3.14 with a slightly different time scale. While in the first image the time frame is r^*/c and is the same for each simulation, in the second one it varies for each value of v_f because it is normalized in terms of the characteristic time τ_0 - the time at which the progenitor electron would be generated at the surface by a uniform distribution of positrons, hence the starting point of these sets of simulations. This choice comes from the search for an alternative in showing the simulation results such that one could be able to compare the influence of the gap propagation velocities on the population growth while taking into consideration the initial acceleration time $t_a(\tau_0)$ needed to start the cascade process. Among the alternatives tried, by means of different time delays and/or contractions, the simple re-scaling in τ_0 time units turned out to be the most effective for a series of reasons.

Firstly, thanks to this choice in normalization, the timestamps at which the progenitor electrons undergo pair production for the first time is the same for every v_f, while normally it has been observed how τ_0 decreases with v_f, since since higher velocities imply stronger E fields hence greater accelerations on particles. Furthermore, in the normalized plot one could also grasp the common behavior between the population corresponding to different velocities in the early stages of the cascade process: all the curves start ramping up from the same normalized t_a^* and present very similar growth rates before entering the final stage of the cascade when the field has become too weak to accelerate the electrons effectively anymore.

Despite being a simplified investigation with respect to the full QED, self-consistent, enhanced positron case, this preliminary electrons analysis paved the way for the ones in the following sections by confirming some fundamental analytical model and by showing, ideally, what data analysis approach would best fit out evaluations.

3.3.3 Allowed pair production by positrons

Since the overarching aim of this Thesis is to prove the analytical models described in Chapter 2 via PIC simulations, the oversimplification consisting in ignoring the pair production events of positrons is, for obvious reason, non-extendable anymore. By directly changing the code, the QED phenomena have been then made available again for all the leptons.

By looking at Figure 3.15 one could observe a distribution of particles in the phase space which is very similar to the one observed at the beginning of Section 3.3, which is in perfect accordance with the explanations given in Section 3.3.1. Following the strategy adopted in the previous case, parametric analysis have been conducted in order to compare the plots for fixed values of f and different gap front velocities v_f: the most significant result are shown in Figure 3.16, with the corresponding population growth rates $\Gamma(t)$ shown in Figure 3.17.

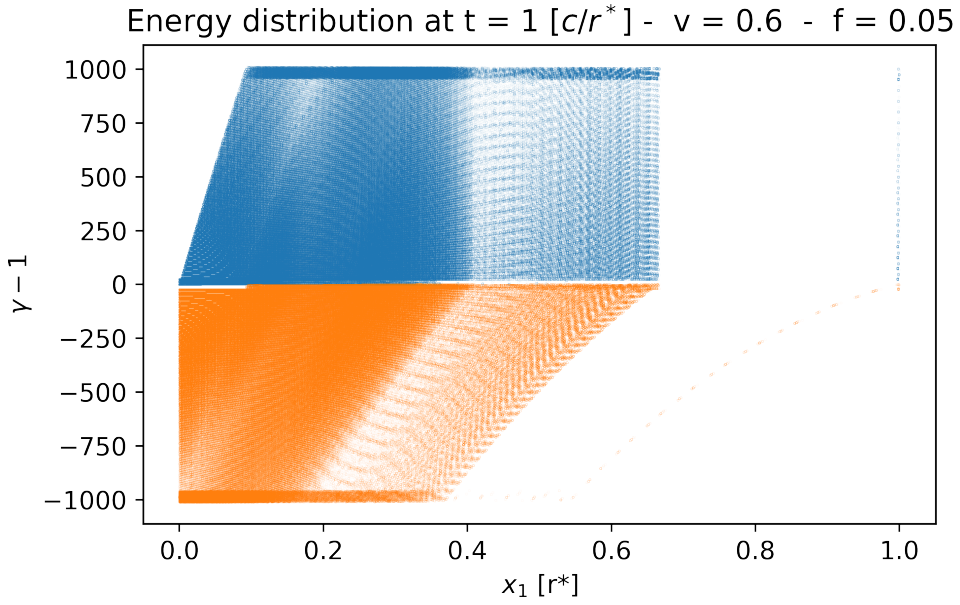

Figure 3.15: Electrons and positrons phase space distribution at $t = 1\,[r^*/c]$, starting from a single still electron in $x = 0$; $\gamma_{\text{thr}} = 1000$, f=0.05, v_f=0.6

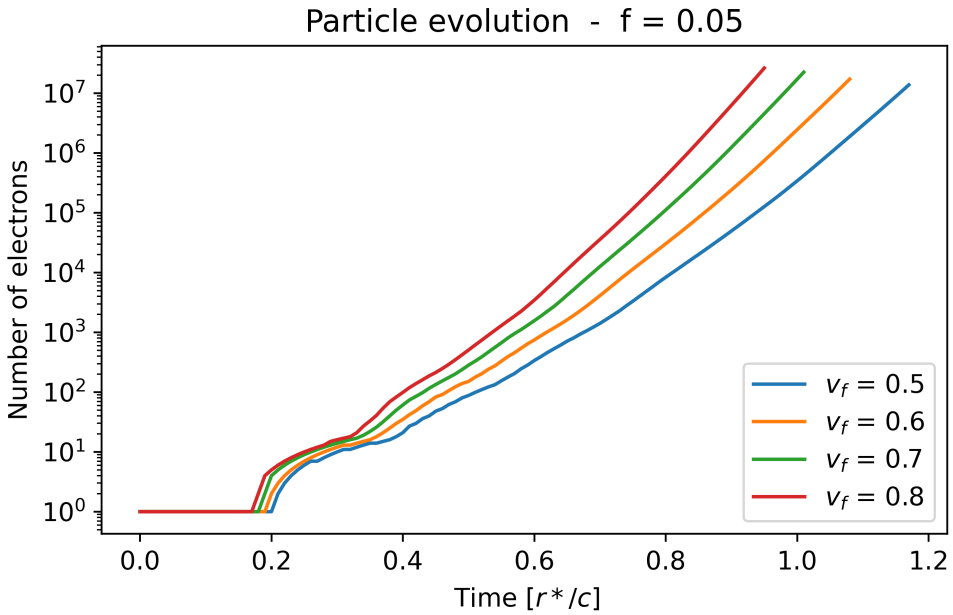

Figure 3.16: Comparison of the number of all the electrons in the system for f=0.05 and different v_f, with all leptons able to pair produce.

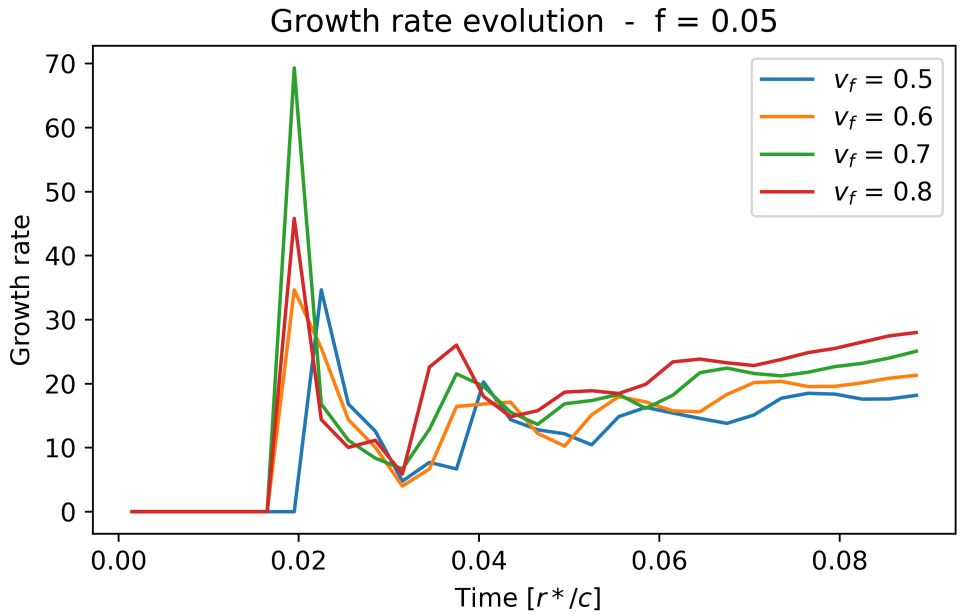

Figure 3.17: Corresponding growth rate comparison for f=0.05 and different v_f, with all leptons able to pair produce.

Just by taking a quick look at the particle evolution plot one could observe that, independently on the v_f, after the first bump the population ramps up with increasingly higher slope, contrary to the behavior observed in the previous case in which only electrons were able to pair produce. This can be also noticed by looking at the plot of the growth rate, which seems to oscillate around a positive-slope line, opposite to the gradual decreasing observed earlier in Figure 3.12. In the previous case the electrons population was limited to the progenitor layer, immersed in a electric field that gradually vanished, which explained the progressive reduction of growth rate until it became null when particles reached the gap front.

The presence of positrons, which have been totally neglected before, plays a crucial role in this framework since those can now undergo the same QED processes as electrons. It is worth underlining how pair production by positrons occurs at earlier and earlier positions with respect to the gap front since they accelerate towards the surface: thanks to this drifting, the electric field they face is then greater and greater, since it has a linear behavior in space - due to the capacitor effect it increases with the proximity to the surface while vanishing at the gap front - but also because it increases linearly in time. These combined effects make positrons accelerating to $\gamma_{\rm thr}$ more and more frequently, with increasingly lower characteristic times $t_a(t)$ and $t_p(t)$, hence leading to a steeper and steeper growth rate in the particles production.

This mainly affects the simulation process by shortening, by a factor of $\simeq 3$, the time at which the code stop compiling after reaching the maximum allowable number of particles in the system. This comparison with the previous setup is only valid for some combinations of high v_f and low f, for which the simulation didn't last long enough for the first layer to reach the gap front.

Another striking difference with the inhibited-positron case is the close similarity of the plots corresponding to different values of v_f, both in the number of particles and in their growth rates, which instead used to be noticeable more spread in the other setup. This behavior is due to the first layer electrons having less impact on the global population growth after the first bump: leptons that are produced behind quickly overcome the growth rate of the firsts since they experience a much higher electric field and since, at least for protons, they are not affected by its attenuation in time. The global behavior is then dominated by the bulk plasma, which undergoes the same processes independently on the v_f, just with a sort of time shifting: this is explicit in Figure 3.17 between 0.06 and 0.08 $[r^*/c]$, where the growth rates for different v_f share the very same evolution except for a slight attenuation and time delay.

Hereafter the plots for particle population and for the corresponding growth rate are shown with the time normalization to τ_0 applied.

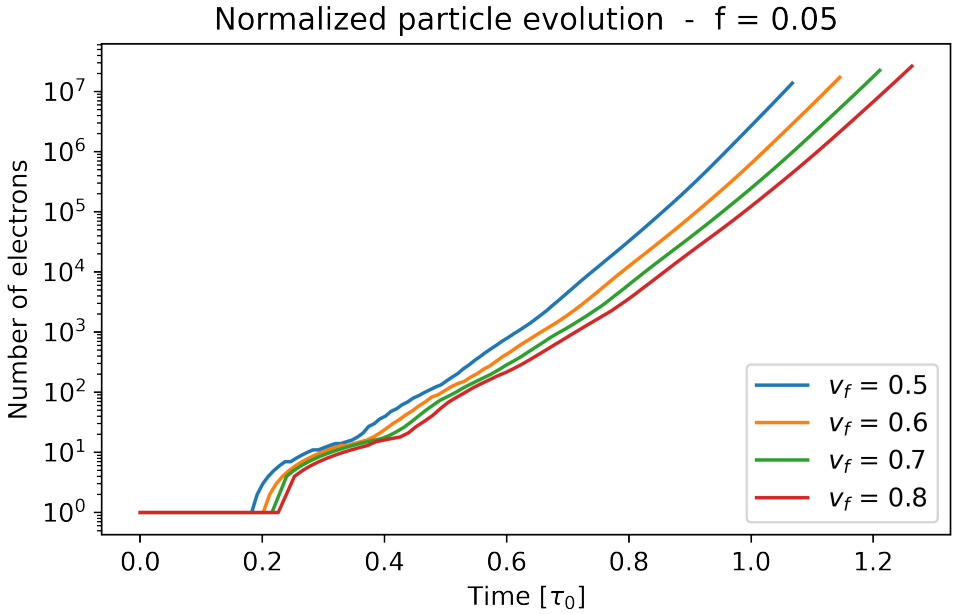

Figure 3.18: Particles population comparison for $f = 0.05$ and different v_f in normalized time scale, with all leptons able to pair produce.

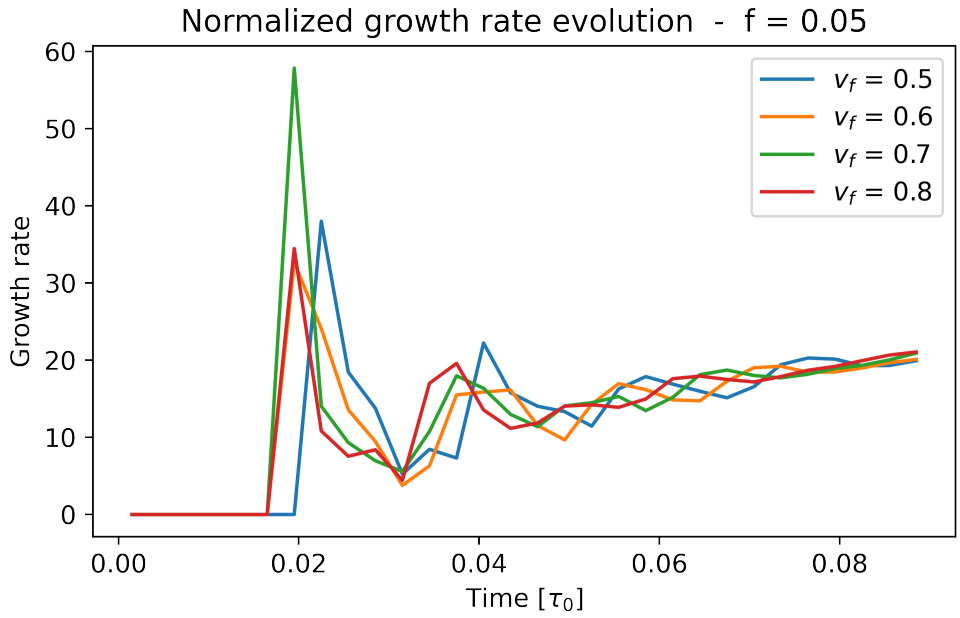

Figure 3.19: Corresponding growth rate comparison for f=0.05 and different v_f in normalized time scale, with all leptons able to pair produce.

When adopting this time normalization described in the previous section, the behaviour between different values of v_f becomes even more similar. The plots of the normalized particle evolution in Figure 3.18 are even more packed than the ones in Figure 3.16; while analyzing the corresponding growth rates in Figure 3.19 the superposition between the plots its even stronger: the peaks match quite well in time, and all the curves converge to the same line, all according to the analytical models described in Section 2.5.

As for the other setup, I wanted to perform another parametric analysis in order to compare the results for different values of f by fixing v_f. Amongst the different gap velocities tried for this kind of analysis, $v_f = 0.6$ proved to be the most interesting by being not too low to be physically unlikely but also not too high such as the simulation could last longer, hence further details could be appreciated. The results of this investigation are shown in Figure 3.20 for the particle evolution, while the corresponding plots for the growth rate are shown in Figure 3.21. This time the chosen values for f have been varied between $f = 0.1$ - which is the maximum after which it would make no physical sense - and $f = 0.001$, which is usually too little if one is seeking for long simulations but here it proved to be fine thanks to the chosen v_f. As expected, the smaller the f, the faster the particle growth and the more pronounced the bulges, as already deepened in Section 3.3.2.

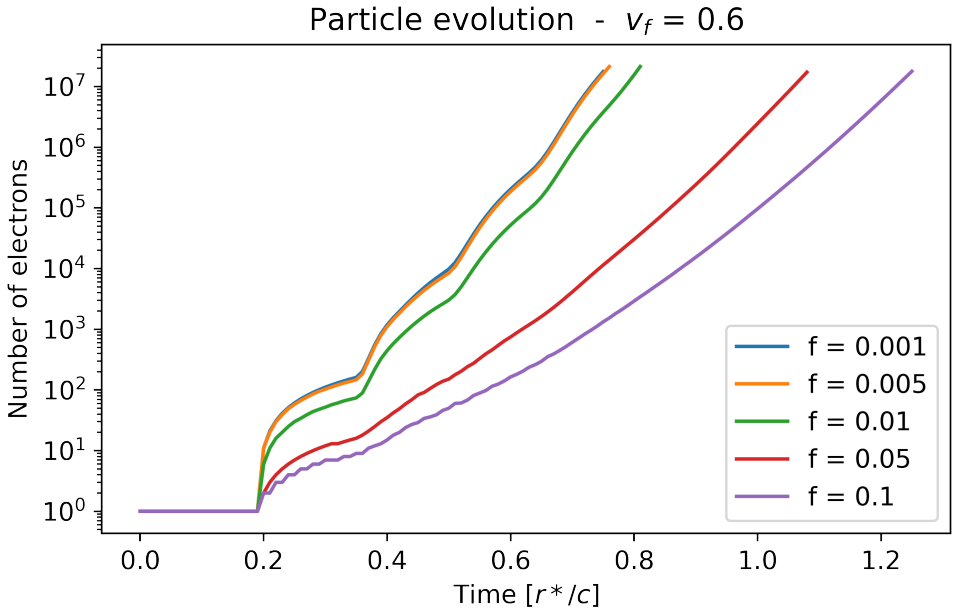

Figure 3.20: Comparison of the number of all the electrons in the system for different f and $v_f = 0.6$, with all leptons able to pair produce.

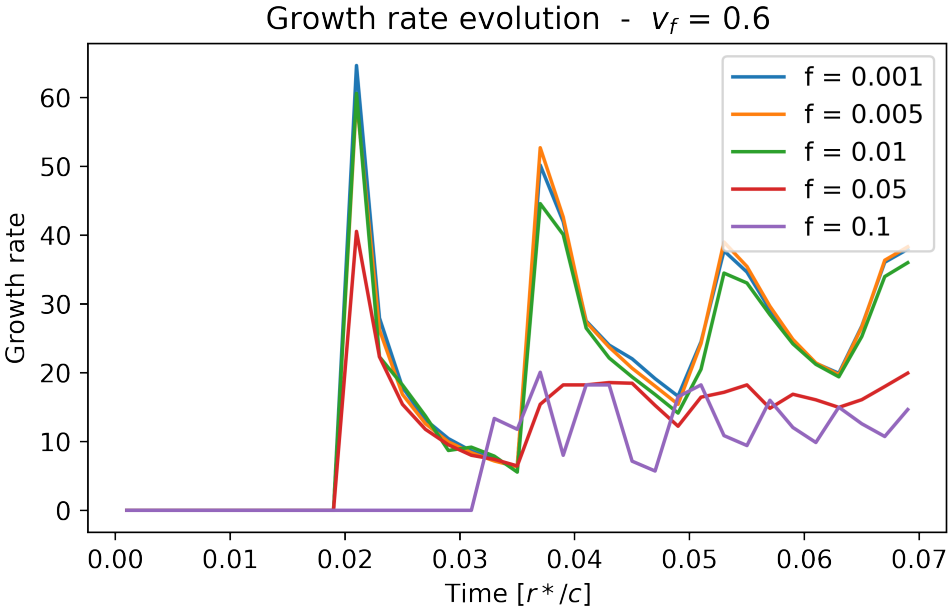

Figure 3.21: Corresponding growth rate comparison for f=0.05 and different v_f

Thanks to this extension in the parametric analysis, it can be observed how the plots tend to converge to a limit behavior. This not only makes perfect physical sense according to the theory, but it also allows us to make a few important assumptions: firstly, it has been proven how it is basically worthless performing simulations with $f < 0.005$, since they wouldn't provide additional information while being computationally heavier. Secondly, it could be acceptable, under the right circumstances, performing the approximation $f \ll 1 \rightarrow f \simeq 0$, since the particle evolution has a limit behavior corresponding to $f = 0$.

By looking at the growth rates of the different simulations, it is clear how its development is basically the same for small values of f, like if $f \leq 0.01$ in this very case where $v_f = 0.6$. The plot corresponding to $f = 0.05$ follows well the ones for smaller values of f in the first bulge, while also presenting the same alternations in time in the following ones: the only defect stands in the values of the peaks, which are significantly lower in that case. Finally, the plot corresponding to $f = 0.1$ definitely fails in representing the growth rate evolution: this is both due to the bulges being almost assents - for the very same reasons given in Section 3.3.2 - and both because the particle plot was originally not smooth enough unlike for the other values of f, leading to higher noise in evaluating the actual slope of the curves hence the growth rate. This results lead to the further consideration, complementary to the previous one for the low values of f, that one should exclude $f \geq 0.1$ with this simulation setups.

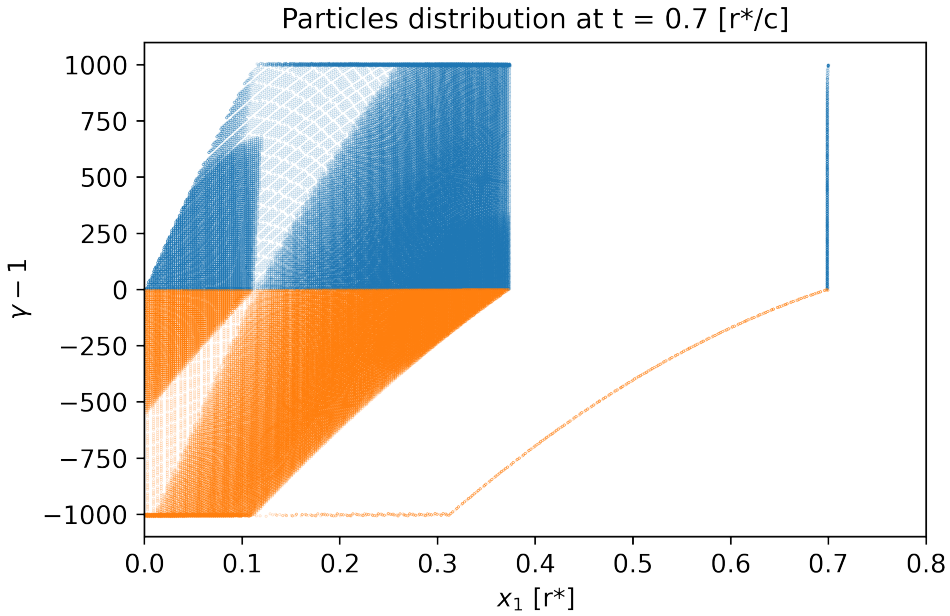

Figure 3.22: Leptons phase space distribution with $v_f = 0.6$, $f = 0.005$

Using the $v_f = 0.6$ and $f = 0.005$, values that have been proven to fit this investigation needs, a last simulation using this very setup has been performed, in order to grasp an idea of the plasma multiplicity obtained starting from a single electron in an already opened gap. Figure 3.22, as the previous ones deriving from different combinations of parameters at different times, shows the phase space distribution of electrons (in blue) and positrons (in orange). From that graph a second one, shown in Figure 3.23 below, has been derived, showing the leptons density according to the position and normalized to the total particle count.

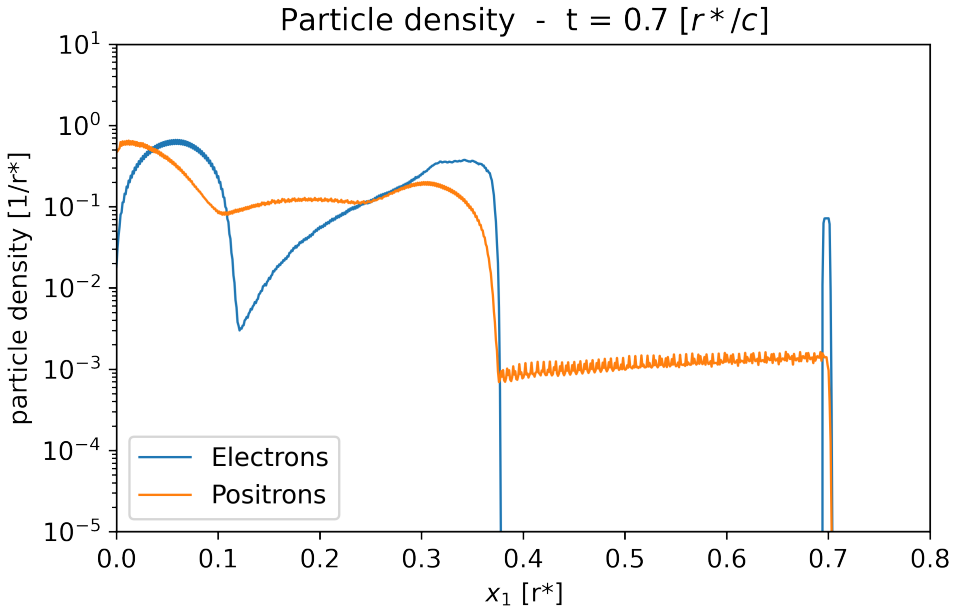

Figure 3.23: Electrons (blue) and positrons (orange) particle density at $t = 0.7\,[r^*/c]$, $v_f = 0.6$, $f = 0.005$, $\gamma_{\text{thr}} = 1000$

Let us begin with some considerations about electrons density. As expected, electrons population presents a sharp peak in $x = 0.7$ corresponding to the layer of the first progenitor, while the bulk is behind and corresponds to further generations of particles, initially pair created by positrons, and their progeny. The presence of distinct particles clusters, created by different generations of positrons, well reflects the "bump behavior" of the global electrons population evolution. Another significant detail stands in the magnitude of the particle density in the different regions: the first layer, despite driving the particle growth in the first stages of the cascade process, becomes less and less significant since the successive layers present an increasingly higher density, all according to the consideration drawn at the beginning of this section.

Moving to the positrons density, one could distinguish mainly two regions. The low-density interval, located between the first two electrons clusters, corresponds to a region in which no pair-production occurs and where the only particles present are the positrons streaming leftwards that were generated in the first layer. When pair-production starts again in earlier positions we have the onset of the consequent generation of particles, which are feeding the second region of high positrons density. Contrary to the electrons density distribution, the positrons one tends to be more uniform: this is due to those particles drifting in the opposite direction of their progenitors, hence not accumulating in layers which are necessarily denser the earlier their onset.

The so-obtained densities in the bulk regions closer to the surface are demonstrated to be already sufficient to satisfy the required plasma multiplicity, which is needed to fill an opened gap and re-establish the ρ_{GJ} density, according to the theory. The current model has proven to be good proof of the conceptual results obtained in the analytical treatment of these phenomena. However, the biggest issue with this setup is the distance from the actual events that I am trying to model in this Thesis, since no pulsar magnetosphere could be simplified with single electrons starting this complex events. I therefore decided to switch to a different setup, closer to the physical events, which is described and investigated hereafter.

3.4 Uniform positrons distribution

The setup in question is very similar to the one adopted in Section 3.2.1: a uniform positrons distribution with density ρ_{GJ} is subject to a linearly-growing externally-imposed electric field which is initially null. The initial density is chosen in order to reach the plasma equilibrium according to the theory described in Section 2.3.1, which is completely satisfied by the solely positrons since there are no electrons whatsoever.

Despite having access to the phase space distribution of all the leptons for different sets of plasma parameters at different time instants, analytically verifying the evolution of all the particles in the system was still too arduous of a challenge since we lack a global model that describes it. In the current section I hence decided to stick with a qualitative analysis of the simulations results while finding proof of conceptual results only for few selected layers of particles, in order to have a confirmation to be on the right track. A more quantitative analysis with deeper links with the analytical models can be found in the following Section 3.5.

On top of the consideration taken on this setup in Section 3.2.1, in Figure 3.24, performed with $v_f = 0.6$, $f = 0.05$ and $\gamma_{\mathrm{thr}} = 1000$, one could immediately notice the high particle density in earlier positions, populated by later generation of particles with higher multiplicity, and in the regions close to $\pm\gamma_{\mathrm{thr}}$.

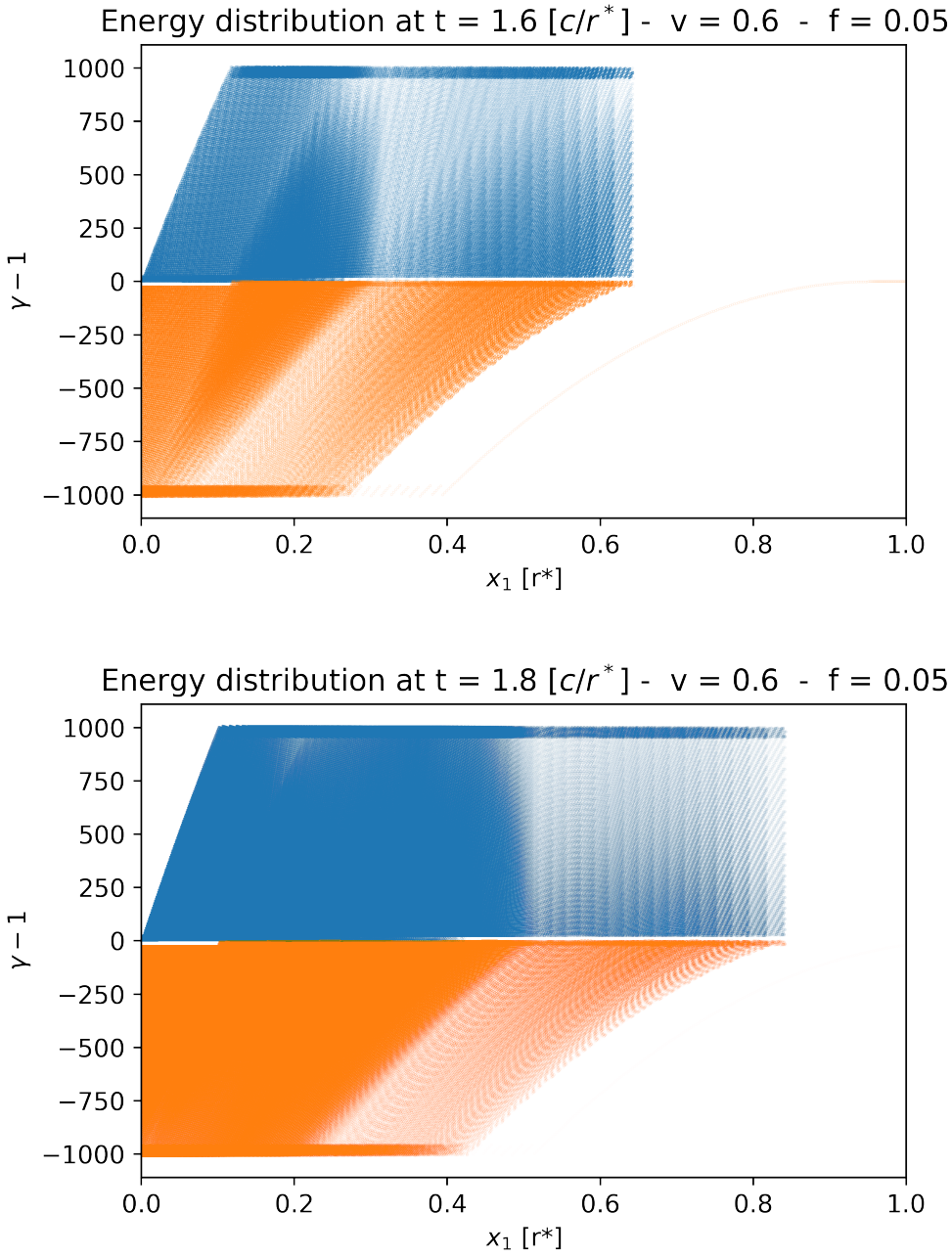

Figure 3.24: Top: electrons (blue) and positrons (orange) phase space distribution at $t = 1.6\,[r^*/c]$
Bottom: electrons and positrons phase space distribution at $t = 1.8\,[r^*/c]$
Both the diagrams have been obtained starting from a uniform $\rho_{\rm GJ}$ positron distribution with $v_f = 0.6$, $f = 0.05$ and $\gamma_{\rm thr} = 1000$.

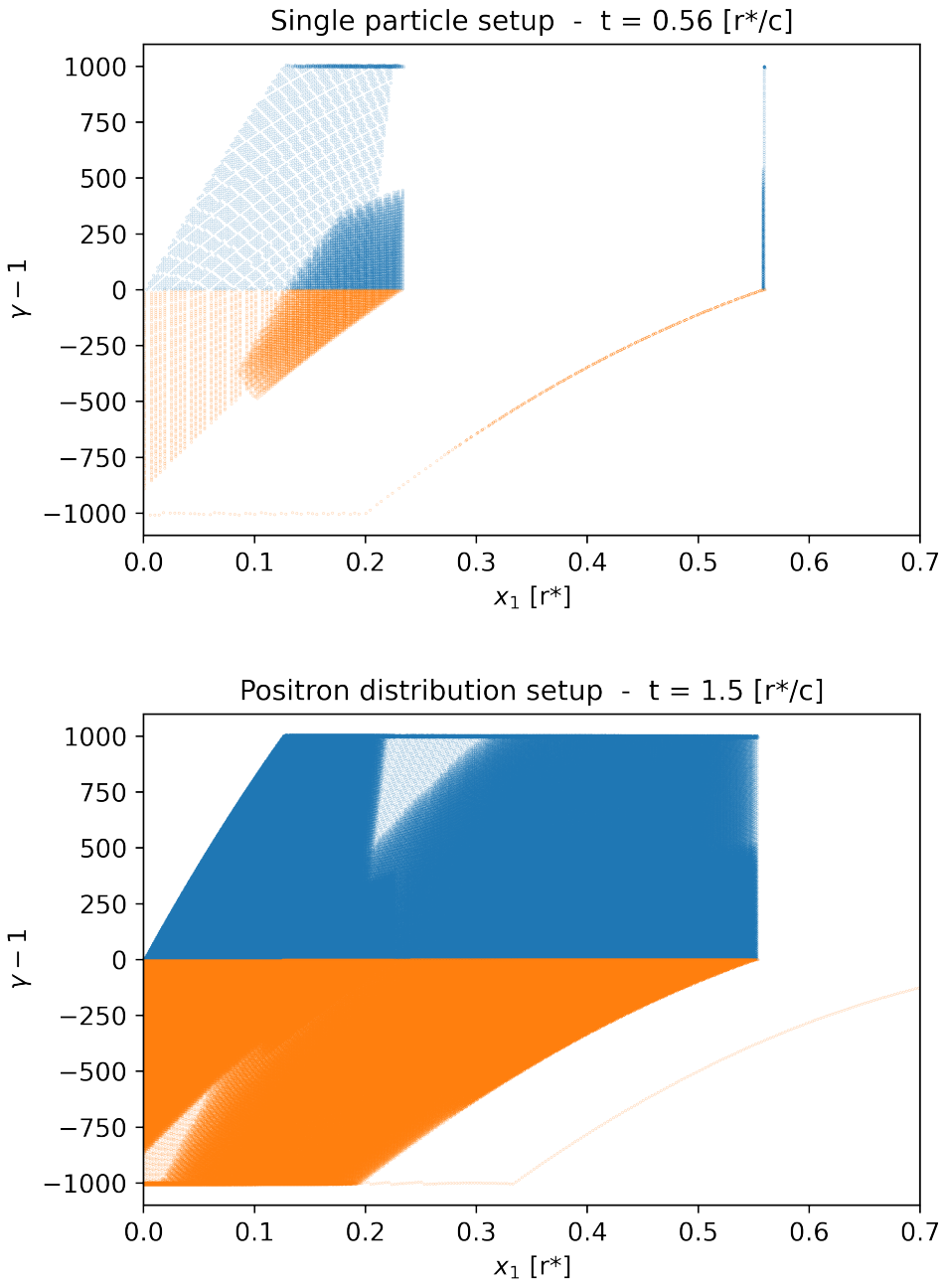

Figure 3.25: Top: Leptons phase space distribution at $t = 0.56\,[r^*/c]$ using a single particle setup.
Bottom: leptons phase space distribution at $t = 1.5\,[r^*/c]$ using a uniform positrons distribution setup
Both the diagrams have been obtained using $v_f = 0.6$, $f = 0.05$ and $\gamma_{\text{thr}} = 1000$.

What is quite significant in this qualitative analysis is the comparison between the two setups treated until now: Figure 3.25 shows the diagrams of the leptons phase space distribution both for the the single-particle and the positrons-distribution setups, in which the same $v_f = 0.6$, $f = 0.05$ and $\gamma_{\text{thr}} = 1000$ have been adopted. In order for the different simulations to be somehow comparable, performing a time shifting has been necessary: while the single-particle setup starts with an already opened gap (otherwise the progenitor couldn't be accelerated whatsoever) the uniform-positron-distribution one starts with null electric field and has the first electron pair-produced at the surface at τ_0. This characteristic time, which is $\tau_0 = 0.94\,[r^*/c]$ for the selected $v_f = 0.6$ and $f = 0.05$, then corresponds to the difference in time to be adopted between the two simulation plots in order to have corresponding first layers in the same position $x = 0.56\,[r^*]$. With the time-shifting applied, the second diagram is nothing but the superposition of many plots, each one corresponding to the progeny of each of the initial positrons that pair produce after τ_0. The first diagram is then a part of the second one, and the different regions of superposition could be noticed without effort: there is the first electron layer in $x = 0.56\,[r^*]$, the stream of positrons deriving from it (which marks the bottom-right boundary for the bulk of positrons in the second plot) and the region of pair production close to the surface, with the very same structure but different density due to the different multiplicity of the two simulations.

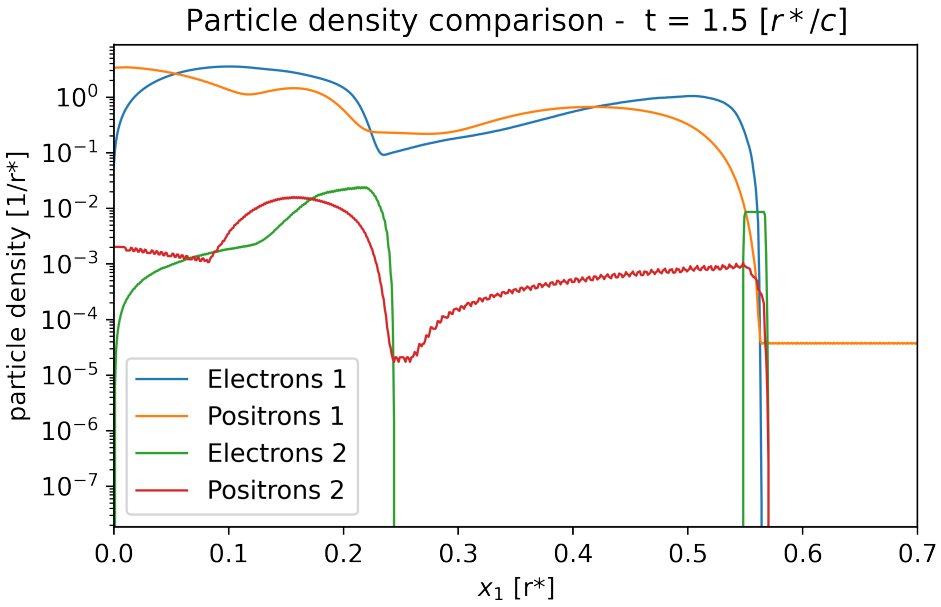

Figure 3.26: Comparison in the particle density of leptons with $v_f = 0.6$, $f = 0.05$ at $t = 1.5\,[r^*/c]$ corresponding to Figure 3.25. Population "1" refers to the uniform positron distribution setup, while population "2" to the single particle one.

Those comparisons in the particle density distribution can be appreciated directly in Figure 3.26, in which the particle density of leptons for both the abovementioned setups are plotted with the same discretization and scales. The similarities depicted previously can be observed in some regions, where the abrupt change in the slope of the curves coincide to the onset of other particle populations onset, which in turn corresponds to the onset of pair production sources.

The two curves that are most alike are, unexpectedly, the ones corresponding to the electrons of population "1" and to the positrons of population "2": the two distributions share the same behavior both in the electrons gap of single-particle setup and in the region right behind it, with the main difference standing in the different order of magnitudes of the particle densities. This strong resemblance can be explained by comparing the sources of the particles that populate that region: in the single particle setup those are positrons streaming leftwards as they're pair emitted by the first layer electrons each t_p, while in the uniform distribution setup those are the electrons drifting rightwards which are locally emitted by positrons that follow the previous behavior, hence pair producing with the same regularity (with the difference in magnitudes given by the sources).

The two electrons populations contrast is made explicit in Figure 3.27, in which the phase space distributions of this specie are plotted for both the setups.

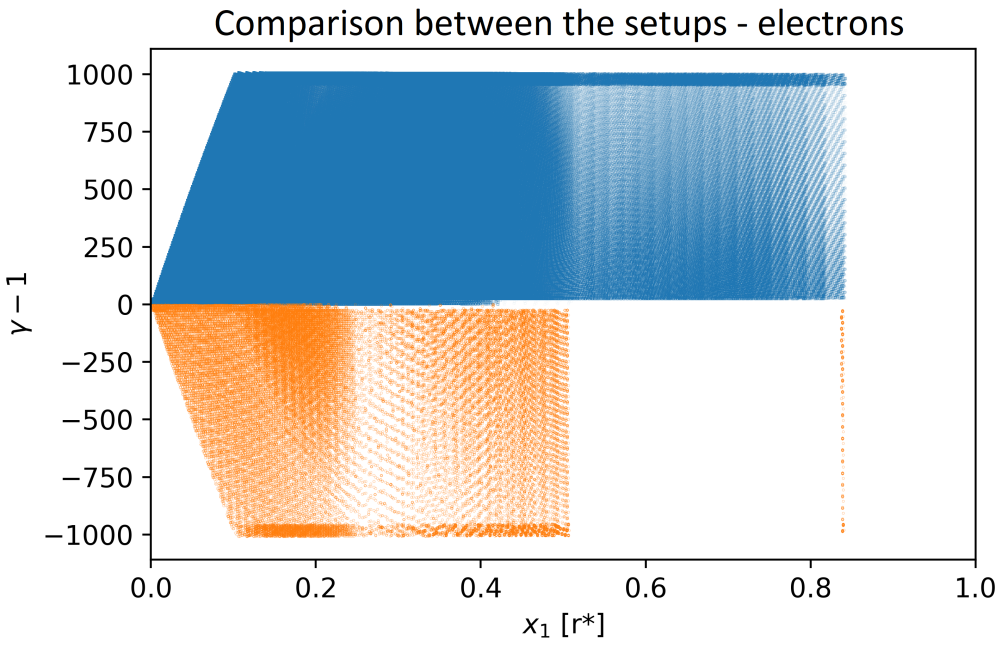

Figure 3.27: Comparison in the electrons phase space distribution for the uniform distribution setup (blue) and the single particle one (orange).

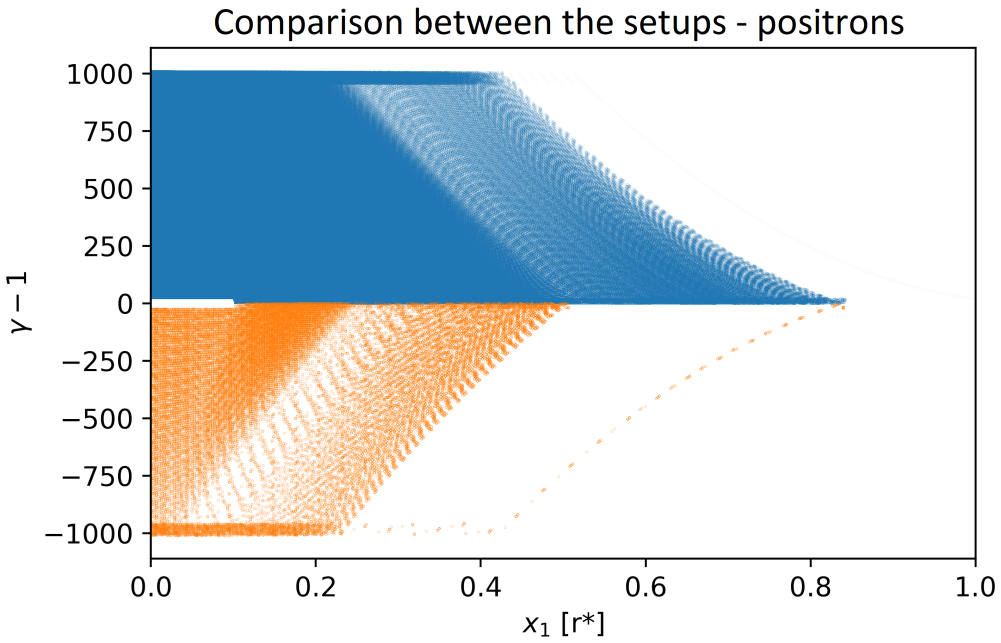

Figure 3.28: Comparison in the electrons phase space distribution for the uniform distribution setup (blue) and the single particle one (orange).

As before, a time shifting by τ_0 has been necessary in order to perform a proper comparison. An analogous graph for positrons is showed in Figure 3.28. In both diagrams one could grasp the resemblances in the space distribution behavior within a certain specie: that is due to the characteristic times t_a and t_p not being dependant on the particles distribution and count, since the electric field they experience is externally-imposed and not always self-consistent.

3.5 Layers characterization

The previous section revolved around deepening the study on the uniform distribution setup and performing some qualitative analysis aimed at comparing it with the single particle one. Despite it has been possible to find some proof of the analytical models, a thorough evaluation of the particle growth in the entire system was still not feasible: I hence decided to study consequent layers of particles in order to reconstruct a global behavior. Layers width basically describes the discretization chosen, as can be appreciated hereafter in Figure 3.29: starting from the first layer, I studied the evolution of the consequent regions of the chosen width in order to assess the growth rate behavior depending on the spatial position in phase space.

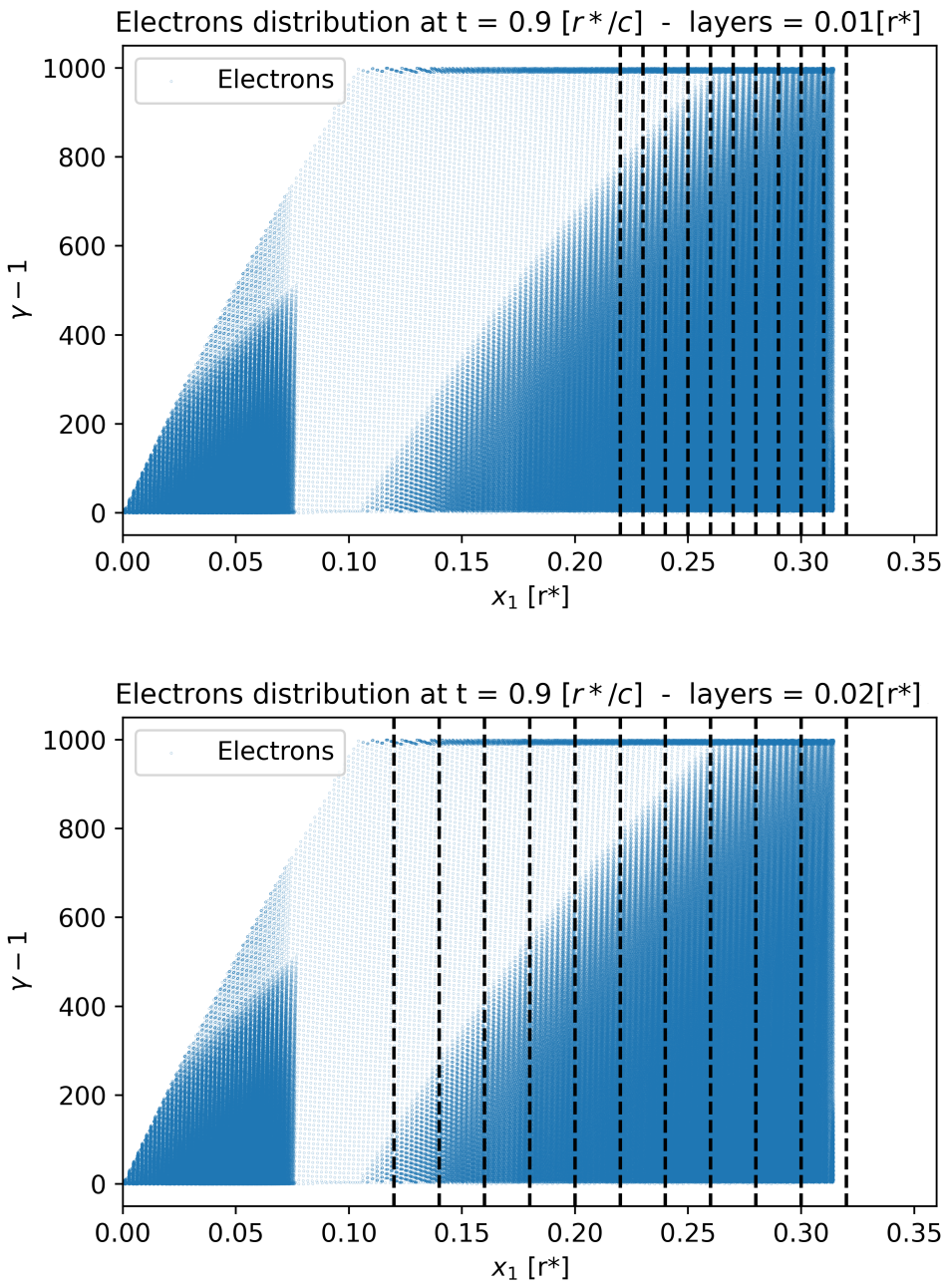

Figure 3.29: Electrons distribution at $t = 0.9\,[r^*/c]$, with $v_f = 0.9375$ and $f = 0.01$. The two identical plots are overlaid with different discretizations of space, performed thorough layer of thickness $l = 0.01\,[r^*]$ and $l = 0.02\,[r^*]$ starting from the already well-known first layer.

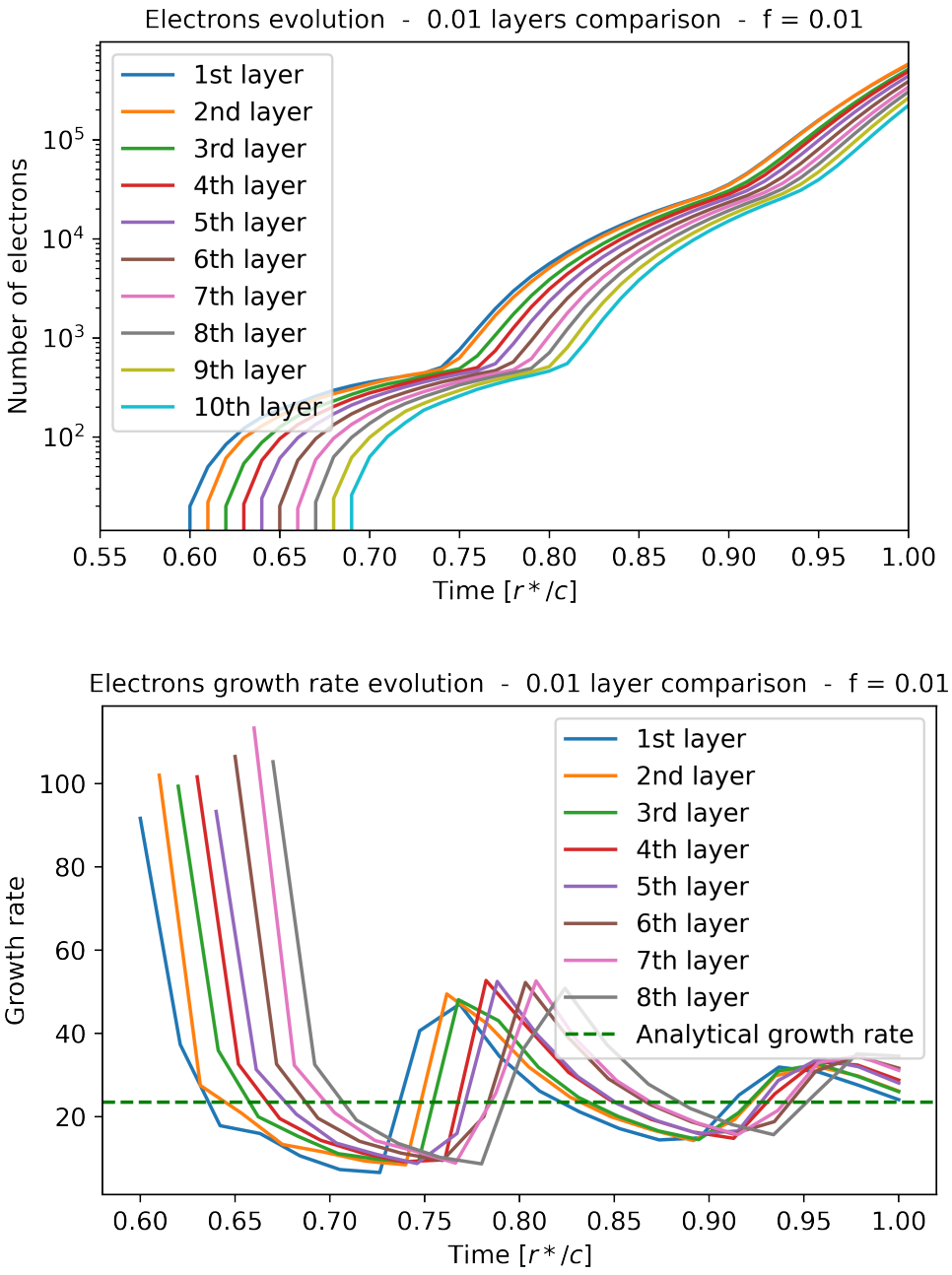

Figure 3.30: Top: Electrons population evolution in the different layers of thickness $l = 0.01\,[r^*]$ corresponding to the simulation results shown in Figure 3.29. Bottom: Corresponding growth rate evolution in the many layers. The green dotted line is the expected growth rate obtained analytically.

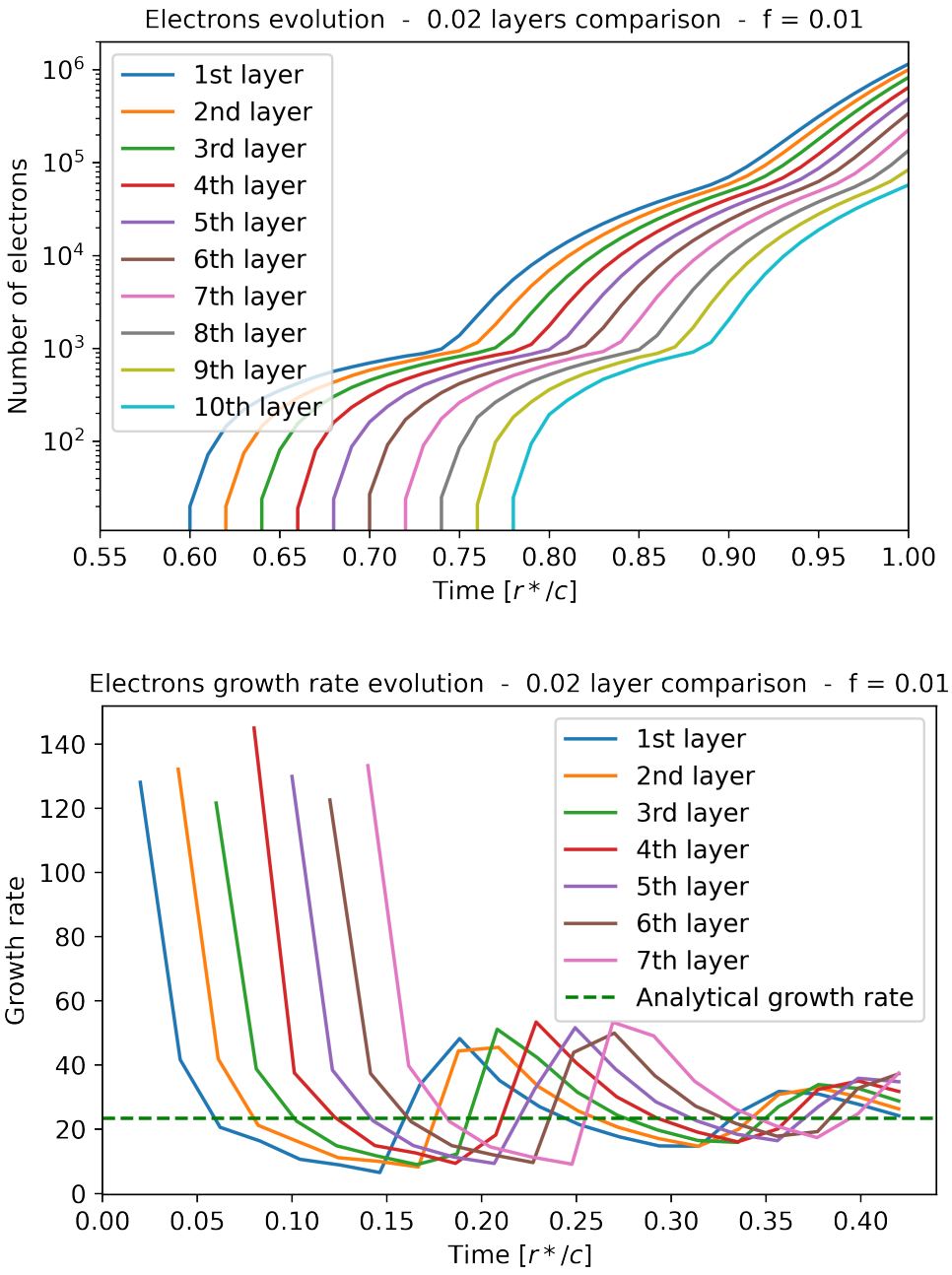

Figure 3.31: Top: Electrons population evolution in the different layers of thickness $l = 0.02\,[r^*]$ corresponding to the simulation results shown in Figure 3.29. Bottom: Corresponding growth rate evolution in the many layers. The green dotted line is the expected growth rate obtained analytically. The time axis here is shifted by a time $t = \tau_0$.

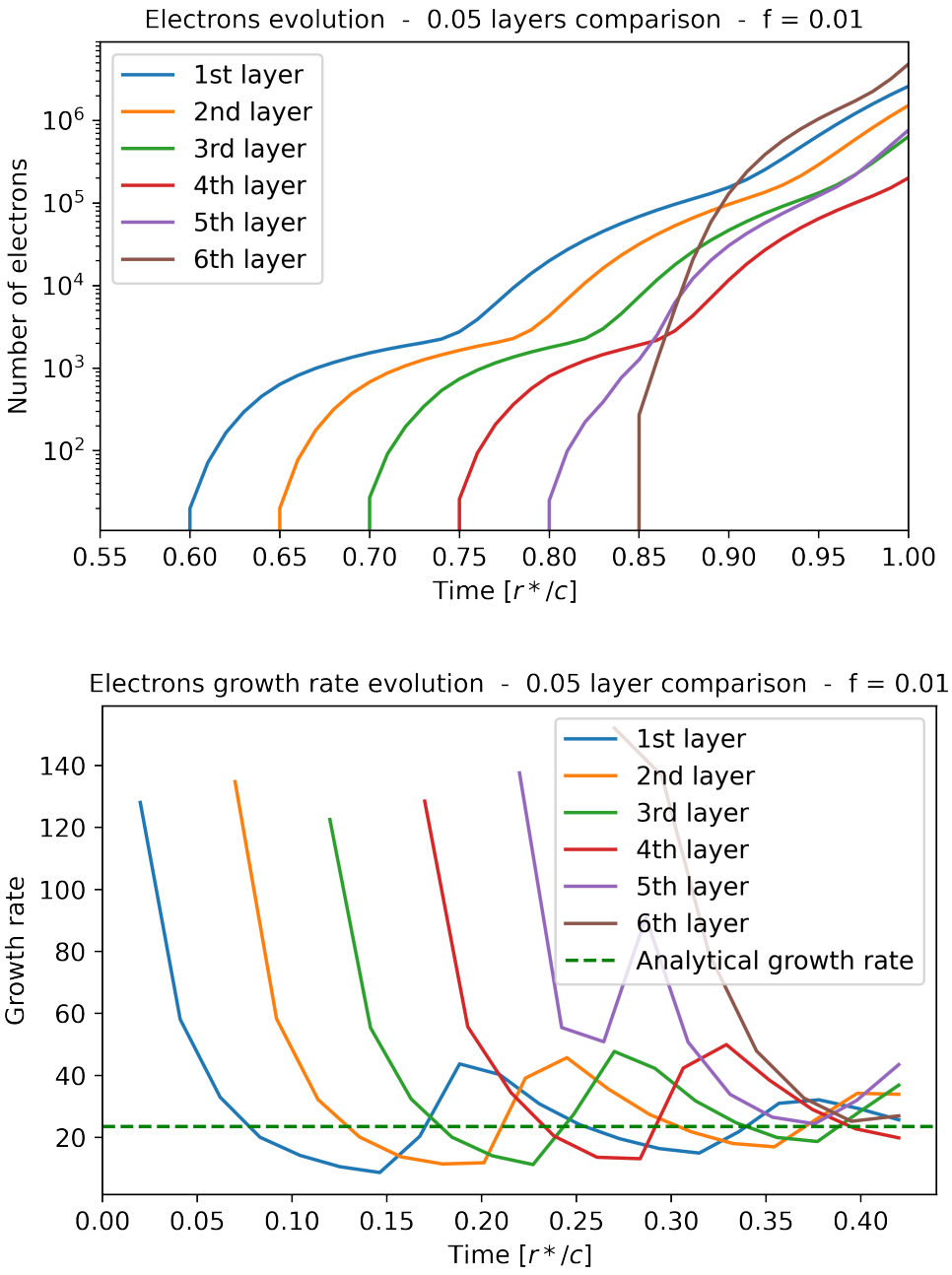

Figure 3.32: Top: Electrons population evolution in the different layers of thickness $l = 0.05\,[r^*]$ corresponding to the simulation results shown in Figure 3.29. Bottom: Corresponding growth rate evolution in the many layers. The green dotted line is the expected growth rate obtained analytically. The time axis here is shifted by a time $t = \tau_0$.

Layer thicknesses have been varied between $l = 0.01\,[r^*]$ and $l = 0.05\,[r^*]$. Values of $l < 0.01$ led to inconsistent descriptions of the layers behavior since we want them to be sufficiently wider than $t_p c$, while $l > 0.05$ has proven not to be useful in their characterization. I hereby show in Figure 3.30, 3.31 and 3.32 the evolution in time of the number of electrons in each layer and the corresponding growth rates for a multi-layered cascade where $v_f = 0.9375$ and $f = 0.01$, with layers of thicknesses $l = 0.01\,[r^*]$, $l = 0.02\,[r^*]$ and $l = 0.05\,[r^*]$ respectively.

Let us begin with underlining the common features shared by the plots. Firstly, independently on the observed layer, population and growth rate evolution are basically the same but shifted in time by l/c. The reason is that all layers move at approximately the speed of light, so each one behaves according to the models of growth in time described in the previous sections. The solely exception is the 6^{th} layer for $l = 0.05\,[r^*]$, whose growth is markedly different from the others since it completely encompasses the high-density region of the second burst of particles, which is intrinsically associated to higher multiplicities. The 5^{th} layer shows this behavior as well, just on a less extent since it only partially covers that high-density zone. Secondly, all the growth rates tend to converge into the expected value obtained, in a first approximation, with equation (2.12).

On top of the main difference, consisting in the l/c shift mentioned previously, the layers grow progressively faster from the front to the back of the cascade. This is a consequence of the electrons in the back layers experiencing a larger electric field at the time they are created (and thus throughout the development of their single-layered cascade). Moreover, the growth rate obtained analytically (2.43) using $\psi \simeq 0$ and $t_a(t) \simeq t_a^*$ fits reasonably well the average growth rate of the different layers as it would do if it was exactly constant asin the case of a constant and uniform externally-imposed field.

This kind of analysis has been performed for other combinations of v_f and f: while the change in the gap front velocity didn't add any additional information on the results of the parametric investigation of Section 3.3.2, the use of smaller values of f led to some useful considerations. Figure 3.33 and Figure 3.34 show the comparison in particle count and growth rate between different layers in simulations using, respectively, $f = 0.005$ and $f = 0.001$. The plots of the first panel are quite smooth thanks to the f being smaller than the one used in previous simulations. This leads to a reduced impact of possible numerical noise, which is usually correlated to the discretization chosen being too close to the scale at which pair production occurs (t_p/c), for the same reason for which thinner layer cannot be used. Inversely, plots in the second panel are affected by the opposite numerical issue: lower f means lower t_p, hence higher multiplicity and larger particle count growth in the unit time, which leads to larger variance in the values obtained during post-processing. This is evident in the bottom plot of Figure 3.34, where the growth rate is quite swinging contrary to the previous results.

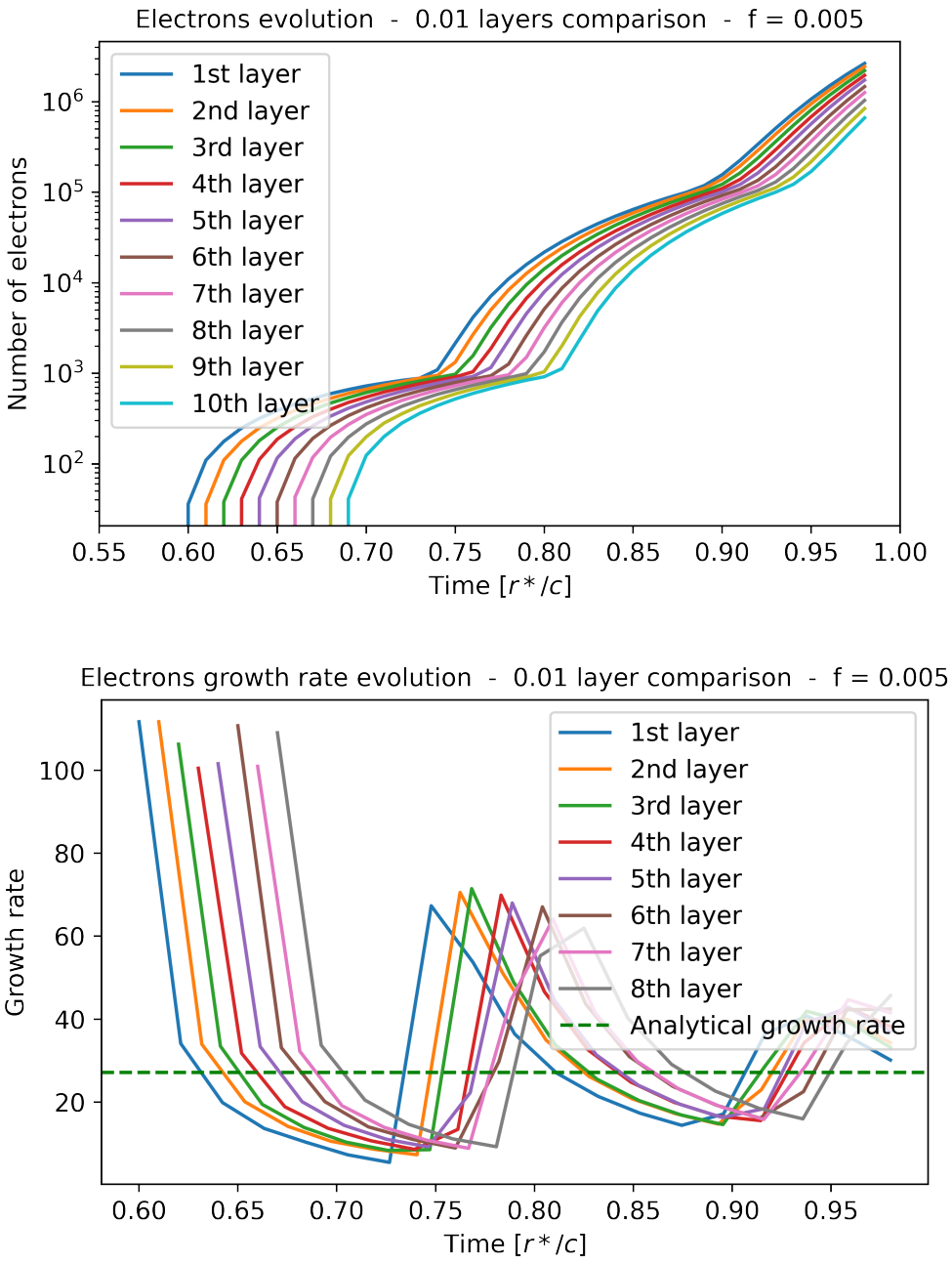

Figure 3.33: Top: Electrons population evolution in the different layers of thickness $l = 0.01\,[r^*]$, based on a simulation performed with $f = 0.005$.
Bottom: Corresponding growth rate evolution in the many layers. The green dotted line is the expected growth rate obtained analytically.

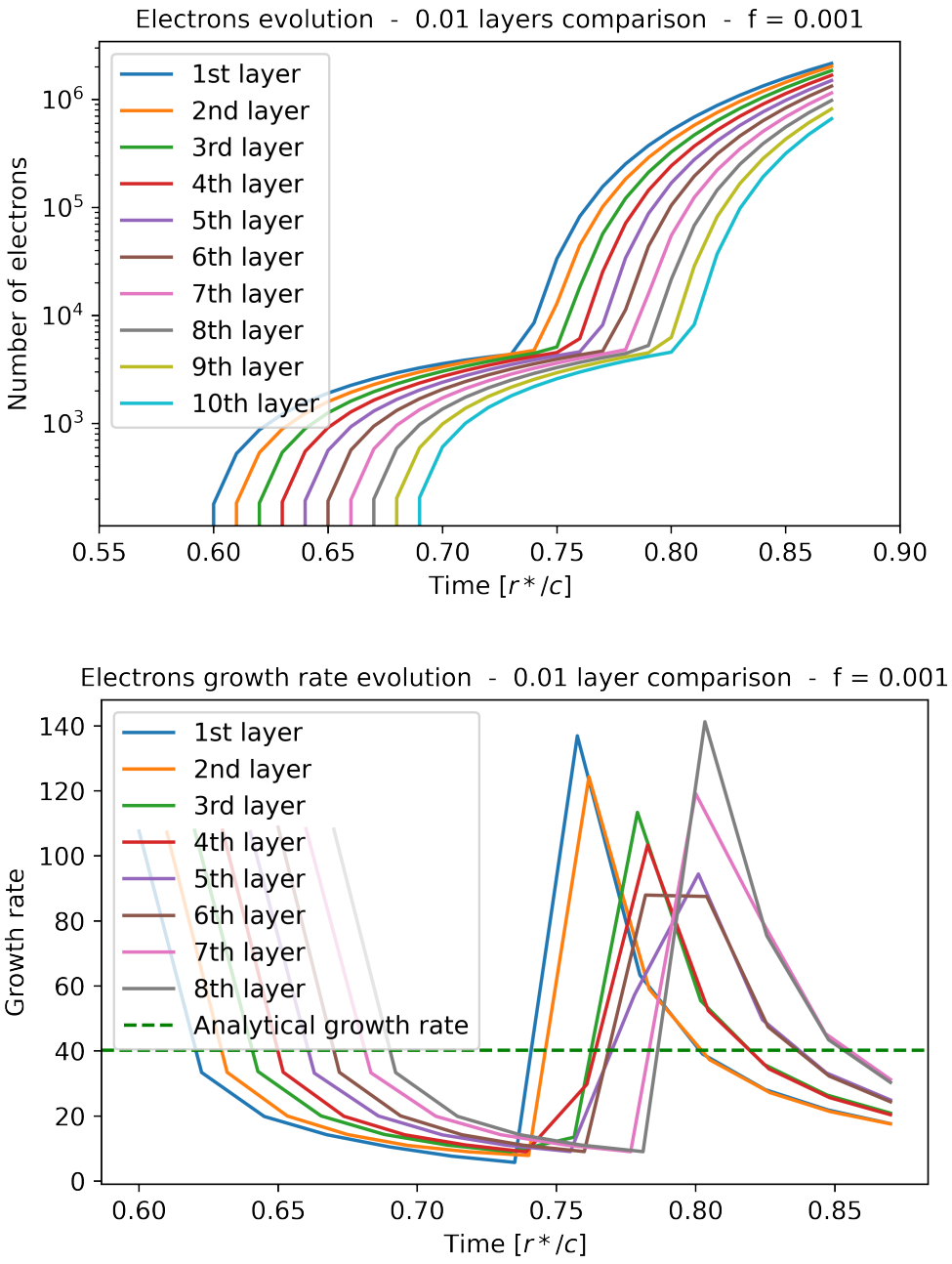

Figure 3.34: Top: Electrons population evolution in the different layers of thickness $l = 0.01\,[r^*]$, based on a simulation performed with $f = 0.001$.
Bottom: Corresponding growth rate evolution in the many layers. The green dotted line is the expected growth rate obtained analytically.

Simulations using $f = 0.001$ are also defective in being too quick in reaching the system maximum allowable particles count (just two "bumps" can be showed), hence not allowing any confirm in the convergence to analytical values as other simulation setups do. One last detail worth underlining are the actual expected growth rates obtained with the different plasma parameters: it spans between $\Gamma \gtrsim 20$ for $f = 0.01$ to $\Gamma \simeq 40$ for $f = 0.001$, in perfect agreement with eq.(2.12).

3.6 Spatial growth rate

The varying growth rate identified above for the different layers naturally gives rise to a non-uniform electron density spatial profile. This profile is shown in Figure 3.35 for $f = 0.001$ and in Figure 3.36 for $f = 0.005$. The plasma current has been chosen $j_m = -1.5\rho_{\rm GJ}c$ and the leptons density driving the E field evolution $n_- = 1.3n_{\rm GJ}$ for electrons and $n_+ = 0.3n_{\rm GJ}$ for positrons, which are slightly above the minimum necessary to maintain both the current and the Goldreich-Julian equilibrium. The corresponding gap front velocity is $v_f = 1.5/(1.3 + 0.3) = 0.9375$ and is the same as the one adopted in the previous section.

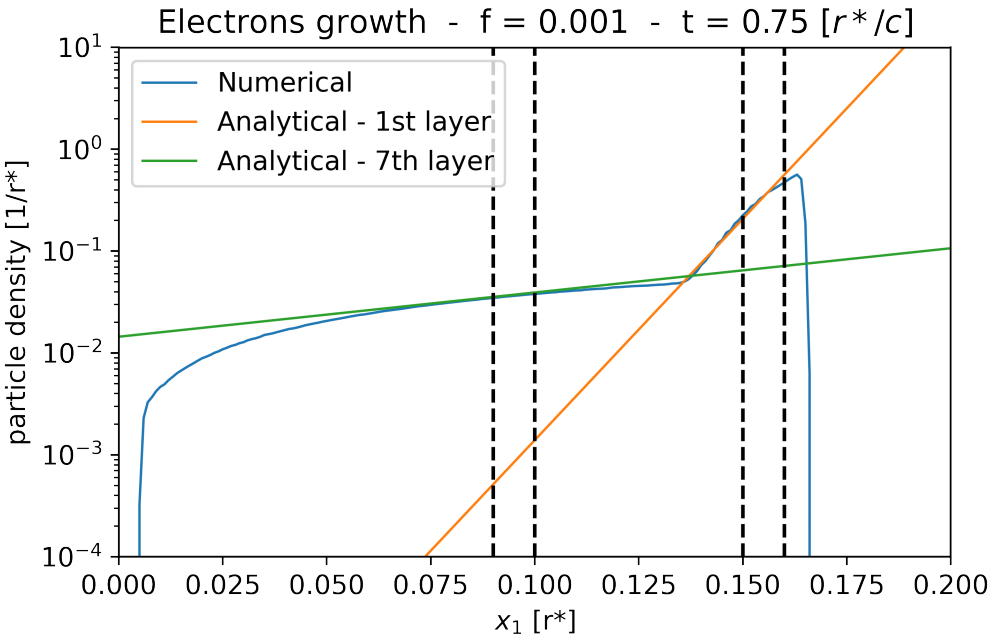

Figure 3.35: Electrons density profile (blue) at $t = 0.75\,[r^*/c]$, obtained in a simulation with $v_f = 0.9375c$ and $f = 0.001$, and estimates of the density profile for the 1^{st} (orange) and 7^{th} (green) layers.

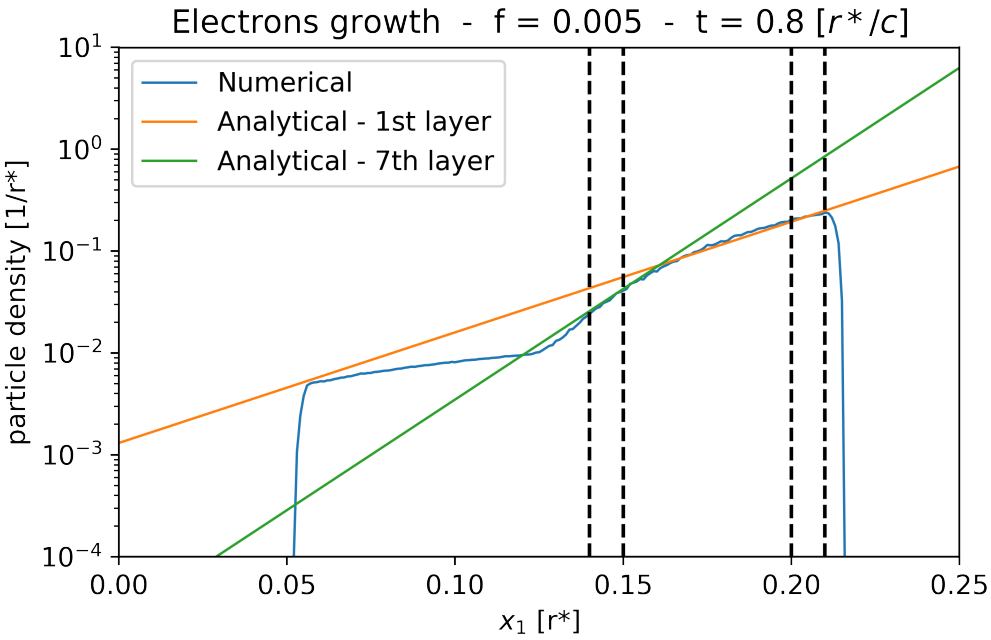

Figure 3.36: Electrons density profile (blue) at $t = 0.8\,[r^*/c]$, obtained in a simulation with $v_f = 0.9375c$ and $f = 0.005$, and estimates of the density profile for the 1^{st} (orange) and 7^{th} layers (green).

Despite the lower growth rate in time of the front layers, the density decreases from the front to the back of the cascade. This happens because layers at any distance d behind the head are created with a temporal lag d/c, which for the time shown in Figure 3.35 and 3.36 is not enough to flatten (or reverse) the electron density profile. Simulations and analytical comparisons using other sets of parameters have been used, but smaller values of f led to non-negligible numerical noise in the post-processing of data.

The number of particles in each layer evolves according to equation (2.54) presented in Section 2.6. Since the electric field varies slowly in space, the density between layers does not vary abruptly and can be written as $n(x,t) = n_0 \exp(\Gamma(t + x/c))$ (2.58). This estimate holds for as long as the growth rate of individual layers is approximately the same, and has been proven to be valid in early times of the cascade. In the figures above, I plotted lines with slopes computed with equation (2.58) for sample layers L01 and L07, which are shown to be in good agreement with the local shape of $n_{-}(x,t)$ obtained from the simulation. This result is quite important since it proved that the multi-layered cascade process, at least in the early stages and using physically acceptable parameters, evolves with the same Γ both in time and in space.

The approximate profile in equation (2.58) can finally be used to compute the time it takes to screen the electric field. Since the front of the cascade is the denser than the back, the field is first screened also at this position when $n_- \simeq -j_m/ec$. Since $|j_m| \simeq (1-2)|\rho_{GJ}|c$ and, from previous simulations, $n_-(t)$ grows from an initial density $\simeq (0.01-0.1)|\rho_{GJ}|/e$, then the screening time is $t_S \simeq 1/\Gamma(t_a^*)$. Given that $\Gamma(t_a^*) \simeq W(1/f)t_a(t_a^*)$ - from equation (2.43) - and that $W(1/f) \simeq 3-5$ for $f \simeq 10^{-6} - 10^{-3}$, $t_S \simeq t_a(t_a^*)$ can be finally estimated. For realistic pulsars, t_S varies between 10^{-9} and 10^{-6} s with the increasing rotation period, a result in good agreement with previous theoretical and numerical predictions.

3.7 Self-consistent setup

In previous section I derived analytical estimates for the spatiotemporal growth of the cascade and validated them against 1D PIC simulations, including heuristic pair production. Furthermore, I have estimated the time at which the plasma generated in the cascade first screens the gap electric field. These results have been proven to be consistent with 1D PIC simulations of pair cascades, including pair production from first principles, but what about in self-consistently developed electric fields? Up until now, all the simulations have been performed with leptons densities that were sufficiently small for them not to be able to perturb the externally-imposed electric field, which was the only driver of particles motion. I thus decided to perform additional sets of simulations in which the only electric field was the self-consistent one generated by the particles themselves, which is the actual phenomenon taking place in the pulsar magnetosphere.

The initial setup consists in a uniform distribution of electrons with density $n_- = 2n_{GJ}$ and positrons with density $n_+ = n_{GJ}$, contrary to the previous setups in which only a single specie with negligible density was present at $t = 0$. Those values has been chosen in order to ensure the equilibrium of the system $\rho = \rho_- + \rho_+ = \rho_{GJ}$ at $t = 0$ when the gap opens due to the current j_m. The corresponding gap front velocity is $v_f = 1.5/(1+2) = 0.5$ while $f = 0.01$ and $\gamma_{\rm thr} = 1000$ have been chosen. As already explained, leptons drift in opposite directions due to the current, generating the linear electric field in the opened gap near the surface, as observable in the top plot of Figure 3.37. At $t \simeq 0.85\,[1/\omega_p] = \tau_0$ the first electron is pair produced on the surface and is followed by a series of analogous events. Due to the high density of positrons, the electrons count in the gap increases quite rapidly, leading to a sudden drop in the self-consistent electric field (bottom plot of Figure 3.37): here is when the simulation differs from the ones of previous sections, for which the E field continued growing unaffected by the presence of the newly-born leptons. It is worth noticing that, despite the drop, the field is still negative, hence particles continue being accelerated towards $\gamma_{\rm thr}$, just more slowly.

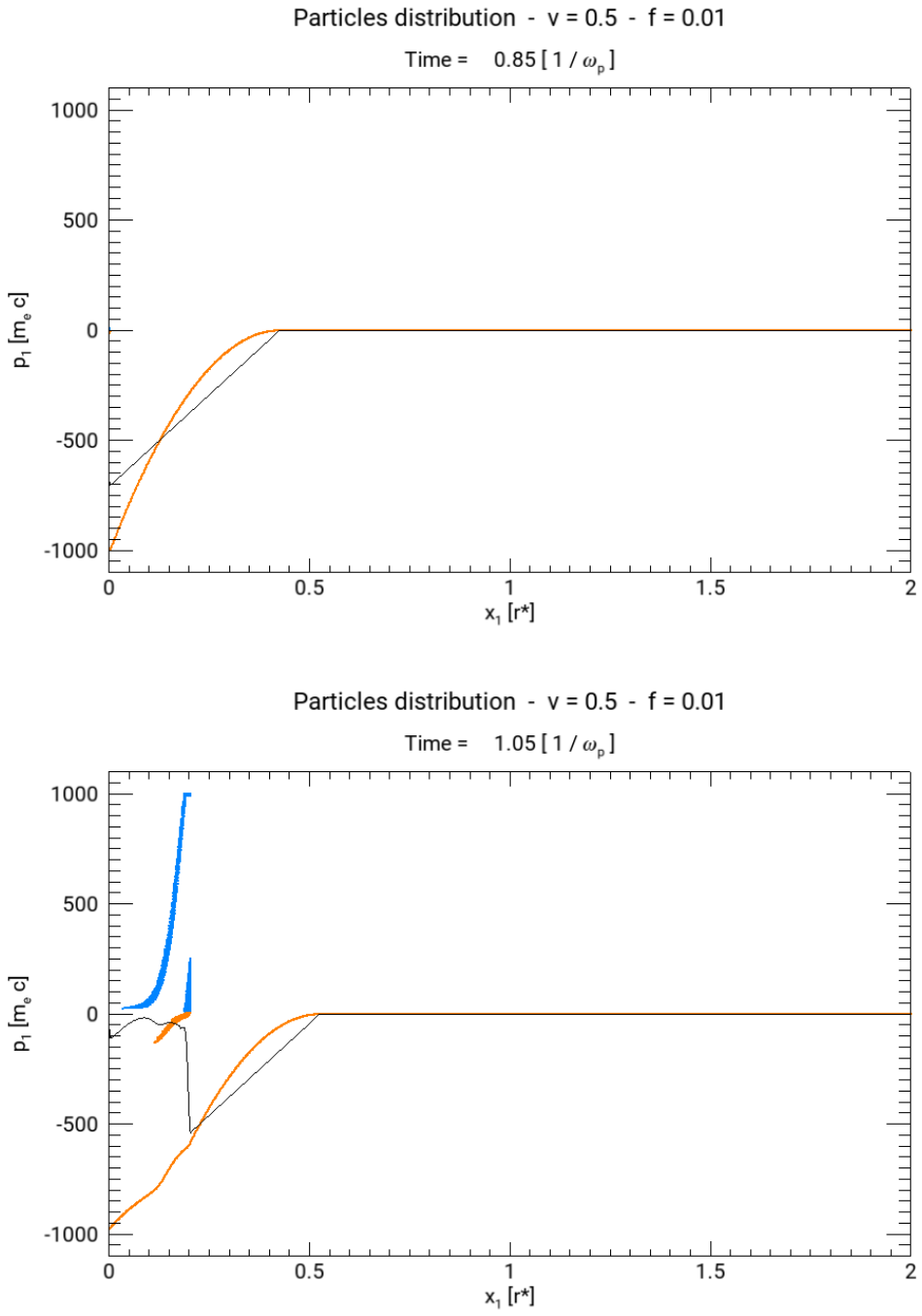

Figure 3.37: Electrons (blue) and positrons (orange) phase space distribution at time $t = 0.85\,[1/\omega_p]$ (top) and time $t = 1.05\,[1/\omega_p]$ (bottom) resulting from a simulation with $v_f = 0.5$, $f = 0.01$ and $\gamma_{\text{thr}} = 1000$. The self-consistent electric field (black) stop increasing after pair-production events take place.

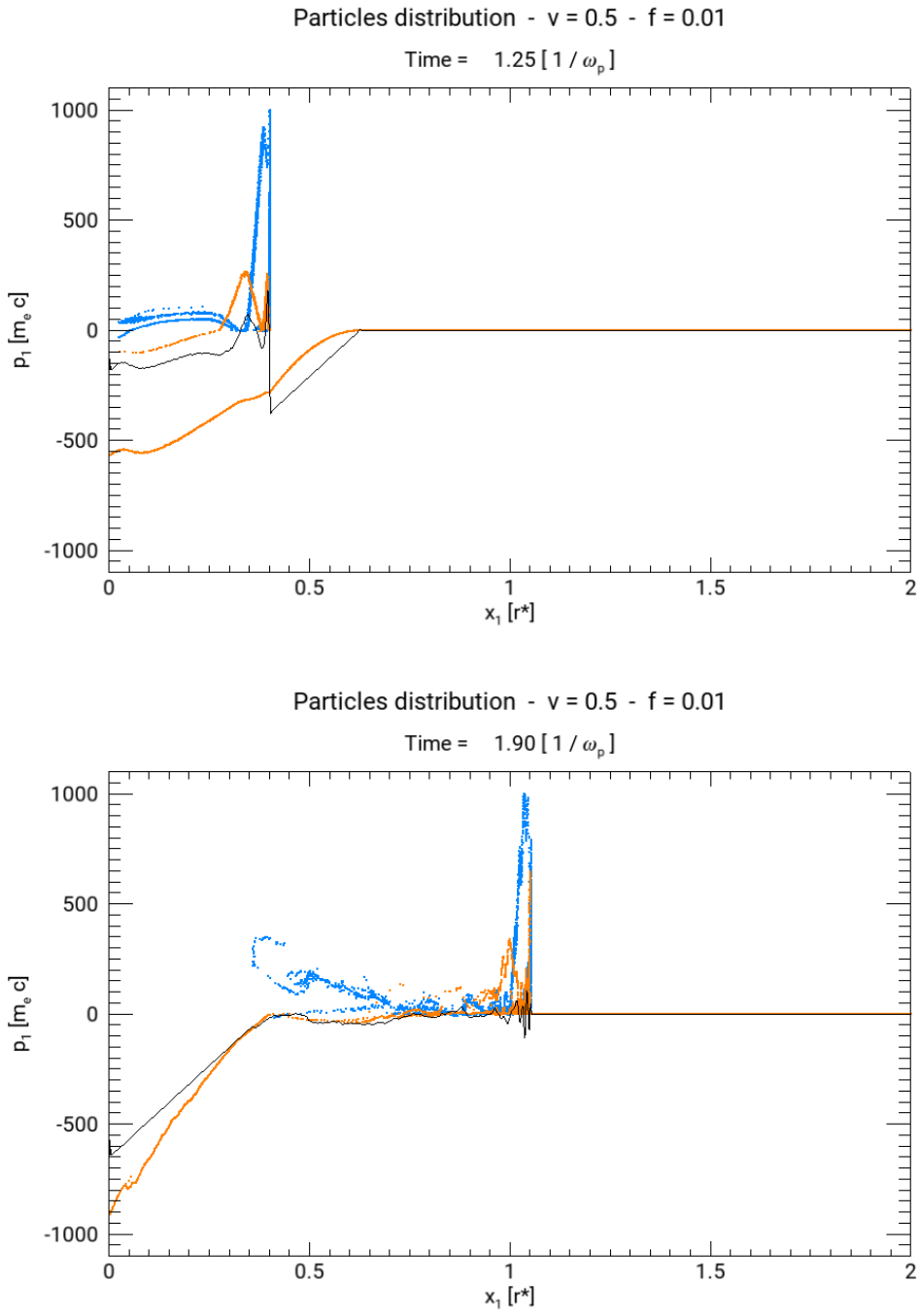

Figure 3.38: Leptons phase space distribution at time $t = 1.25\,[1/\omega_p]$ (top) and time $t = 1.90\,[1/\omega_p]$ (bottom). The first gap gradually closes since the E vanishes close to the front, while a second gap opens near the surface.

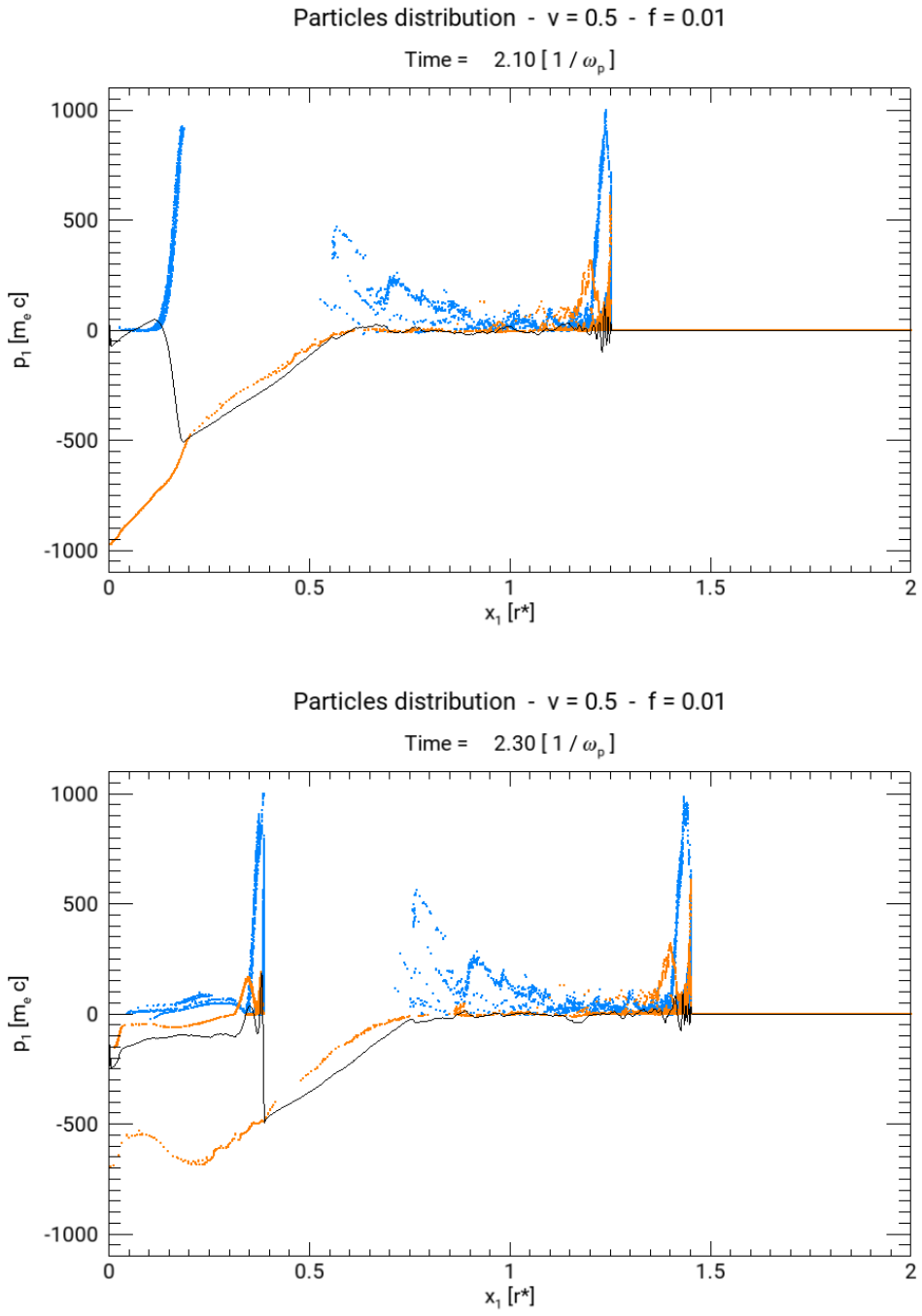

Figure 3.39: Leptons phase space distribution at time $t = 2.10\,[1/\omega_p]$ (top) and time $t = 2.30\,[1/\omega_p]$ (bottom). The second gap, as the first one, is filled with freshly-produced plasma and gradually closes.

The burst of electrons eventually leads to the reversal of the electric field, resulting in a temporary stop in pair production events since particles are now accelerated in the opposite direction (decelerated), as one could notice in the top plot of Figure 3.38. The leptons multiplicity reached sufficiently high levels to fill the gap and close it, leading to a sort of settling when the Goldreich-Julian density is reached again. After that, as observable in the bottom plot of Figure 3.38, a new gap develops, following an analogous behavior as before: the electric field grows linearly again, until the positrons are accelerated again to the threshold and give rise to another cascade event, as in the top plot of Figure 3.39. The second gap, just like the first one, closes after some time, as hinted in the last plot.

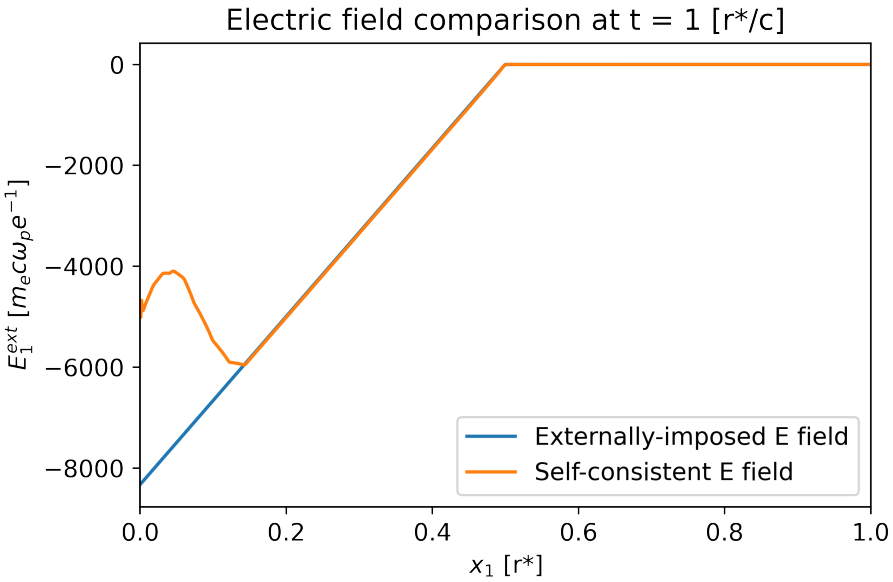

Figure 3.40: Comparison of the externally-imposed electric field for $v_f = 0.5$ and the self-consistent one at time $t = 1\,[r^*/c]$

In Figure 3.40 the self-consistent electric field is plotted together with the corresponding externally-imposed one. They both share a linear trait, which corresponds to the leptons drifting without pair production before τ_0, after which the self-consistent field start being screened by electrons while the other continues growing linearly. Since simulations in the previous section have been performed with arbitrarily small leptons density, such that their impact on the global field would be negligible, fields with an approximated magnitude and the desired v_f would be perfectly acceptable for simple qualitative analysis. However, the magnitude cannot be arbitrary for accurate quantitative investigations but has to grow according to equation 2.19 accurately described in Section 2.3.

As expected, plasma multiplicity is reached quickly enough to fill the gap with fresh plasma and close it. The time scales for which this occurs are comparable to the ones predicted in the previous section. The alternating pair production bursts, which occur which a certain regularity, have been proven to be responsible of producing inductive plasma waves. The mechanism is as follows: as the current grows in time, the electric field is screened, as prescribed by Ampere's law (1.8); when the field is screened, the plasma current is maximum, which reverses the field, decelerating particles. The system enters a stage where the electric field is approximately constant in space and oscillates in time inductively, i.e., supported by reversals of the plasma current. The frequency of these oscillations is the relativistic plasma frequency, $\omega_0 = \sqrt{4\pi e^2 n_\pm / \gamma_{\rm thr} m_e}$. In this stage, electrons and positrons periodically reverse their momentum without producing new pairs. With time, inductive oscillations become unstable [20] and perturbations in the electric field accelerate a small fraction of particles beyond $\gamma_{\rm thr}$, producing new bursts of pair production.

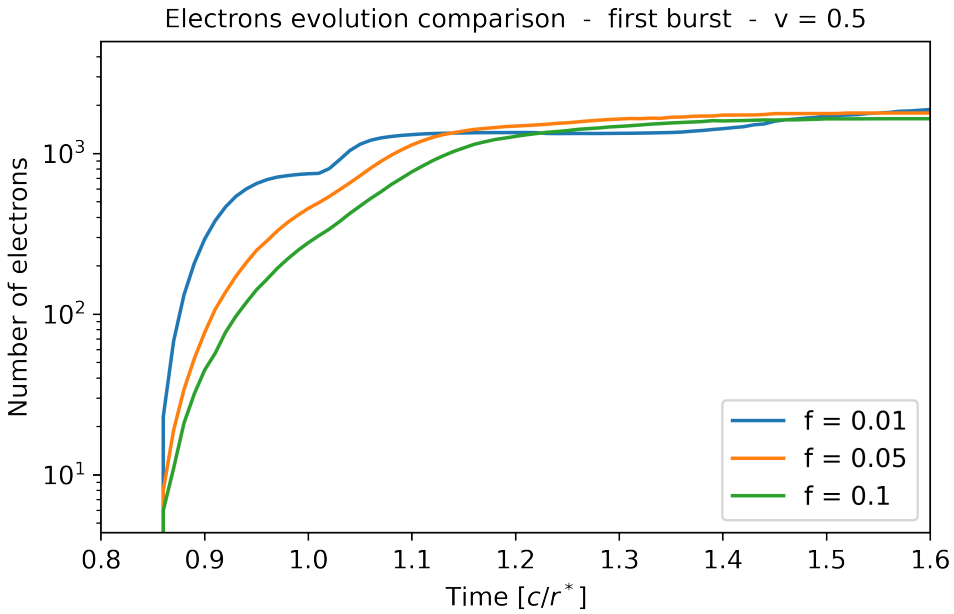

Figure 3.41: Comparison of the number of electrons evolution in the first burst for $v_f = 0.5$ and different values of f.

A parametric analysis has been performed by varying the value of f with $v_f = 0.5$ - which is now imposed by fixing the initial density and not by making a field growing at the required speed. Results for evolution of electrons are shown in Figure 3.41, while Figure 3.42 displays the corresponding growth rates.

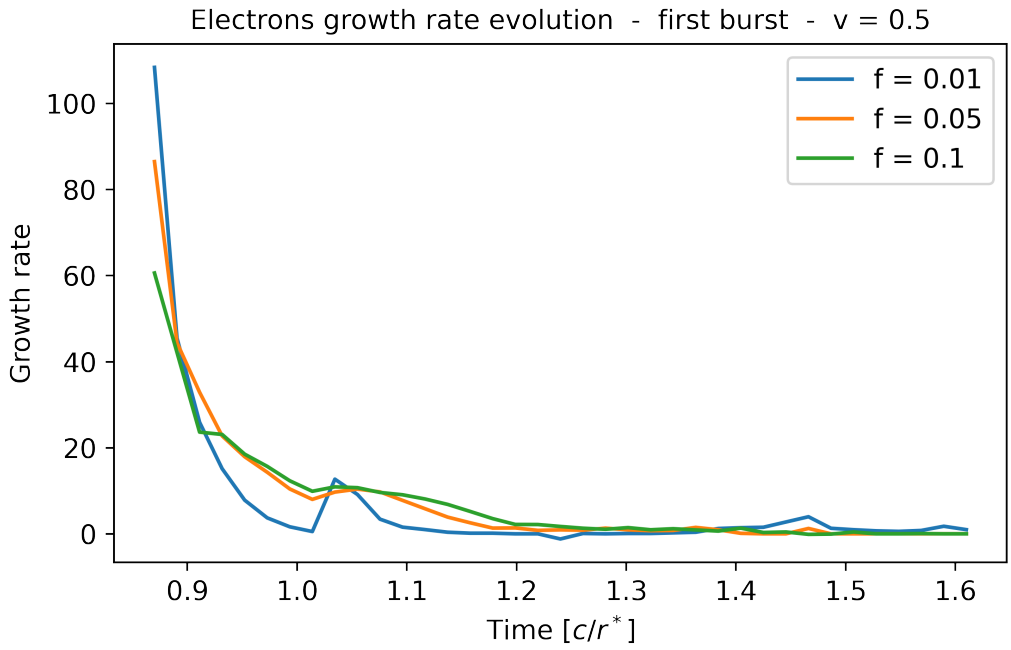

Figure 3.42: Comparison of the electrons growth rate evolution in the first burst for $v_f = 0.5$ and different values of f.

As expected, the electrons population plateau quite quickly, sign that the plasma multiplicity obtained is sufficient to screen the opened gap and stop the pair production cascading process. Smaller values of f lead to a faster growth right after τ_0, hence screening the E field more rapidly: this reflects on the lower growth rate right after, since the gap is already almost closed. It is worth underlining how the number of electrons required to completely screen the field is the same independently on the value of f, which only regulates the time at which the plateau is reached.

A comparison between the self-consistent setup with the externally-imposed field one is presented in Figure 3.43 for the particle population evolution and in Figure **??** for the corresponding growth rates evolution; $f = 0.01$ has been chosen for this investigation. While the current setup leads to a plateau, in the previous one the particle count continued to increase since the E field did the same. This is well reflected on the growth rates: in the self-consistent case it is vanishing when the field is totally screened, while in the externally-imposed field case it gradually converges to the value expected from the analytical evaluations, since the growth becomes almost purely exponential.

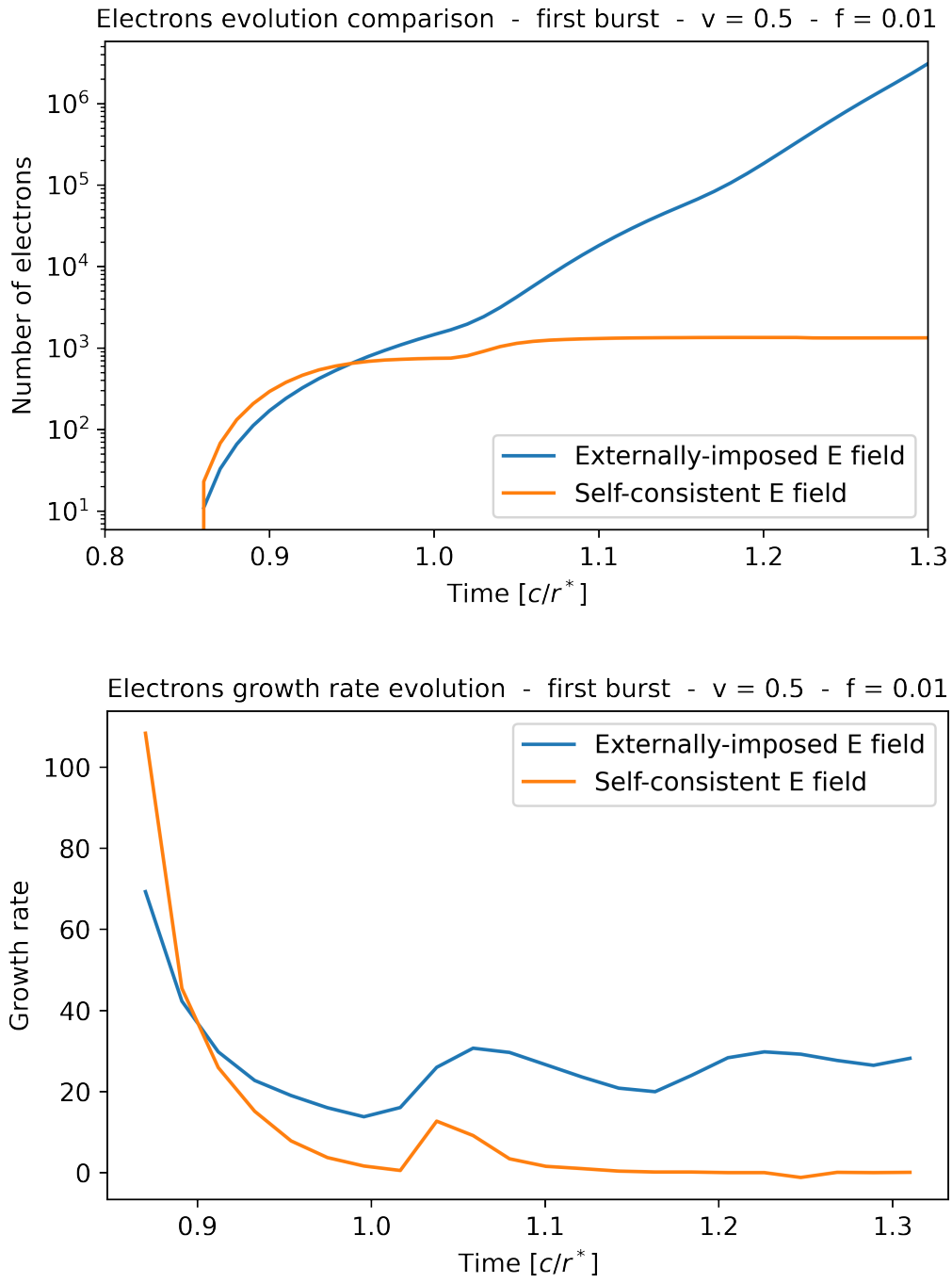

Figure 3.43: Top: electrons evolution comparison of the two field setups with $v_f = 0.5$ and $f = 0.01$.
Bottom: corresponding growth rates evolution.

The initial distribution having electrons density $n_- = 2n_{GJ}$ and positrons density $n_+ = n_{GJ}$, corresponding to a gap front velocity $v_f = 0.5$, it's quite an important landmark since it's the one setup with the maximum allowable leptons density for which the Goldreich-Julian equilibrium is still satisfied, resulting in the slowest v_f possible. This proved to be remarkable from a physical point of view considering that lower velocities imply weaker fields, hence less particles - lower multiplicity - required to shield it. Unfortunately, this comes with downsides when numerically approaching the problem: at the gap closing, the electric field still presents lots of peaks, which induce unnecessary particles fluctuations and potential numerical noise. Here came the choice of lowering as much as possible the positrons initial density with respect to ρ_{GJ} in order to smooth out the electric field.

The current induced by leptons drifting in opposite directions is $j_m = \rho_+ v_+ + \rho_- v_- = -\alpha \rho_{Gj} c$, with $\alpha = 1.5$, according to the theory presented in Section 2.3; the previous equation can be written in terms of the particle density as $(n_+ + n_-)v_f = 1.5 n_{GJ} c$ since positrons drift with $v_+ = -v_-$ and $v_f \equiv v_-$, hence:

$$\frac{v_f}{c} = 1.5 \frac{n_{GJ}}{n_+ + n_-} \tag{3.3}$$

The GJ equilibrium condition consists in $n_+ - n_- = n_{GJ}$, hence the minimum densities that can sustain j_m are $n_- = 1.25 n_{GJ}$ and $n_+ = 0.25 n_{GJ}$. The following simulations start with $n_- = 1.3 n_{GJ}$ and $n_+ = 0.3 n_{GJ}$, resulting in $v_f = 0.9375$.

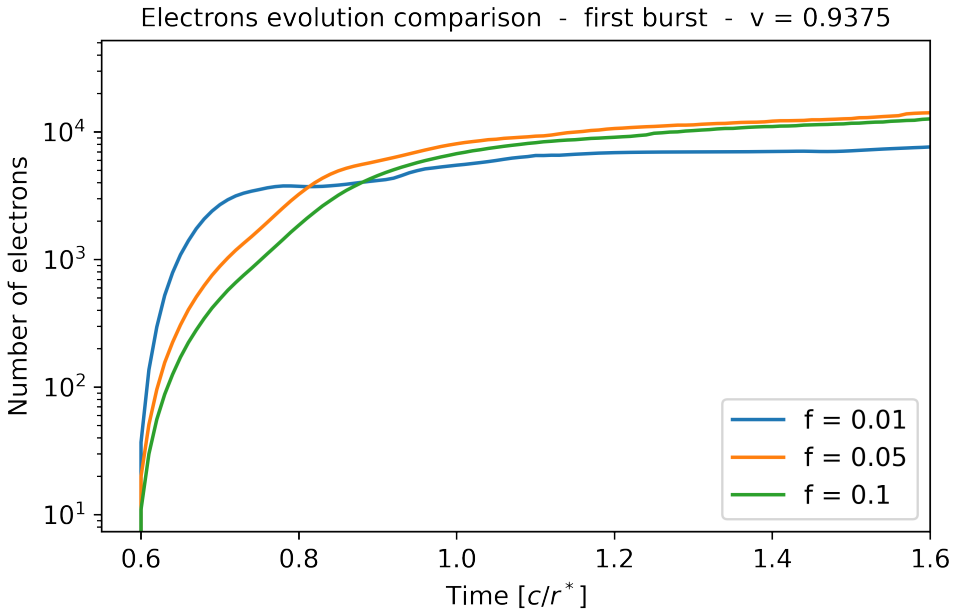

Figure 3.44: Electrons evolution comparison with $v_f = 0.9375$ and varying f.

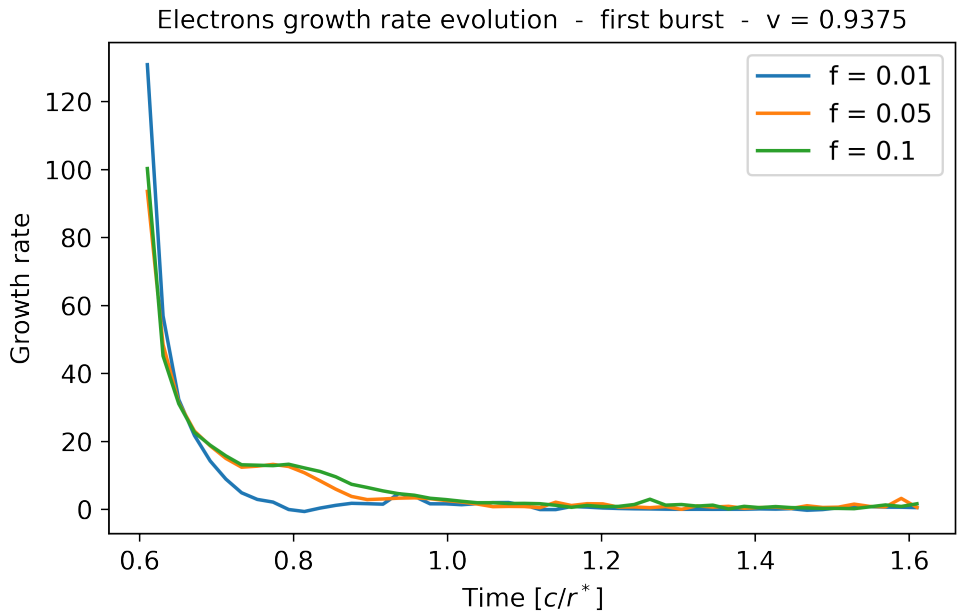

Figure 3.45: Electrons growth rates corresponding to the particle evolution of Figure 3.45. Independently on the f, the curves converge to 0 in a time $t \simeq 0.3\,[c/r^*]$ after τ_0.

Figure 3.44 is the result of a parametric analysis made by varying f while the initial leptons distribution led to the desired $v_f = 0.9375$; Figure 3.45 shows the corresponding growth rates. While the overall behavior is similar to the one observed for the same analysis performed with $v_f = 0.5$, a few differences prove that this setup leads to a better smoothing and screening of the electric field: especially for low values of f, but also for higher ones in a less extent, both the particle count and the corresponding growth rate are much smoother than in the previous case. This confirms that higher gap front velocities, corresponding to lower initial particle densities, lead to a better response of the system in its capability of screening electric field generated by the particle current imposed. This can be explained by the fact that a stronger field, resulting from a greater v_f, accelerates particles more frequently, hence leading to a higher multiplicity which, in turn, leads to less oscillation induced by the currents present at the gap closing. The higher multiplicity can be observed in the particles count of the plateau, which passes from being $\simeq 10^3$ for $v_f = 0.5$ to being $\simeq 10^4$ for $v_f = 0.9375$.

To conclude, the electrons growth rate evolution for $f = 0.01$ and $f = 0.1$ are plotted in Figure 3.46, where the self-consistent and the externally-imposed E field cases are compared together with the expected growth rate analytically calculated.

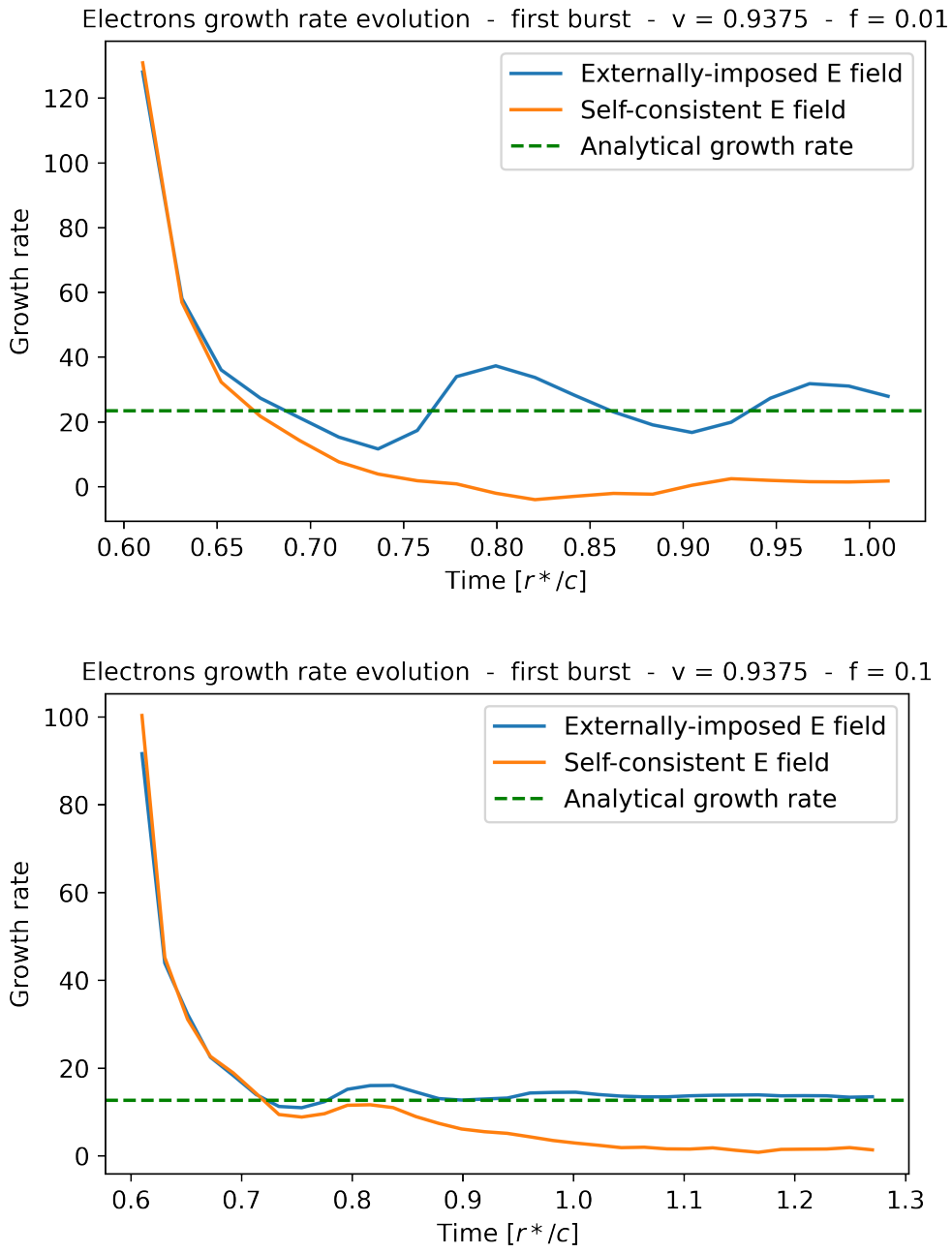

Figure 3.46: Comparison between the growth rates evolution between the self-consistent E field case (orange) and the externally-imposed E field one (blue) with the associated analytical growth rate (green). Both the diagrams have been produced using $v_f = 0.9375$, one with $f = 0.01$ (top) and the other with $f = 0.1$ (bottom).

Chapter 4

Conclusions

Heuristic models of pair cascades play a pivotal role in advancing our theoretical comprehension of the intricate dance between Quantum Electrodynamics (QED) and plasma kinetic effects. Within the scope of this study, I have undertaken a rigorous exploration of this dynamic interplay by employing a heuristic model that hinges on the concept of electrons and positrons generating fresh pairs each time they undergo acceleration beyond a predefined threshold energy. In particular, this investigation has centered around a comparative analysis of cascade development within constant and linear background electric field profiles. In the case of a uniform electric field, this research has unveiled an intriguing phenomenon: the proliferation of particles within the cascade follows an exponential growth pattern. I have gone a step further by juxtaposing the analytical estimate of this growth rate with empirical data gathered from simulations.

Furthermore, I have made a notable revelation in the context of cascades within a linear electric field. While exponential growth still characterizes these cascades, a distinct feature has emerged – the growth rate experiences a time-dependent decline. This phenomenon can be attributed to the diminishing strength of the electric field that seed particles within the cascade encounter as time progresses. Consequently, this leads to a spatially variable growth rate for the density of electron clouds generated in cascades near the surfaces of neutron stars. Specifically, the density of the leading edge of these clouds is expected to increase at a slower rate compared to their trailing edge. However, since the initial formation of the clouds occurs at the leading edge, the electron density exhibits a gradient, decreasing from the front to the rear.

These findings align with previous 1D Particle-in-Cell (PIC) simulations of pair cascades, encompassing pair production from first principles and self-consistently developed linear electric fields. I have not only derived analytical approximations for the spatiotemporal evolution of the cascade but have also corroborated these estimates through meticulous validation against 1D PIC simulations, incorporating

heuristic pair production.

Lastly, this research has ventured into estimating the critical point at which the plasma generated within the cascade begins to screen the gap electric field. The analysis of the properties of inductive waves, self-consistently generated as a consequence of pair cascades within a linear electric field, is a tantalizing avenue we've left for future exploration.

The insights forged through the analytical models outlined in this work serve as invaluable tools for interpreting more complex, full-fledged QED simulations of pair cascades. It's imperative to note, however, that their application is confined to the domain of validity of the heuristic model underpinning this study, specifically in scenarios characterized by a negligible photon mean free path. As we embark on the next phase of research into pair cascades within compact objects, it is envisaged to extend this model. Such extensions, and consequently, the theoretical framework elucidated here, are poised to propel our understanding closer to the realm of *ab initio* descriptions of pair cascades. This entails incorporating elements such as a soft energy threshold for photon emission and the incorporation of a finite photon mean free path, be it constant or spatially dependent.

In essence, this work forms the cornerstone upon which future investigations into the intriguing world of pair cascades in compact celestial objects will be built, taking us further along the path of unraveling the mysteries of the universe at its most fundamental levels.

Bibliography

[1] D. Carreto Fidalgo. «Pulsars and Pulsar Wind Nebulae». In: *Springer theses* (2019). DOI: 10.1007/978-3-030-24194-0_2 (cit. on p. 1).

[2] A. Hewish, S. J. Bell, J. D. H. Pilkington, P. F. Scott, and R. A. Collins. «Observation of a Rapidly Pulsating Radio Source». In: *Nature* 217.5130 (Feb. 1968), pp. 709–713. ISSN: 1476-4687. DOI: 10.1038/217709a0. URL: https://www.nature.com/articles/217709a0 (visited on 06/15/2021) (cit. on p. 1).

[3] T. Gold. «Rotating neutron as the origin of the pulsating radio sources». In: *Nature* 218 (1968), pp. 731–732. DOI: 10.1038/218731a0 (cit. on p. 1).

[4] A. A. Abdo et al. «The first Fermi Large Area Telescope catalog of gamma-ray pulsars». In: *Atrophys. J., Suppl. Ser.* 187(2) (2010), pp. 460–494. DOI: 10.1088/0067-0049/187/2/460 (cit. on p. 1).

[5] T. Gold. «Rotating neutron stars and the nature of pulsars». In: *Nature* 221 (1969), pp. 25–27. DOI: 10.1038/221025a0 (cit. on p. 1).

[6] D. B. Melrose and M. Z. Rafat. «Pulsar radio emission mechanism: Why no consensus?» In: *J. Phys. Conf. Ser* 932(1) (2017), p. 012011. DOI: 10.1088/1742-6596/932/1/012011 (cit. on p. 2).

[7] P. Goldreich and W. H. Julian. «Pulsar electrodynamics». In: *Astrophys. J.* 157 (1969), p. 869. DOI: 10.1086/150119 (cit. on pp. 2, 3).

[8] F. Cruz. «Multiscale modeling of pulsar magnetospheres». PhD thesis. 2021 (cit. on pp. 3, 5, 9, 13, 14).

[9] P. A. Sturrock. «A Model of Pulsars». In: *The Astrophysical Journal* 164 (1971), p. 529. DOI: 10.1086/150865 (cit. on p. 3).

[10] A. N. Timokhin. «Time-dependent pair cascades in magnetospheres of neutron stars – I. Dynamics of the polar cap cascade with no particle supply from the neutron star surface». In: *Monthly Notices of the Royal Astronomical Society* 408.4 (Nov. 11, 2010), pp. 2092–2114. ISSN: 0035-8711. DOI: 10.1111/j.1365-2966.2010.17286.x. URL: https://doi.org/10.1111/j.1365-2966.2010.17286.x (cit. on pp. 4, 6, 15, 16).

[11] J. Arons and E. T. Scharlemann. In: () (cit. on p. 4).

[12] A. N. Timokhin and A. K. Harding. «On the maximum pair multiplicity of pulsar cascades». In: *The Astrophysical Journal* 871(1) (2019), p. 12. DOI: 10.3847/1538-4357/aaf050 (cit. on p. 6).

[13] F. Cruz, T. Grismayer, and L. O. Silva. «Kinetic Model of Large-amplitude Oscillations in Neutron Star Pair Cascades». In: *The Astrophysical Journal* 908.2 (Feb. 2021), p. 149. ISSN: 0004-637X. DOI: 10.3847/1538-4357/abd2c0. URL: https://doi.org/10.3847/1538-4357/abd2c0 (cit. on pp. 6, 12, 15).

[14] R. A. Fonseca. «Experimental and Numerical Study of Laser-Plasma Electron Accelerators». PhD thesis. 2012. DOI: 10.13140/RG.2.1.3712.7124 (cit. on p. 7).

[15] K. Yee. «Numerical solution of initial boundary value problems involving Maxwell's equations in isotropic media». In: *IEEE Trans. Antennas Propag.* 14(3) (1966), pp. 302–307. DOI: 10.1109/TAP.1966.1138693 (cit. on p. 8).

[16] C. K. Birdsall and A. B. Langdon. *Plasma physics via computer simulation*. Boca Raton: Institute of physics, 1991 (cit. on p. 9).

[17] T. Erber. «High-Energy Electromagnetic Conversion Processes in Intense Magnetic Fields». In: *Rev. Mod. Phys.* 38(4) (1966), pp. 626–659. DOI: 10.1103/RevModPhys.38.626 (cit. on p. 11).

[18] V. I. Ritus. «Quantum effects of the interaction of elementary particles with an intense electromagnetic field». In: *J. Russ. Laser Res.* 6 (1985), pp. 497–617. DOI: 10.1007/BF01120220 (cit. on p. 11).

[19] R. M. orless, G. H. Gonnet, and D.E.G. et al. Hare. «On the LambertW function». In: *Adv. Comput. Math.* 5 (1996), pp. 329–359. DOI: 10.1007/BF02124750 (cit. on p. 15).

[20] F. Cruz, T. Grismayer, and L. O. Silva. «Kinetic instability in inductively oscillatory plasma equilibrium». In: *Phys. Rev. E* 103 (5 May 2021), p. L051201. DOI: 10.1103/PhysRevE.103.L051201 (cit. on p. 77).

Appendix A

Published paper

Physics of Plasmas

AIP Publishing

Model of pulsar pair cascades in non-uniform electric fields: Growth rate, density profile, and screening time

Cite as: Phys. Plasmas **29**, 052902 (2022); https://doi.org/10.1063/5.0085847
Submitted: 19 January 2022 • Accepted: 05 April 2022 • Published Online: 04 May 2022

F. Cruz, T. Grismayer, S. Iteanu, et al.

COLLECTIONS

Paper published as part of the special topic on Papers from the 63rd Annual Meeting of the APS Division of Plasma Physics

View Online Export Citation CrossMark

Physics of Plasmas ARTICLE scitation.org/journal/php

Model of pulsar pair cascades in non-uniform electric fields: Growth rate, density profile, and screening time

Cite as: Phys. Plasmas **29**, 052902 (2022); doi: 10.1063/5.0085847
Submitted: 19 January 2022 · Accepted: 5 April 2022 ·
Published Online: 4 May 2022

F. Cruz,[1,a),b)] T. Grismayer,[1] S. Iteanu,[2] P. Tortone,[3] and L. O. Silva[1,c)]

AFFILIATIONS

[1]GoLP/Instituto de Plasmas e Fusão Nuclear, Instituto Superior Técnico, Universidade de Lisboa, 1049-001 Lisboa, Portugal
[2]Département de Physique, Univ. Lyon, ENS de Lyon, Univ. Claude Bernard, F-69342 Lyon, France
[3]Dipartimento di Energia, Politecnico di Torino, 10129 Torino, Italy

Note: This paper is part of the Special Collection: Papers from the 63rd Annual Meeting of the APS Division of Plasma Physics.
Note: Paper GI1 6, Bull. Am. Phys. Soc. 66 (2021).
[a)]Invited speaker.
[b)]**Author to whom correspondence should be addressed:** fabio.cruz@tecnico.ulisboa.pt
[c)]luis.silva@tecnico.ulisboa.pt

ABSTRACT

Time-dependent cascades of electron–positron pairs are thought to be the main source of plasma in pulsar magnetospheres and a primary ingredient to explain the nature of pulsar radio emission, a long-standing open problem in high-energy astrophysics. During these cascades—positive feedback loops of gamma-ray photon emission via curvature radiation by TeV electrons and positrons and pair production—the plasma self-consistently develops inductive waves that couple to electromagnetic modes capable of escaping the pulsar dense plasma. In this work, we present an analytical description of pair cascades relevant in pulsars, including their onset, exponential growth, and saturation stages. We study this problem in the case of a background linear electric field, relevant in pulsar polar caps, and using an heuristic model of the pair production process. The analytical results are confirmed with particle-in-cell simulations performed with the OSIRIS code that include heuristic pair production.

I. INTRODUCTION

Pulsars are rapidly rotating neutron stars permeated by magnetic fields that can exceed 10^{12} G. Their exotic magnetospheres are filled with highly relativistic pair-dominated magnetized plasma flows that transport the rotational energy of the neutron star. These flows are such that the pulsar magnetosphere is in the force-free regime almost everywhere.[1–3] This regime can be expressed by the condition $\mathbf{E}\cdot\mathbf{B}\simeq 0$, where $\mathbf{E}$ and $\mathbf{B}$ are the ambient electric and magnetic fields. Regions where this condition cannot be met are ideally suited for non-linear phenomena, such as (i) dissipation via, e.g., magnetic reconnection,[4] leading to high-energy gamma-ray emission[5] and (ii) pair cascades,[6,7] a feedback loop that supplies plasma to the magnetosphere.

In pair cascades, electrons and positrons are accelerated along the curved magnetic field of pulsars, emitting gamma-ray photons through curvature radiation that can be converted into new electron–positron pairs via Quantum Electrodynamics (QED) processes.[8,9] If emitting and newly born leptons are continuously accelerated, this mechanism can act as an efficient source of pair plasma that self-regulates:[6,7] it stops when the fresh plasma is dense enough to screen the background electric field and restarts if/when the plasma advects into other regions of the magnetosphere.

Vacuum gaps, i.e., regions of $\mathbf{E}\cdot\mathbf{B}\neq 0$ where cascades develop, can be located in polar caps,[6,7] near the stellar surface or in the outer magnetosphere.[10,11] Cascades operating at low altitudes have been conjectured to be intimately connected to coherent emission mechanisms from pulsars.[6,7] Recent advances in numerical algorithms and computational resources allowed a great progress in the understanding of pair cascades and their interplay with collective plasma phenomena. Timokhin[12] performed the first 1D simulations, including the relevant QED effects from first principles in plasma kinetic simulations, showing that cascades periodically launch large-density plasma blobs into the magnetosphere, generating coherent superluminal electrostatic waves.[13] Follow-up works[14,15] determined the spectra and multiplicity of the pair plasma created in cascades for a variety of initial conditions.

Physics of Plasmas ARTICLE scitation.org/journal/php

Recently, 2D simulations have shown that the modes identified in 1D simulations can be electromagnetic if the pair production fronts are not perfectly aligned with the local magnetic field.[16,17] These results demonstrated that the properties of pulsar radio emission can be intimately connected with the QED and plasma kinetic processes underlying pair cascades.

Exploring the intricate interplay between these processes with *ab initio* simulations is computationally very expensive. The large multiplicity of cascades and the consequent disparity between the size of the vacuum gaps (∼100 m) and the shortest plasma kinetic scales (∼1 cm) make 2D and 3D simulations very challenging, even when modeling only local simulation domains. Heuristic models of the QED processes emerged as a natural solution to this problem. These models replace the strong nonlinearities of the QED cross sections with simpler criteria, with the goal of lowering the computational costs of simulations of pair cascades.

A commonly adopted heuristic model consists in injecting electron–positron pairs at a rate that depends on the local electric and/or magnetic fields. This strategy has been used as a plasma source in global simulations of pulsar magnetospheres[18–22] to study the distribution of plasma currents in the vicinity of the neutron star, as well as particle acceleration in the current sheets that develop beyond the light cylinder, leading to gamma-ray emission consistent with observations. A second class of heuristic models replaces the criteria for QED processes to occur with thresholds based on typical energy or length scales associated with these processes. Such models are able to trace the development of pair cascades and, thus, capture more accurately the interaction between QED and plasma kinetic processes. These models have been used in local simulations of pair cascades,[13,16,23] but also in global pulsar magnetosphere simulations.[24–28]

Despite their wide use and known mapping to first-principles descriptions of the QED processes in some cases,[23] heuristic models remain poorly explored from a theoretical standpoint. These simple models are an important tool to understand the development of pair cascades and to rigorously derive estimates for, e.g., their growth rate, the plasma distribution functions that they produce and the types and properties of plasma waves excited. Such estimates are important to comprehend coherent emission processes triggered during the cascade process, but also other processes that depend on cascade products, namely, the properties of the plasma distribution function.[29,30]

In this work, we use an energy threshold-based heuristic model to analytically and numerically study the development of pair cascades. In Sec. II, we describe this model in detail and assume, for simplicity, that the cascade develops in a uniform background electric field to derive its properties. In Sec. III, we investigate how are the properties of the cascade modified with a more realistic linear electric field profile, in particular, how is its growth rate modified and how it changes in time and space. In Secs. II and III, we compare our analytical results with particle-in-cell (PIC) simulations. Our conclusions are finally presented in Sec. IV.

II. CASCADE IN A UNIFORM ELECTRIC FIELD

Polar cap pair discharges are regulated by two QED processes: (i) emission of gamma-ray photons by ultra-relativistic electrons and positrons via nonlinear Compton scattering,[8] the QED equivalent of curvature radiation,[31,32] and (ii) conversion of gamma-rays into electron–positron pairs via multiphoton Breit–Wheeler pair production.[9] The differential probability rates for these processes are well-known[8,9] functions of the parent particles' energy, momentum components, and local electromagnetic field components.

However, for typical pulsar parameters (the surface magnetic field of $B \sim 10^{12}$ G and a rotation period of $T \sim 1$ s), we can estimate the characteristic energy and length/timescales associated with these processes in polar caps. For instance, the energy at which electrons and positrons produce the most energetic photons is $\varepsilon_{\pm} \sim 10^7\, m_e c^2$, where m_e is the electron mass and c is the speed of light. The length scale associated with this process is the distance over which leptons are accelerated from rest to these energies, $\ell_{\pm} \sim 100$ m. The photons emitted by the ultra-relativistic leptons follow an energy spectrum that peaks at the critical energy $\varepsilon_{\gamma} \sim 10^2$–$10^3\, m_e c^2$, and decay into pairs after a typical propagation distance $\ell_{\gamma} \sim 1$–10 m.

In this work, we assume that these processes can be described by the following heuristic model of pair production: Any electron or positron accelerated beyond a threshold energy $\varepsilon_{\rm thr}$ emits a new electron–positron pair with a fraction f of its original energy, $\varepsilon_{\rm pair} \equiv f\varepsilon_{\rm thr}$, equally split between the pair particles. With this model, we assume that the intermediate photon decays instantaneously, i.e., $\ell_{\gamma} \ll \ell_{\pm}$, and that the QED processes occur at well-defined energies. These conditions are valid for the canonical parameters presented above. However, they become invalid, e.g., for pulsars with lower periods or weaker surface magnetic fields, for which the ratio ℓ_{γ}/ℓ_a can be significantly different and a one-dimensional description of the cascade is likely insufficient.[17]

For convenience, we parametrize the model presented in this work using the fraction f and the threshold Lorentz factor $\gamma_{\rm thr} = \varepsilon_{\rm thr}/m_e c^2$. In real pulsars, $\gamma_{\rm thr} \sim \varepsilon_{\pm}/m_e c^2 \sim 10^7$ and $f \sim 10^{-6}$–$10^{-3} \ll 1$, although exact estimates may depend on the magnitude and geometry of the surface magnetic field of the pulsar.[23]

In general, cascades develop in electric fields with spatial dependencies. For example, in polar cap vacuum gaps, the electric field varies in both altitude and latitude, leading to non-trivially shaped pair production fronts[16,33] and emission power profiles.[17] For simplicity, we assume in this work that the cascade can be described as a 1D problem along the magnetic field lines. This is a good approximation due to the strong magnetic fields that permeate pulsar magnetospheres, which forbids charged particles to cross magnetic field lines. In this section, we also assume that the cascade develops on a spatially uniform electric field with magnitude E_0. We investigated this scenario in detail in Cruz *et al.*.[23] In this section, we review the key results from that work in order to introduce notation and establish the theoretical framework required in the more complex scenario studied in Sec. III.

A. Population model

It is straightforward to determine the two relevant timescales of this system with electrons and positrons subject to a uniform electric field E_0 pair producing according to the heuristic model presented above: (i) $t_a \equiv \gamma_{\rm thr} m_e c/eE_0$ is the time required for particles to be accelerated from rest to $\gamma_{\rm thr}$, and (ii) $t_p \equiv f t_a$ is the time required for particles that just emitted a pair to be reaccelerated to $\gamma_{\rm thr}$. These timescales are illustrated in the schematic representation of the cascade process in Fig. 1.

Any particle in this simple system emits new pairs every t_p after being accelerated to $\gamma_{\rm thr}$ for the first time. This naturally divides the system in two populations: n_1 particles with $\gamma \in [\gamma_{\rm thr} - \gamma_{\rm pair}, \gamma_{\rm thr}]$ and n_2 particles with $\gamma < \gamma_{\rm thr} - \gamma_{\rm pair}$ (see Fig. 1). Particles in population 2

Physics of Plasmas ARTICLE scitation.org/journal/php

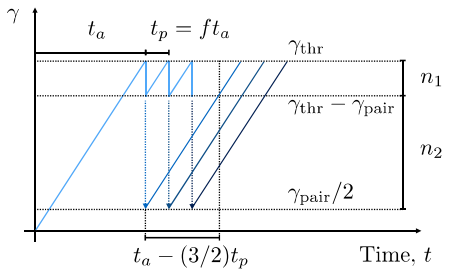

FIG. 1. Schematic representation of heuristic pair production model and associated populations and timescales. Solid blue lines represent the time evolution of the Lorentz factor of electrons (or positrons). When electrons reach a Lorentz factor $\gamma_{\rm thr}$, they emit a pair with energy $\gamma_{\rm pair} m_e c^2$. Emission times are indicated with blue dashed arrows, and new particles created at those times are shown with darker colors. The energy bands, corresponding to populations 1 and 2 described in the text, are indicated on the right-hand side. Characteristic times t_a and t_p are also schematically indicated.

are created with a Lorentz factor $f\gamma_{\rm thr}/2$ and convert into population 1 over a time $t \simeq t_a - 3t_p/2 = t_a(1 - 3f/2)$, i.e., we can write

$$n_1(t + t_a(1 - 3f/2)) \simeq n_1(t) + n_2(t). \tag{1}$$

Symmetrically, particles in population 2 decrease at a rate $n_2/(t_a(1 - 3f/2))$ due to this conversion and increase at a rate $2n_1/t_a$ due to pair production from both species, and we can write

$$\frac{{\rm d}n_2(t)}{{\rm d}t} \simeq \frac{2n_1(t)}{ft_a} - \frac{n_2(t)}{(1 - 3f/2)t_a}. \tag{2}$$

For $f \ll 1$, Eqs. (1) and (2) have an exponentially growing solution $n_{1,2}(t) \propto \exp(\Gamma t)$, with

$$\Gamma t_a \simeq W(2/f) \simeq \ln(2/f), \tag{3}$$

where $W(x)$ is the Lambert function,[34] which behaves as $\ln(x)$ for large x. We note that this solution for Γ scales very weakly with f for all relevant $f \ll 1$.

To verify our theoretical analysis, we have performed 1D PIC simulations with OSIRIS[35,36] of a uniform electron–positron plasma initially at rest and immersed in a uniform electric field E_0. The value of E_0 is chosen such that particles attain relativistic energies over short distances, i.e., $eE_0(c/\omega_p)/m_e c^2 \simeq 3000 \gg 1$, where $\omega_p = (4\pi e^2 n_0/m_e)$ is the plasma frequency associated with the initial plasma density n_0 and e is the electron charge. The simulation domain has length $L/(c/\omega_p) \simeq 30$ and periodic boundary conditions. The grid resolution is $\Delta x/(c/\omega_p) = 0.015$, and the time step is chosen to resolve t_p, the shortest timescale of the problem. In the PIC simulations, pair production is included according to the energy threshold-based heuristic model described above.

In Fig. 2, we represent the evolution in time of the energy in the electric field $W_E = \int_0^L (E^2/8\pi)\,{\rm d}x$ and of the total kinetic energy $W_K = \sum_i (\gamma_i - 1) m_e c^2$ (where the sum is done over all particles) for a simulation with $\gamma_{\rm thr} = 500$ and $f = 0.1$. In the inset, we highlight the exponential growth of the kinetic energy in the early times of the simulation and show that it is well described by a growth rate Γ given by Eq. (3). At these early times, the total kinetic energy in the system grows due to a growing number of particles, whereas the average kinetic energy is approximately constant and is controlled by the distribution function developed during the cascade.[23]

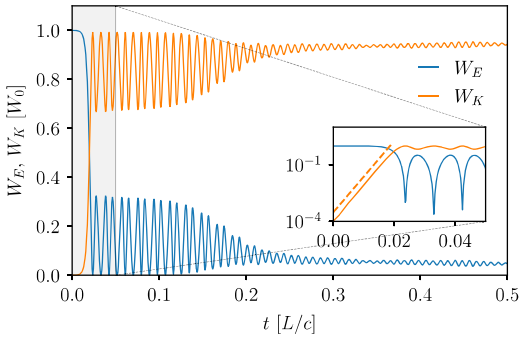

FIG. 2. Time evolution of the energy stored in the electric field W_E and of the total kinetic energy W_K in a simulation of a pair cascade with $\gamma_{\rm thr} = 500$ and $f = 0.1$ developed in a uniform electric field E_0. The energies W_E and W_K are normalized to the total energy available at time $t = 0$, $W_0 = \int_0^L (E_0^2/8\pi)\,{\rm d}x$.

B. Inductive oscillations

As new pairs are created during the cascade, electrons and positrons are accelerated in opposite directions, driving a current. Due to the spatial homogeneity of E, the density of electrons and positrons $n_\pm$ is constant in space (and equal in magnitude) during the cascade and so is the current j that they drive. As the current grows in time, the electric field is screened, as prescribed by Ampère's law

$$\frac{\partial E}{\partial t} = -4\pi j \simeq 8\pi e c n_\pm. \tag{4}$$

When the field is screened, the plasma current is maximum, which reverses the field, decelerating particles. The system enters a stage where the electric field is approximately constant in space and oscillates in time inductively, i.e., supported by reversals of the plasma current.[13] The frequency of these oscillations is the relativistic plasma frequency,[23] $\omega_0 \simeq \sqrt{4\pi e^2 n_\pm/\gamma_{\rm thr} m_e}$. This is illustrated in Fig. 2 for times $t \simeq (0.02 - 0.15)\,L/c$. During this time, electrons and positrons periodically reverse their momentum without producing new pairs. With time, inductive oscillations become unstable,[37] and perturbations in the electric field accelerate a small fraction of particles beyond $\gamma_{\rm thr}$, producing new bursts of pair production. In Fig. 3 (Multimedia view), we show the phase space of electrons and positrons and the electric field profile to illustrate the development of these perturbations. The consecutive pair production bursts ultimately damp the average electric field, and energy is further transferred into particle kinetic energy, as shown in Fig. 2 for times $t > 0.15\,L/c$.

The system behavior described above and illustrated in Figs. 2 and 3 for $f = 0.1$ occurs similarly for other values of $f \ll 1$ and $\gamma_{\rm thr}$. In particular, we have performed simulations with $\gamma_{\rm thr} = 500 - 5000$ and $f = 10^{-3} - 0.1$, and the onset and saturation of the cascade, as well as the excitation and damping of inductive plasma waves, are qualitatively similar for all cases. All analytical estimates derived from the heuristic model considered here, such as the cascade growth rate, the time required for the electric field to be screened and the frequency of the inductive plasma waves, are consistent with simulation results.

Physics of Plasmas ARTICLE scitation.org/journal/php

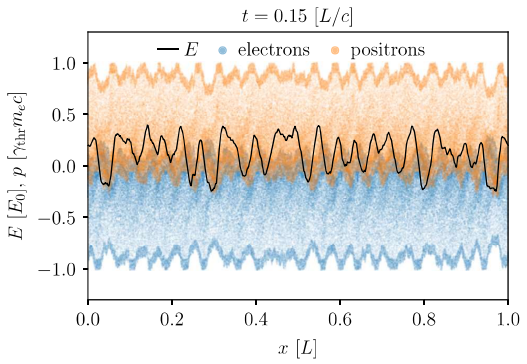

FIG. 3. Phase space of electrons (blue dots) and positrons (orange dots) and electric field profile (black line). The static frame shows a time where the initial pair cascade has ceased, and the electric field oscillates inductively in time, i.e., supported by plasma currents. Perturbations of the electric field developed as a product of the instability of inductive waves are also visible. Reacceleration of electrons and positrons in these perturbations triggers secondary pair production bursts. Multimedia view: https://doi.org/10.1063/5.0085847.1

III. CASCADE IN A LINEAR ELECTRIC FIELD

We now consider a more complex and realistic profile for the electric field. In particular, we assume that the electric field has spatiotemporal dependence, $E = E(x,t)$. A good approximation of $E(x, t)$ can be obtained for vacuum gaps near the stellar surface. To describe the plasma near the surface of the neutron star, it is convenient to write Maxwell's equations in the frame that co-rotates with the pulsar. In this frame, Gauss's and Ampère's laws are, respectively, written as[12]

$$\frac{\partial E}{\partial x} = 4\pi(\rho - \rho_{\rm GJ}), \tag{5a}$$

$$\frac{\partial E}{\partial t} = -4\pi(j - j_{\rm m}), \tag{5b}$$

where $\rho_{\rm GJ}$ is the Goldreich–Julian density,[38] i.e., the equilibrium plasma density in the pulsar magnetosphere, and $j_{\rm m}$ is a background current that locally supports the twist of the magnetic field imposed at large scales by the magnetosphere.

When the plasma density ρ and/or current density j deviate from their equilibrium values, a vacuum gap develops. Simulations show[12,14,23] that this precedes pair cascades, with only one species (electrons or positrons) of approximately constant density flowing through the gap toward the stellar surface. Without loss of generality, we assume here that positrons initially flow through the gap (which corresponds to the configuration found in gaps of pulsars where the magnetic and rotation axes are aligned, with $\rho_{\rm GJ} < 0$) at the speed of light with charge density $\rho_+ = r|\rho_{\rm GJ}|$, where $0 < r < 1$ is a ratio to be determined. In these conditions, it is possible to integrate Eqs. (5a) and (5b) to show that the electric field is

$$E(x,t) = \begin{cases} 4\pi|\rho_{\rm GJ}|(1+r)(x - v_f t), & x < v_f t, \\ 0, & x \geq v_f t, \end{cases} \tag{6}$$

where v_f is the velocity at which the front of the gap moves. This velocity can be related to $\alpha \equiv -j_{\rm m}/|\rho_{\rm GJ}|c$ and r as $v_f/c = (\alpha - r)/(1 + r) \simeq r$. Previous analytical[39] and numerical[14] works suggest that $\alpha < 0$ or $\alpha > 1$ for pair cascades to be produced in pulsar polar caps. In the following analysis, we consider that $1 < \alpha < 3$, such that $1/3 < v_f/c < 1$. The electric field profile in Eq. (6) is schematically illustrated in Fig. 4.

A. Growth in time

It is straightforward to note that the typical timescales t_a and t_p are no longer constant nor equal for electrons and positrons with the electric field in Eq. (6). For $x < v_f t$, $E(x,t) < 0$, and thus, any positron is accelerated toward the stellar surface ($x = 0$), and conversely any electron is accelerated toward the magnetosphere ($x > 0$). Therefore, in their paths, positrons/electrons experience increasing/decreasing values of the electric field. Thus, the acceleration and re-acceleration times of positrons and electrons are a function of the position x_i and time t_i in which they are created or enter the gap, $t_{a\pm} = t_{a\pm}(x_i, t_i)$ and $t_{p\pm} = t_{p\pm}(x_i, t_i)$. Integrating the equation of motion of electrons and positrons, it is possible to derive

$$t_{a\pm}(x_i,t_i) \simeq \frac{t_i\beta_f - x_i/c}{1 \pm \beta_f} - \sqrt{\left(\frac{t_i\beta_f - x_i/c}{1 \pm \beta_f}\right)^2 \pm \frac{\gamma_{\rm thr}/(1+r)\omega_{p,\rm GJ}^2}{1 \pm \beta_f}}, \tag{7}$$

where $\beta_f \equiv v_f/c$ and $\omega_{p,\rm GJ} = \sqrt{4\pi e^2 n_{\rm GJ}/m_e}$ is the plasma frequency associated with a number density $n_{\rm GJ} = |\rho_{\rm GJ}|/e$. Under realistic conditions, the terms inside the square root in Eq. (7) can be comparable, so both need to be taken into account when computing $t_{a\pm}$. The reacceleration time $t_{p\pm}$ can be expressed by replacing $\gamma_{\rm thr} \to f\gamma_{\rm thr}$ in the last term of Eq. (7).

Rigorously determining the evolution in time of the number of particles in the cascade with the time and space dependent $t_{a\pm}$ and $t_{p\pm}$ determined above is a challenging task. Moreover, with such time and space dependence, it is not straightforward that a pure exponential

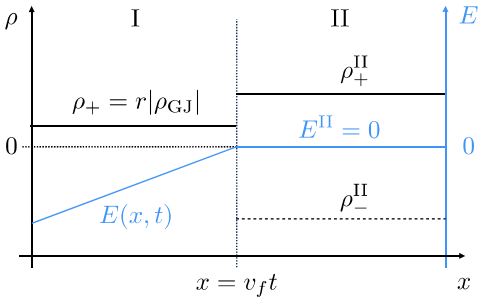

FIG. 4. Schematic representation of the linear electric field profile considered in Sec. III. In the open gap (region I), a stream of positrons of charge density ρ_+ travels toward the stellar surface ($x = 0$). Because the total charge density in this region does not match $\rho_{\rm GJ}$, a linear electric field $E(x, t)$ given by Eq. (6) develops. In region II, the electric field is $E^{\rm II} = 0$ because the total charge and current densities match the equilibrium conditions, $\rho^{\rm II} = \rho_+^{\rm II} + \rho_-^{\rm II} = \rho_{\rm GJ}$ and $j^{\rm II} = j_{\rm m}$, respectively. The boundary between regions I and II moves with velocity $v_f > 0$.

Physics of Plasmas ARTICLE scitation.org/journal/php

behavior similar to that observed for a constant electric field occurs. Here, we seek a solution for a scenario where $t_{a\pm}$ and $t_{p\pm}$ are slowly varying, such that one may have a local growth rate. In particular, we investigate the case of a single layer of electrons streaming through the open gap and pair producing over time. For such layer, new electrons always co-move with their primary particles, whereas positrons are immediately directed toward the stellar surface. We consider this layer to be arbitrary thin, which is a good approximation since its thickness grows as $\Delta x \simeq tc/(f\gamma_{\rm thr})^2$, with $f\gamma_{\rm thr} \ll 1$. As mentioned above, we study in particular the case where $t_a(t)$ and $t_p(t)$ (we drop the subscript from here on for simplicity) are slowly evolving, which is possible for $v_f/c \gtrsim 0.7$ and $f \lesssim 0.05$. First, we assume that $t_p(t) \simeq f t_a(t)$ and, therefore, since $f \ll 1$, $t_a(t) - 3t_p(t)/2 \simeq t_a(t)$. This assumption is valid as long as the layer is far from the front of the gap. In these conditions, it is possible to rewrite Eqs. (1) and (2) as

$$n_1(t + t_a(t)) \simeq n_1(t) + n_2(t), \tag{8a}$$

$$\frac{{\rm d}n_2(t)}{{\rm d}t} \simeq \frac{n_1(t)}{f t_a(t)} - \frac{n_2(t)}{t_a(t)}. \tag{8b}$$

We note that the first term on the right-hand side of Eqs. (2) and (8b) differs by a factor of 2 because, in the case of a linear electric field, the growth in the number of electrons is caused only by pair production events triggered by primary electrons (and not positrons).

Given the results presented in Sec. II and the rational above, it is reasonable to assume that the solution of this system can be written with the WKB approximation

$$n_{1,2}(t) \propto \exp\left(\int_{t_a^*}^{t} \Gamma(t')\,{\rm d}t'\right), \tag{9}$$

where $\Gamma(t')$ is the local (in time) growth rate of the cascade at time t' and t_a^* is the time in which $n_{1,2}$ starts to grow exponentially, which can be estimated as the time of creation of the second generation of electrons. Plugging $n_2(t)$ into Eq. (8b), we can write

$$\frac{n_2(t)}{n_1(t)} = \frac{1}{f(\Gamma(t)t_a(t) + 1)}. \tag{10}$$

Assuming now that $\Gamma(t)$ varies slowly during a time $t_a(t)$, we use its Taylor expansion $\Gamma(t') = \Gamma(t) + (t' - t)\dot{\Gamma}(t)$ to obtain

$$\int_t^{t+t_a(t)} \Gamma(t')\,{\rm d}t' \simeq \Gamma(t)t_a(t)\left(1 + \frac{\dot{\Gamma}(t)t_a(t)}{2\Gamma(t)}\right) \equiv \Gamma(t)t_a(t)(1 + \psi(t)). \tag{11}$$

Plugging this result in Eq. (8a) and using Eq. (10), we get

$$\exp\left[\tilde{\Gamma}(t)t_a(t)\right] \simeq \frac{1 + \psi(t)}{f\tilde{\Gamma}(t)t_a(t)}, \tag{12}$$

where $\tilde{\Gamma}(t) = \Gamma(t)(1 + \psi(t))$. The solution of Eq. (12) yields a correction to Eq. (3),

$$\Gamma(t)t_a(t) = \frac{1}{1 + \psi(t)} W\left(\frac{1 + \psi(t)}{f}\right). \tag{13}$$

We note that this is not a fully closed form of $\Gamma(t)$, since ψ is a function of Γ and $\dot{\Gamma}$. Assuming that $t_a(t) \simeq t_a^*(1 + Ct)$, where $C \ll 1$ is a constant, we can get ψ to the lowest order when $\Gamma(t)t_a(t) \simeq W(1/f)$,

$$\psi \simeq \frac{Ct_a^*}{W(1/f)} \ll 1. \tag{14}$$

We have performed a set of 1D PIC simulations that validate the analysis presented above. In these simulations, a single electron is initialized at the stellar surface ($x = 0$). This electron experiences an external electric field given by Eq. (6) with the time translation $t \to t - t_0$, where the time t_0 is estimated to be the time at which a positron stream from the magnetosphere would pair produce at the surface. We use in all simulations $\gamma_{\rm thr} = 1000$ and vary $v_f \in [0.5, 0.9]$ and $f \in [0.005, 0.1]$. The length of the simulation domain L is chosen such that electron layer reaches the front of the gap at $x < L$. The grid resolution is $\Delta x/L = 0.001$, and the time step is chosen to resolve the smallest expected $t_p(t)$. Additionally, we set the initial electron density to be low enough such that particle motion is dominated by the externally imposed electric field at all times, i.e., the total electric field experienced by electrons is never significantly affected by the plasma current.

In Fig. 5, we show the results of these simulations. Figures 5(a) and 5(b) show the evolution in time of the number of electrons N_- for fixed $v_f = 0.6$ and varying f and for fixed $f = 0.05$ and varying v_f, respectively. These results suggest that, as with a uniform background electric field, the cascade grows exponentially. It is also clear that, as before, the cascade grows faster for smaller f. In these simulations, the number of electrons grows until the electron layer catches the front of the gap, where $E = 0$ and pair production ceases. For the set of simulations shown in Fig. 5(a), this happens at $t \simeq 0.3\,L/c$. In Fig. 5(b), it is clear that this time increases with v_f, as intuitively expected. From Figs. 5(a) and 5(b), it is also clear that N_- grows progressively slower with time, which is consistent with our hypothesis from the expected increase over time of $t_p(t)$ and $t_a(t)$. In Fig. 5(c), we show the growth rate $\Gamma(t)$ for the simulation with $f = 0.05$ and $v_f/c = 0.7$. This growth rate was obtained by fitting exponential curves to $N_-(t)$ over short time intervals centered at t. In Fig. 5(c), we also plot the growth rate estimated with Eq. (13), showing that it approximates well the simulation results. A similar correspondence is obtained for all simulations with $v_f/c > 0.7$ and $f < 0.05$. We note that the peaks observed in Fig. 5(c) correspond to times $t \lesssim 1 - 2t_a$ in which the growth is not yet purely exponential and, thus, falls out of the regime of validity of our model. This only approximately exponential phase is visible in Figs. 5(a) and 5(b) in the sudden periodic increases in N_- at early times.

B. Growth in space

To extend our analysis from one to multiple electron layers, we have performed a second set of simulations where we externally impose the electric field in Eq. (6) (without time translation) and start with a uniform positron distribution. Positrons are accelerated as the gap opens, pair producing at $x \simeq 0$. Fresh electrons are then accelerated toward the magnetosphere, with each electron developing its own single-layered cascade. Since we start from a uniform positron distribution, a multi-layered cascade is generated in this case. However, all layers move at approximately the speed of light, so each layer behaves according to the model outlined above.

Physics of Plasmas ARTICLE scitation.org/journal/php

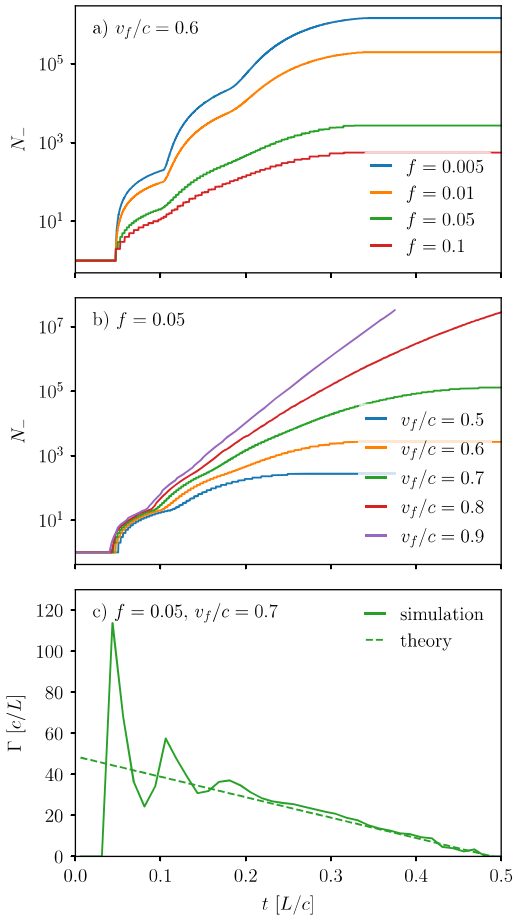

FIG. 5. Time evolution of the number of electrons N_- in simulations of pair cascades developed in a linear electric field with (a) fixed $v_f/c = 0.6$ and varying f and (b) fixed $f = 0.05$ and varying v_f/c. Panel (c) shows the evolution of the local (in time) growth rate of N_- for the simulation with $f = 0.05$ and $v_f/c = 0.7$ [represented with a green line in (b)], together with the theoretical estimate given by Eq. (13).

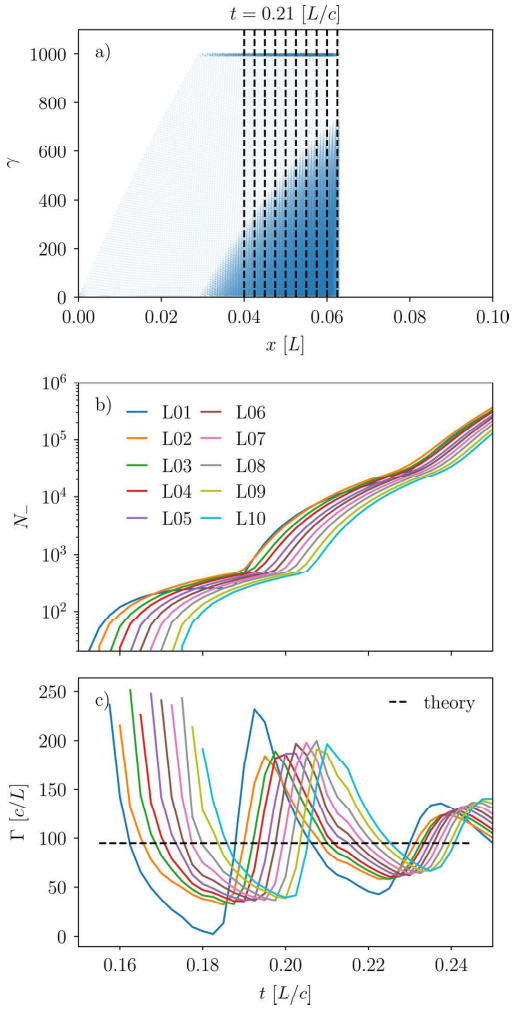

FIG. 6. (a) Distribution in space and energy of electrons (blue dots) in simulation of a pair cascade with a linear electric field with parameters $f = 0.01$ and $v_f/c = 0.9$. (b) Time evolution of the number of electrons in the layers identified by the boundaries drawn with vertical dashed lines in (a). Layer numbers increase from the front to the back of the cascade (i.e., with decreasing x). (c) Local (in time) growth rates of the curves in (b), compared with the theoretical estimate given by Eq. (13) with $\psi \simeq 0$ and $t_a(t) \simeq t_a^*$.

We illustrate the development of this multi-layered cascade in a simulation with $f = 0.01$ and $v_f/c = 0.9$ in Fig. 6. We follow the number of electrons in different layers of width $\Delta x_L = 0.0025\,L$ starting from the leading edge, or the front of the cascade. In Fig. 6(a), we present the particle distribution in space and energy, as well as a visual representation of the multiple layers considered. Figures 6(b) and 6(c) show the evolution in time of the number of electrons in each layer and the corresponding growth rate, respectively, confirming that each layer grows in an approximately exponential fashion. Furthermore, we see that the layers grow progressively faster from the front to the back of the cascade. This is a consequence of the electrons in the back layers experiencing a larger electric field at the time they are created (and thus throughout the development of their single-layered cascade). Moreover, in Fig. 6(c), we also show that the growth rate obtained analytically [with Eq. (13) with $\psi \simeq 0$ and $t_a(t) \simeq t_a^*$] fits reasonably well the average growth rate of the different layers.

Physics of Plasmas ARTICLE scitation.org/journal/php

The varying growth rate identified above for the different layers naturally gives rise to a non-uniform electron density spatial profile. This profile is shown in Fig. 7 for the same simulation and time shown in Fig. 6(a). Despite the lower growth rate in time of the front layers, the density decreases from the front to the back of the cascade. This happens because layers at any distance d behind the head are created with a temporal lag d/c, which for the time shown in Fig. 7 is not enough to flatten (or reverse) the electron density profile.

We can estimate the profile $n_-(x,t)$ based on the form of $\Gamma(t)$ previously determined. Assuming that the electric field varies slowly in space, we can write the density of the kth layer from the front as

$$n_{-,k}(t) \simeq n_{-,k+1}(t)\exp\left(\Gamma(t)\Delta x_L/c\right). \tag{15}$$

Taking arbitrary small Δx_L, we can finally write

$$n_-(x,t) \propto \exp\left(\Gamma(t)(t+x/c)\right). \tag{16}$$

This estimate holds for as long as the growth rate of individual layers is approximately the same, i.e., while the number of electrons in each layer is dominantly determined by the lifetime of that layer. This condition can be written as $t\dot{\Gamma}(t)/\Gamma(t) \ll 1$, which is valid in early times of the cascade. In Fig. 7, we plot lines with slopes computed with Eq. (16) for sample layers L02 and L10, which are shown to be in good agreement with the local shape of $n_-(x,t)$ obtained from the simulation.

The approximate profile in Eq. (16) can finally be used to compute the time it takes to screen the electric field. Since the front of the cascade is the denser than the back, the field is first screened also at this position when $n_- \simeq -j_m/ec$. Since $|j_m| \simeq (1-2)|\rho_{GJ}|c$ and, from previous simulations,[12,14,23] $n_-(t)$ grows from an initial density $\simeq (0.01-0.1)|\rho_{GJ}|/e$, then the screening time is $t_s \simeq 1/\Gamma(t_a^*)$. Given that $\Gamma(t_a^*) \simeq W(1/f)t_a(t_a^*)$ [from Eq. (13)] and that $W(1/f) \simeq 3-5$ for $f \simeq 10^{-6}-10^{-3}$, we can finally estimate $t_s \simeq t_a(t_a^*)$. For realistic pulsars, t_s varies between 10^{-9} and 10^{-6} s with the increasing rotation period, a result in good agreement with previous theoretical and numerical predictions.[15]

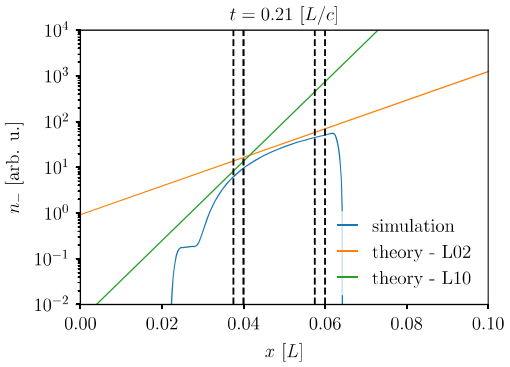

FIG. 7. Electron density profile obtained in the same simulation illustrated in Fig. 6 ($f = 0.01$ and $v_f/c = 0.9$). The density profile is well estimated by the theoretical estimate in Eq. (16), which is represented here with the slopes of the lines in orange and green for the layers L02 and L10 of the cascade, respectively. These layers are defined in the text and illustrated in Fig. 6(a).

IV. CONCLUSIONS

Heuristic models of pair cascades represent an important tool to develop a theoretical understanding of the rich interplay between QED and plasma kinetic effects. In this work, we have studied this interplay using an heuristic model in which electrons and positrons produce new pairs whenever they are accelerated beyond a threshold energy. In particular, we have compared the development of cascades in constant and linear background electric field profiles. For a uniform electric field, we have shown that the number of particles in the cascade grows exponentially and compared an analytical estimate of its growth rate with simulation results.

We have then shown that cascades also grow exponentially in a linear electric field, but present a key distinctive property: the growth rate decreases with time due to the decreasing electric field that the cascade seed particles experience. This ultimately results in a spatially dependent growth rate for the density of electron clouds generated in cascades near the surface of neutron stars. Specifically, the density of the front of these clouds is expected to grow slower than their back. However, since the front of the clouds is generated earlier, the electron density decreases from the front to the back. These results are consistent with previous 1D PIC simulations of pair cascades, including pair production from first principles and in self-consistently developed (linear) electric fields.[12,14] We have derived analytical estimates for the spatiotemporal growth of the cascade and validated them against 1D PIC simulations, including heuristic pair production. Finally, we have estimated the time at which the plasma generated in the cascade first screens the gap electric field. An analysis of the properties of inductive waves self-consistently generated as a result of pair cascades in a linear electric field is left as future work.

The insights developed with the analytical models presented in this work can be applied to interpret more complex, full QED simulations of pair cascades. Yet, their applicability is limited to the regime of validity of the heuristic model considered in this work (negligible photon mean free path). Extensions of this model, and consequently of the theory presented here, are next steps on the study of pair cascades in compact objects. In particular, including a soft energy threshold for photon emission and a (constant or spatially dependent) finite photon mean free path would further approximate these models to the *ab initio* description of pair cascades.

ACKNOWLEDGMENTS

This work was supported by the European Research Council (No. ERC-2015-AdG Grant 695088) and FCT (Portugal) (Grant No. PD/BD/114307/2016) in the framework of the Advanced Program in Plasma Science and Engineering (APPLAuSE, FCT Grant No. PD/00505/2012).

AUTHOR DECLARATIONS

Conflict of Interest

The authors have no conflicts to disclose.

DATA AVAILABILITY

The data that support the findings of this study are available from the corresponding author upon reasonable request.

Physics of Plasmas ARTICLE scitation.org/journal/php

REFERENCES

[1]F. C. Michel, "Theory of pulsar magnetospheres," Rev. Mod. Phys. **54**, 1–66 (1982).
[2]J. Pétri, "Theory of pulsar magnetosphere and wind," J. Plasma Phys. **82**, 635820502 (2016).
[3]B. Cerutti and A. M. Beloborodov, "Electrodynamics of pulsar magnetospheres," Space Sci. Rev. **2017**, 111–136.
[4]F. V. Coroniti, "Magnetically striped relativistic magnetohydrodynamic winds: The Crab Nebula revisited," Astrophys. J. **349**, 538 (1990).
[5]Y. E. Lyubarskii, "A model for the energetic emission from pulsars," Astron. Astrophys. **311**, 172–178 (1996).
[6]P. A. Sturrock, Astrophys. J. **164**, 529–556 (1971).
[7]M. A. Ruderman and P. G. Sutherland, Astrophys. J. **196**, 51–72 (1975).
[8]T. Erber, "High-energy electromagnetic conversion processes in intense magnetic fields," Rev. Mod. Phys. **38**, 626–659 (1966).
[9]V. I. Ritus, J. Sov. Laser Res. **6**, 497–617 (1985).
[10]J. Arons, "Pair creation above pulsar polar caps: Geometrical structure and energetics of slot gaps," Astrophys. J. **266**, 215–241 (1983).
[11]K. S. Cheng, C. Ho, and M. Ruderman, "Energetic radiation from rapidly spinning pulsars. I. Outer magnetosphere gaps," Astrophys. J. **300**, 500 (1986).
[12]A. N. Timokhin, "Time-dependent pair cascades in magnetospheres of neutron stars-I. Dynamics of the polar cap cascade with no particle supply from the neutron star surface," Mon. Not. R. Astron. Soc. **408**, 2092–2114 (2010).
[13]A. Levinson, D. Melrose, A. Judge, and Q. Luo, Astrophys. J. **631**, 456–465 (2005).
[14]A. N. Timokhin and J. Arons, "Current flow and pair creation at low altitude in rotation-powered pulsars' force-free magnetospheres: Space charge limited flow," Mon. Not. R. Astron. Soc. **429**, 20–54 (2012).
[15]A. N. Timokhin and A. K. Harding, "On the polar cap cascade pair multiplicity of young pulsars," Astrophys. J. **810**, 144 (2015).
[16]A. Philippov, A. Timokhin, and A. Spitkovsky, Phys. Rev. Lett. **124**, 245101 (2020).
[17]F. Cruz, T. Grismayer, A. Y. Chen, A. Spitkovsky, and L. O. Silva, "Coherent emission from QED cascades in pulsar polar caps," Astrophys. J. Lett. **919**, L4 (2021).
[18]A. A. Philippov and A. Spitkovsky, "*Ab initio* pulsar magnetosphere: Three-dimensional particle-in-cell simulations of axisymmetric pulsars," Astrophys. J. Lett. **785**, L33 (2014).
[19]M. A. Belyaev, "Dissipation, energy transfer, and spin-down luminosity in 2.5D PIC simulations of the pulsar magnetosphere," Mon. Not. R. Astron. Soc. **449**, 2759–2767 (2015).
[20]B. Cerutti, A. A. Philippov, K. Parfrey, and A. Spitkovsky, "Particle acceleration in axisymmetric pulsar current sheets," Mon. Not. R. Astron. Soc. **448**, 606–619 (2015).
[21]C. Kalapotharakos, G. Brambilla, A. Timokhin, A. K. Harding, and D. Kazanas, "Three-dimensional kinetic pulsar magnetosphere models: Connecting to gamma-ray observations," Astrophys. J. **857**, 44 (2018).
[22]G. Brambilla, C. Kalapotharakos, A. N. Timokhin, A. K. Harding, and D. Kazanas, "Electron–positron pair flow and current composition in the pulsar magnetosphere," Astrophys. J. **858**, 81 (2018).
[23]F. Cruz, T. Grismayer, and L. O. Silva, "Kinetic model of large-amplitude oscillations in neutron star pair cascades," Astrophys. J. **908**, 149 (2021).
[24]A. Y. Chen and A. M. Beloborodov, "Electrodynamics of axisymmetric pulsar magnetosphere with electron-positron discharge: A numerical experiment," Astrophys. J. Lett. **795**, L22 (2014).
[25]A. A. Philippov, A. Spitkovsky, and B. Cerutti, "*Ab initio* pulsar magnetosphere: Three-dimensional particle-in-cell simulations of oblique pulsars," Astrophys. J. Lett. **801**, L19 (2015).
[26]A. A. Philippov, B. Cerutti, A. Tchekhovskoy, and A. Spitkovsky, "*Ab initio* pulsar magnetosphere: The role of general relativity," Astrophys. J. Lett. **815**, L19 (2015).
[27]A. Y. Chen, F. Cruz, and A. Spitkovsky, "Filling the magnetospheres of weak pulsars," Astrophys. J. **889**, 69 (2020).
[28]C. Guépin, B. Cerutti, and K. Kotera, Astron. Astrophys. **635**, A138 (2020).
[29]J. Benáček, P. A. Muñoz, A. C. Manthei, and J. Büchner, "Radio emission by soliton formation in relativistically hot streaming pulsar pair plasmas," Astrophys. J. **915**, 127 (2021).
[30]J. Benáček, P. A. Muñoz, and J. Büchner, "Bunch expansion as a cause for pulsar radio emissions," Astrophys. J. **923**, 99 (2021).
[31]S. R. Kelner, A. Y. Prosekin, and F. A. Aharonian, Astrophys. J. **149**, 33 (2015).
[32]F. Del Gaudio, Ph.D. thesis, Instituto Superior Técnico, 2020.
[33]J. Arons and E. T. Scharlemann, "Pair formation above pulsar polar caps: Structure of the low altitude acceleration zone," Astrophys. J. **231**, 854–879 (1979).
[34]R. M. Corless, G. H. Gonnet, D. E. G. Hare, D. J. Jeffrey, and D. E. Knuth, Adv. Comput. Math. **5**, 329–359 (1996).
[35]R. A. Fonseca, L. O. Silva, F. S. Tsung, V. K. Decyk, W. Lu, C. Ren, W. B. Mori, S. Deng, S. Lee, T. Katsouleas, and J. C. Adam, "OSIRIS: A three-dimensional, fully relativistic particle in cell code for modeling plasma based accelerators," in *Computational Science—ICCS 2002*, edited by P. M. A. Sloot, A. G. Hoekstra, C. J. K. Tan, and J. J. Dongarra (Springer, Berlin, Heidelberg, 2002), pp. 342–351.
[36]R. A. Fonseca, S. F. Martins, L. O. Silva, J. W. Tonge, F. S. Tsung, and W. B. Mori, Plasma Phys. Controlled Fusion **50**, 124034 (2008).
[37]F. Cruz, T. Grismayer, and L. O. Silva, "Kinetic instability in inductively oscillatory plasma equilibrium," Phys. Rev. E **103**, L051201 (2021).
[38]P. Goldreich and W. H. Julian, "Pulsar electrodynamics," Astrophys. J. **157**, 869 (1969).
[39]A. M. Beloborodov, "Polar-cap accelerator and radio emission from pulsars," Astrophys. J. Lett. **683**, L41–L44 (2008).